Dissertation zur Erlangung des akademischen Grades

„doctor rerum naturalium“

(Dr. rer. nat.)

Crater Morphologies and the Distribution of Ejecta Deposits on the Dwarf Planet Ceres

vorgelegt von Dipl.-Geophysikerin Franziska Schulzeck

im Fachbereich Geowissenschaften der Freien Universität Berlin

Berlin, 2018

Erstgutachter: Prof. Dr. Ralf Jaumann

Freie Universität Berlin
Institut für Geologische Wissenschaften
Fachrichtung Planetologie und Fernerkundung
sowie
Deutsches Zentrum für Luft- und Raumfahrt
Institut für Planetenforschung, Abt. Planetengeologie

Zweitgutachter: Prof. Dr. Lena Noack

Freie Universität Berlin
Institut für Geologische Wissenschaften
Fachrichtung Geochemie, Hydrogeologie, Mineralogie

Tag der Disputation: 19. November 2018

EIDESSTATTLICHE ERKLÄRUNG

Hiermit erkläre ich, dass ich die beigefügte Dissertation selbstständig verfasst und keine anderen als die angegebenen Hilfsmittel genutzt habe. Alle wörtlich oder inhaltlich übernommenen Stellen habe ich als solche gekennzeichnet.

Ich versichere außerdem, dass ich die beigefügte Dissertation nur in diesem und keinem anderen Promotionsverfahren eingereicht habe und, dass diesem Promotionsverfahren keine endgültig gescheiterten Promotionsverfahren vorausgegangen sind.

Berlin, 07. Dezember 2018 Franziska Schulzeck

DANKSAGUNG

Ich danke Herrn Prof. Dr. Ralf Jaumann und Frau Dr. Katrin Stephan für die Betreuung meiner Doktorarbeit und Frau Prof. Dr. Lena Noack für die Übernahme des Zweitgutachtens. Darüber hinaus danke ich allen Mitarbeitern der Abteilung Planetengeologie am DLR-Institut für Planetenforschung in Berlin für ihre Unterstützung. Für ihre fachliche Unterstützung danke ich speziell Katrin Krohn, Stefanus Schröder und Katharina Otto. Besonders danken möchte ich meinen beiden Zimmerkollegen Isabel von der Gathen und Martin Voelker. Auch danke ich meinem Onkel Jochen. Der größte Dank gilt meinem Freund, meiner Schwester und meinen Eltern.

ABSTRACT

The following thesis describes a combined approach of geologic mapping and ballistic calculations of ejected material to investigate the surface composition and the processes that shaped the dwarf planet Ceres. The analyses are based on data of the Dawn mission.

After orbiting the asteroid Vesta from 2011 to 2012, the Dawn spacecraft reached Ceres' orbit in March 2015. The main goals of the Dawn mission were to investigate the geology, interior composition and past and present endogenic and exogenic processes of Ceres and Vesta to describe their evolution and to gain a broader understanding of the early solar system and protoplanet growth (Russell and Raymond, 2011; Russell et al., 2016). This thesis will contribute to the understanding of the geology, the evolution and the dynamics of Ceres.

This work utilized a two-step procedure to analyze the composition and geologic history of the surface of Ceres. First, including clear filter, topographic and color data, geologic mapping was conducted for the Sintana quadrangle in the southern hemisphere of Ceres to identify geologic processes and to help to assemble a global stratigraphy for Ceres. In the course of the mapping, geologic units and features were analyzed and absolute ages of geologic units were determined. Second, ejecta deposition of the small and fast rotating dwarf planet was investigated by analytical ballistic calculations in order to understand the origin and distribution of geologic units. To examine the relation between ejecta and secondary cratering, particle sizes were calculated. Moreover, the special case of ejecta dynamics of boulder craters was analyzed, as well as the ballistics and size-frequency distributions of the ejecta blocks themselves.

The geologic mapping reveals an ice-rich subsurface that is predominantly resurfaced by large impact events. The crater shapes in the Sintana quadrangle resemble those on icy satellites with a great variety of morphologies. Moreover, secondary crater chains cross the quadrangle. In addition, the morphology of blocky landslides is indicative of an ice-rich subsurface. The mapping region shows no evidence of endogenic activity, but the absolute age of the cratered terrain background unit hints to a resurfacing event that was possibly induced by impact ejecta/melt of the close-by Kerwan basin.

Features and processes that were identified in the Sintana region, such as secondary crater chains, boulders, resurfacing by large impact craters and asymmetric ejecta blankets, are even more distinct in other regions of Ceres. Ballistic calculations were used to investigate the origin of those observations. The results of the ballistic calculations show that the rotation of Ceres leads to a specifically asymmetric ejecta deposition and that a planet-wide contamination with

secondary craters that bias surface ages is very likely. The low gravity regime results in a long-range transport of particles; hence ejecta might be deposited far away from its primary crater. The particle sizes of high-velocity particles could be large enough to produce distant secondary craters and can therefore explain the secondary crater chains that are observed all over Ceres. The analysis of boulder crater ejecta deposits shows that they are as asymmetric as the ejecta deposits of larger impact basins on Ceres. The investigation of boulders demonstrates that the deposition of low-velocity ejecta is also influenced by the Coriolis effect. Steep slopes of boulder size-frequency distributions are in agreement with the idea that such blocks produce secondary craters with a similar distribution (McEwen and Bierhaus, 2006). As already revealed by geologic mapping, the ballistic analysis confirms that a high contamination of the surface by secondary impacts is likely, for instance, in the shape of non-radial crater chains. Secondary craters, in turn, pose problems in the dating of geological units, because they can increase the estimated age of a surface.

In short, this work is the first extensive study about the rotational effects on ejecta deposition on the dwarf planet Ceres.

ZUSAMMENFASSUNG

Die vorliegende Dissertation kombiniert eine geologische Kartierung mit ballistischen Berechnungen von Auswurfmaterial zur Untersuchung der Oberflächenzusammensetzung und der oberflächenformenden Prozesse des Zwergplaneten Ceres. Die Analysen basieren auf Daten der Dawn-Mission.

Nachdem sich die Raumsonde Dawn zwischen 2011 und 2012 im Orbit des Asteroiden Vesta aufhielt, trat sie im März 2015 in den Orbit des Zwergplaneten Ceres ein. Ziel der Dawn-Mission war es, sowohl die innere und äußere Zusammensetzung von Ceres und Vesta als auch endogene und exogene Prozesse zu erforschen, um mehr über die Entwicklung des Sonnensystems und die Entstehung von Protoplaneten zu erfahren (Russell and Raymond, 2011; Russell et al., 2016). Die vorliegende Arbeit trägt zu diesem Verständnis von Geologie, Evolution und Dynamik des Zwergplaneten Ceres bei.

Das methodische Vorgehen zur Untersuchung der Entwicklung und Zusammensetzung der Oberfläche von Ceres lässt sich in zwei Schritte unterteilen. Zunächst wurde unter Einbeziehung von Klarfilteraufnahmen, Farbfilteraufnahmen und topografischen Daten das Quadrangel Sintana in Ceres‘ Südhemisphäre geologisch kartiert. Im Zuge dessen wurden geologische Einheiten und Strukturen untersucht und das Oberflächenalter bestimmt. Dadurch konnten die zu Grunde liegenden geologischen Prozesse identifiziert werden und eine Einordnung in die globale Stratigraphie vorgenommen werden. Ballistische Berechnungen veranschaulichen als zweite Methode die Verteilung von Auswurfmaterial des kleinen schnell rotierenden Zwergplaneten. Dies ist relevant, um den Ursprung geologischer Einheiten zurückverfolgen zu können. Um den Zusammenhang zwischen Auswurfmaterial und Sekundärkratern zu untersuchen, wurden darüber hinaus Partikelgrößen berechnet. Als Spezialfall wurde die Auswurfdynamik von Kratern mit großen Auswurfbrocken analysiert sowie die Größenverteilung und Ballistik der Brocken selbst.

Die Ergebnisse der geologischen Kartierung weisen auf einen hohen Eisanteil im Untergrund hin und zeigen, dass hauptsächlich große Einschläge für die Umstrukturierung der Oberfläche verantwortlich sind. Die kartierten Kraterstrukturen ähneln denen auf den Eismonden. Das kartierte Gebiet zeigt zudem eine Vielfalt an Kraterformen und zahlreiche Sekundärkraterketten. Auch die Morphologie von Massenbewegungsablagerungen auf Ceres ist ein Indiz für eine eisreiche Zusammensetzung des Untergrundes. Hinweise auf endogene Aktivitäten in dem kartierten Teil der Oberfläche wurden allerdings nicht gefunden. Die Altersbestimmung deutet

zusätzlich darauf hin, dass das kartierte Gebiet von Auswurfmaterial oder Impaktschmelze überprägt wurde, wahrscheinlich vom angrenzenden Kraterbecken Kerwan.

Die Sintanaregion zeigt Sekundärkraterketten, Auswurfbrocken, die Überprägung durch große Einschlagskrater und deutet auf eine asymmetrische Ablagerung des Auswurfmaterials hin. Diese Strukturen und Prozesse sind noch ausgeprägter in anderen Regionen von Ceres zu finden. Ballistische Berechnungen haben den Ursprung dieser Beobachtungen untersucht. Die Ergebnisse dieser Berechnungen zeigen, dass sich das Auswurfmaterial durch die Rotation von Ceres asymmetrisch ablagert. Zudem ist eine oberflächenweite Kontamination mit Sekundärkratern sehr wahrscheinlich, was zu einer Verzerrung der Altersmessungen führt. Die geringe Gravitationsbeschleunigung erlaubt den Partikeln weite Strecken zurückzulegen, bevor sie wieder auf die Oberfläche treffen. Dies hat zur Folge, dass sich Auswurfmaterial auch weit entfernt von dem Primärkrater befinden kann. Die Partikelgrößen von schnellen Partikeln können ausreichend sein, um Sekundärkrater zu produzieren, und können so die Sekundärkraterketten erklären, die sich auf Ceres‘ Oberfläche befinden. Genau wie bei großen Einschlagsbecken, zeigt sich auch bei kleineren Kratern, in deren Umgebung sich intakte Auswurfbrocken befinden, die asymmetrische Verteilung des Auswurfmaterials. Die Analyse dieser Brocken zeigt, dass selbst die Bahnen langsamer Partikel durch den Corioliseffekt abgelenkt werden. Die Größenhäufigkeitsverteilung der Brocken selbst weist einen steilen Anstieg auf, wie es auch für Sekundärkrater beobachtet wird (McEwen and Bierhaus, 2006). Ebenso wie die geologische Kartierung, zeigt auch die Untersuchung der Auswurfsmaterialverteilung, dass auf Ceres eine hohe Verunreinigung mit Sekundärkratern, z.B. in Form von nicht radialen Sekundärkraterketten, zu erwarten ist. Demzufolge ist eine fehleranfällige Altersbestimmung möglich, da diese Krater die bestimmten Oberflächenalter erhöhen.

Die vorliegende Arbeit beschreibt zum ersten Mal umfassend den Einfluss der Rotation von Ceres auf die Ablagerung von Auswurfmaterial.

CONTENTS

LIST OF FIGURES

LIST OF TABLES

LIST OF SYMBOLS

Symbol	Variable
D_p	projectile diameter
D_{sc}	simple-to-complex transition diameter
D_T	transient crater radius
$-e_x$, C, λ	material constants
R_{planet}	planetary radius
T_f	tension at fracture
v_p	impact velocity/projectile velocity
ϱ_b	bulk density
l_a	fragment size
ρ_b	bulk density
A	apoapsis
a	semi-major axis
D	measured crater diameter
D	final crater diameter
D_{sg}	strength-to-gravity transition diameter
E	eccentric anomaly
G	gravitational constant
g	gravitational acceleration
h_L	launch altitude
h_T	terminal altitude
L	launch
M	mass
n	dimensionless mean motion
p	semi-latus rectum
P	periapsis
P	rotational Period
p(x)	probability function
P(x)	cumulative distribution function
R	radius
r	magnitude radius vector from the center of the planetary body
T	terminus

Symbol	Variable
T	travel time
v	velocity
α	exponent/scaling factor
α	impact angle
α, β	rotation angles
δ	projectile density
δ	projected range on the surface
$\Delta \phi$	total ballistic range
ε	eccentricity
ζ	flight path angle
θ	azimuth of ejection
Θ	inclination
μ	standard gravitational parameter
ϱ	radius/radial distance (spherical coordinates)
σ	target density
υ	true anomaly
Φ	azimuth/azimuthal angle
φ	ejection angle
ψ	colatitude
ω	angular speed

1 INTRODUCTION

1.1 THE DAWN MISSION

The thesis is based on data obtained by the Dawn spacecraft as a contribution to the science of the Dawn mission. The following section therefore describes the mission basics along with the instruments onboard the spacecraft and the two bodies of interest in the asteroid belt. All relevant results of the Dawn science team to date are summarized as a contextual for the work of this thesis.

1.1.1 MISSION OVERVIEW

As described in detail in Russell and Raymond (2011), the Dawn mission was selected in 2001 and the Dawn spacecraft launched in September 2007 to investigate the two most massive bodies in the asteroid belt that formed in the earliest days of the Solar System: the asteroid Vesta and the dwarf-planet Ceres. The mission's aim is to determine present state composition, shape and surface geology of the two bodies and also to identify internal and external forces that shaped them (Russell and Raymond, 2011). With that information, the Dawn mission wants to provide more knowledge about conditions during the early stages of the Solar System and the growth of protoplanets (Russell and Raymond, 2011).

The spacecraft carries three instruments: a Framing Camera (FC), a visible and near-IR spectrometer (VIR), and a gamma ray and neutron spectrometer (GRaND). In this thesis, mostly Framing Camera data was used for the geological mapping. At times, other data sets were included in the discussions for additional information. The following instrument descriptions closely follow the particular instrument publication. The Framing Camera (FC) (Sierks et al., 2011) covers a wavelength range from 400 to 1000 nm. Framing Camera data is mainly used to investigate surface features and surface processes. The camera has one clear filter (F1) and seven band-pass/color filters (F2: 555 nm, F3: 749 nm, F4: 917 nm, F5: 965 nm, F6: 829 nm, F7: 653 nm, F8: 438 nm). Those "band-pass filters are essential for the study of mineralogy and chemical composition" (Sierks et al., 2011) and they are used in addition to VIR spectral results. Various color filter ratios are used for different problems, such as mapping specific minerals (Garry et al., 2014; Reddy et al., 2012). Additionally, the Framing Camera is used for the optical determination of dynamical parameters, such as the rotation and the gravitational field. Furthermore, Framing Camera data is the base for topographic information. Digital terrain models are determined by stereophotogrammetry using area-based multi-image matching in combination with optical geometry of the camera and orbital parameters (Preusker et al., 2016).

The global digital terrain model of Ceres has a lateral resolution of 135 m/pixel. In addition to the band-pass filters of the Framing Camera that provide insight into mineralogy and chemical composition, the mineralogical composition of the surface is investigated with the VIR spectrometer (De Sanctis et al., 2011). The hyperspectral spectrometer operates in a range from near UV (ultraviolet, 0.25 μm) to near IR (infrared, 5.0 μm). The third instrument is the Gamma Ray and Neutron Detector (GRaND) (Prettyman et al., 2011). Its objective is to map the surface elemental composition. Its depth sensitivity is 100 g/cm^2. Besides constituents of silicate minerals, oxide minerals and ices, the instrument is also able to detect products of volcanic exhalation and aqueous alteration processes. It is also sensitive to near-surface hydrogen.

For the two planetary bodies, three main science data acquisition orbits are used: the Survey orbit, the HAMO orbit (High Altitude Mapping Orbit) and the LAMO orbit (Low Altitude Mapping orbit) (Russell and Raymond, 2011). Images taken at the particular Cerean orbits have a resolution of 400 m/pixel, 140 m/pixel and 35 m/pixel (Roatsch et al., 2016a; Roatsch et al., 2016b; Roatsch et al., 2017). A mapping campaign was conducted for both bodies. For these campaigns, 15 individual quadrangles were mapped by different scientists.

1.1.2 The Asteroid Belt

The asteroid belt with its two most massive objects Vesta and Ceres is located between Mars and Jupiter and has a total current mass of ~0.05 lunar masses (Krasinsky et al., 2002). The main belt is located between 2.1 and 3.3 AU from the sun (Levison et al., 2009). The classification of asteroids is based on their spectral properties, their albedo and composition (Blair, 2002). According to this classification, the three main types are: C-type asteroids (carbonaceous, 75% of all known asteroids), S-type asteroids (siliceous, 17% of all known asteroids) and M-type asteroids (metallic) (Blair, 2002). One formation model that explains the current state of the asteroid belt is the Grand Tack model. It proposes that the migration of Jupiter inward to the sun and back outward with Saturn depleted the asteroid belt region and then repopulated it (Walsh et al., 2012). The asteroid belt is not uniformly filled. There are gaps that correspond with orbital resonances with the giant planets (Minton and Malhotra, 2009). The distance in the protoplanetary disk where the temperature is "low enough for water to condensate as ice" is called the snow line (Hsieh and Jewitt, 2006). Ceres and the asteroid Vesta formed during the early days of the Solar System and are presumably some of the few intact protoplanets left (Castillo-Rogez and McCord, 2010; Russell and Raymond, 2011). Ceres and Vesta underwent a thermal evolution by the decay of radionuclides that led to a differentiation (Coradini et al., 2011). They are also witnesses of a violent collisional history (O'Brien and Sykes, 2011). Their accretion was probably interrupted by

the formation of Jupiter (Prettyman et al., 2003). Because of their compositional differences (rocky Vesta, ice-rich Ceres), it has been suggested that they formed on the opposite side of the snow line (O'Brien and Sykes, 2011).

1.1.3 The Geology of Vesta

Between July 16, 2011 and September 5, 2012, the spacecraft orbited the asteroid Vesta. Observations, summarized in Russell et al. (2013), show that the composition of Vesta is in good agreement with what is expected for the parent body of the HED (Howardite, Eucrite, Diogenite) meteorites. Vesta is differentiated with an iron core in its center and a crust that consists of eucrites and diogenites (De Sanctis et al., 2012; Russell et al., 2012). Its northern hemisphere is more heavily cratered than its southern hemisphere which, in contrast, displays two ancient basins (Russell et al., 2013).

1.1.4 The Geology of Ceres

Ceres was discovered in 1801 by Giuseppe Piazzi (Pilcher, 1979). Ceres orbits the sun at a distance of 2.767 AU with an inclination of 9.7 degrees (McCord and Sotin, 2005) and an orbital period of 1682 days (NASA). Ceres has a mean radius of 476 km (Thomas et al., 2005) and a rotation period of 9.076 hours (Lagerkvist and Magnusson, 1990). Ceres is a tri-axial ellipsoid with a mean density of 2162 kg/m^3 (Park et al., 2016). Since 2006, Ceres is classified as a dwarf planet. A dwarf planet orbits the sun and has enough mass to be of nearly spherical shape, but not large enough to clear its orbital path (Seeds and Backman, 2015). Earth observations indicated a low-albedo body (Rivkin et al., 2011). Additionally, observations by the Hubble Space Telescope predicted a geologically differentiated body (Thomas et al., 2005) and thermodynamic models proposed a water-rich mantle (Castillo-Rogez and McCord, 2010; McCord and Sotin, 2005).

The Dawn data revealed new insights into the composition, surface structure and surface forming processes of Ceres. Impact craters are the "most prevalent" features on the surface (Buczkowski et al., 2016) (Fig. 1-1). Ceres reveals impact craters ranging from fresh to highly degraded morphologies with craters that exhibit polygonal shapes and various inner structures, such as peaks, pits, bright spots and smooth crater floors (Hiesinger et al., 2016). In contrast to the dark surface of Ceres, there are a localized high-albedo features associated with craters (Nathues et al., 2015). The most famous spots are located at the crater floor of the 92-km Occator crater (239.33°E and 19.82°N). Hiesinger et al. (2016) estimate the simple-to-complex transition diameter between 7.5 and 12 km and find that basins larger than 300 km in diameter are absent.

In addition, Ceres reveals local-scale linear structures, such as floor-fractured craters and kilometer-scale lineaments, either impact-related or the result of crustal uplift (Buczkowski et al., 2016; Scully et al., 2017). Landslide morphologies inside of craters and outside suggest a surface that is rich in water ice (Schmidt et al., 2017). Gravity and shape data sets show that Ceres is partially differentiated and has a rocky core and a volatile-rich shell (Park et al., 2016). The variation of topography is ~17 km (Fig. 1-2).

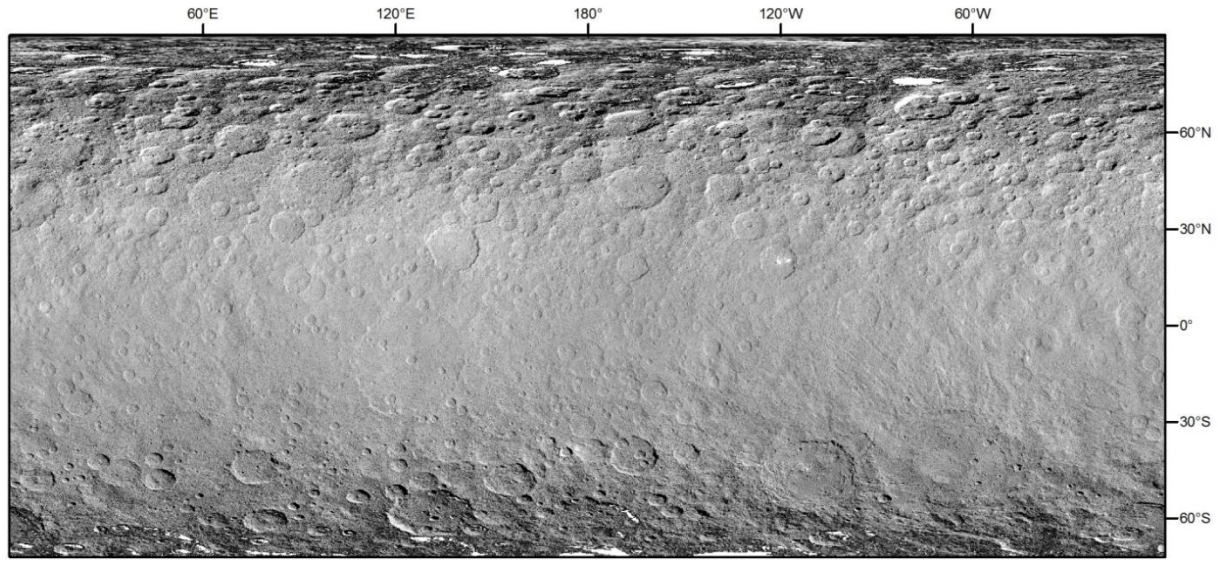

Fig. 1-1. The global LAMO clear filter mosaic of Ceres

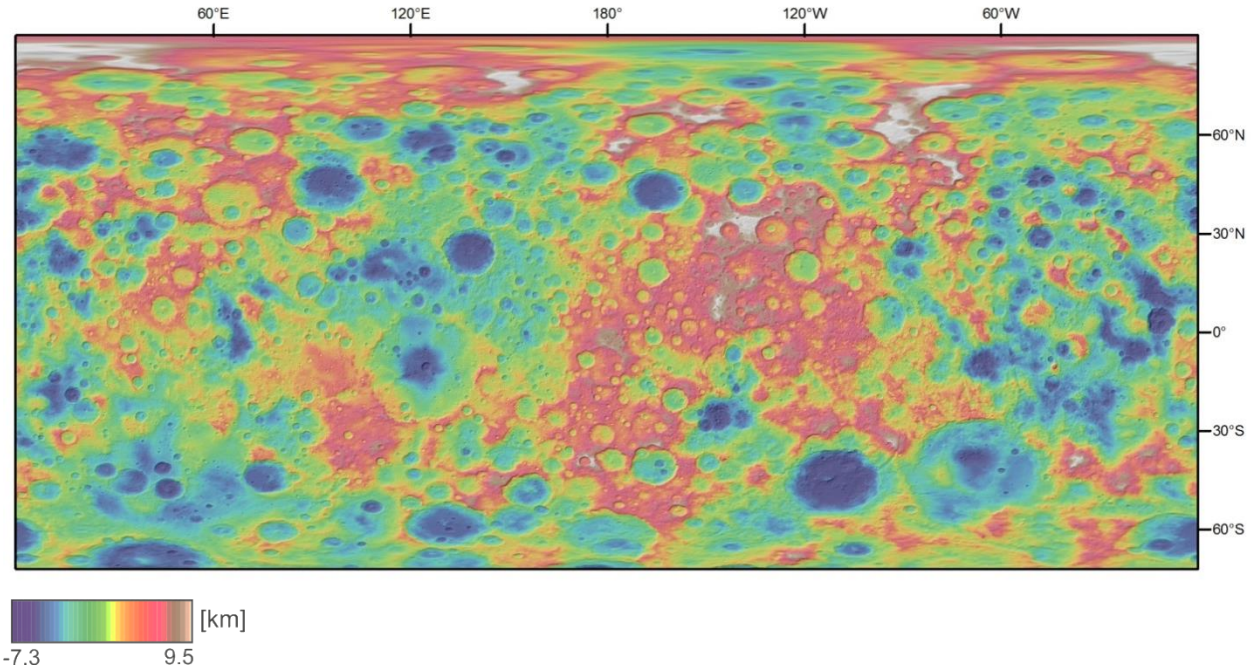

Fig. 1-2. The global digital elevation model with a resolution of 135 m/pixel (50% transparency) on top of a grayscale hillshade. Elevations refer to a biaxial ellipsoid (482x482x446 km) (Preusker et al., 2016).

Rheology constraints revealed by surface topography propose that Ceres might have had a global subsurface ocean in the past (Fu et al., 2017). Ceres' shallow surface, a mechanical strong crust, consists of a mixture of rock (carbonates/phyllosilicates), salts and/or clathrates and up to 40% water ice by volume (Bland et al., 2016; Ermakov et al., 2017; Fu et al., 2017). Viscous relaxation, occurring only at longer wavelengths, is limited (Bland et al., 2016; Ermakov et al., 2017). Locally, Ceres exhibits organic material (De Sanctis et al., 2017a). Bright spots of different sizes and slightly different compositions are observed all over Ceres and 90% are impact related (Palomba et al., 2017). Whereas the average surface of Ceres consists of Mg-phyllosilicates and ammoniated clays and the abundance of Mg-Ca carbonates is reduced, some bright spots can have a different albedo and a different elemental proportion with a higher carbonate abundance and a depletion in phyllosilicates (De Sanctis et al., 2016). Spectral data shows, for instance, that the prominent bright spots in the Occator crater mainly consist of sodium carbonate (De Sanctis et al., 2016). Sulfates might also contribute to Ceres' spectral signature (Bu et al., 2017). Water vapor related to Ceres was first reported in 2014 with measurements from the Herschel Space Observatory (Küppers et al., 2014). Dawn data suggests that there might be active sublimation of the bright spots, for instance in Occator (Nathues et al., 2015). Furthermore, water absorptions have been detected by the VIR instrument (Combe et al., 2016) inside a 10-km crater called Oxo (360°E, 42°N). Moreover, permanently shadowed craters at polar latitudes that also reveal bright deposits could be cold-traps for water ice (Schorghofer et al., 2016), since one of those deposits was spectroscopically identified as water ice (Platz et al., 2016b). Water ice is also likely to play a role in the formation of the pits on Ceres (Sizemore et al., 2017). Lobate morphologies are similar to ice-rich flows on other planetary bodies and indicative for ground ice (Schmidt et al., 2017). Dawn data is also used to investigate interior processes. One the most distinct surface features of Ceres is the tholus Ahuna Mons, a 17-km-wide and 4-km-high domical mountain with steep flanks and a slightly depressed summit (Ruesch et al., 2016). Cryovolcanism has been suggested as a mechanism that has shaped surface landforms, such as Ahuna mons and flow features (Krohn et al., 2016; Ruesch et al., 2016). Floor-fractures in craters, but also crater-unrelated regional fractures support the theory of cryovolcanic uplifting (Buczkowski et al., 2018; Scully et al., 2017).

Ceres reveals a couple of specifically interesting craters that will be briefly discussed below. In the southern hemisphere, there are two large basins next to each other: Yalode (260 km, 292.48°E, 42.58°S) and Urvara (170 km, 249.24°E, 45.66°S). The geomorphology of the two craters is discussed in Crown et al. (2018). Absolute age determination reveals that the Yalode crater is slightly older (580 ± 40 Ma) than the Urvara impact (550 ± 50 Ma). Especially Urvara ejecta dominates the surrounding area in the form of smooth deposits. The geologic mapping reveals

that ejecta of those two basins can extend far beyond the adjacencies. Kerwan (280 km, 123.99°E and 10.77°S) is the largest impact basin on Ceres and is discussed in detail in Williams et al. (2018b). The basin is filled and surrounded by smooth material that is interpreted as impact-induced melting. Occator is one of the most interesting craters on Ceres, because of its highly fractured crater floor (Buczkowski et al., 2018), its bright deposits in its interior (Nathues et al., 2015) and its flow features (Krohn et al., 2016) that encourage theories about cryovolcanism. One of the youngest craters is Haulani crater (34 km, 10.77°E and 5.8°N), which also shows a variety of flow features and is especially eminent in color ratios (Krohn et al., 2018).

1.2 MOTIVATION

As part of the global mapping campaign, the geologic map of the Sintana quadrangle, one out of 15 mapping quadrangles, is one of the first tools to provide an understanding of the surface composition and the geologic evolution of the dwarf planet Ceres. Geologic mapping is a tool to assess interior and exterior processes, such as volcanism, diapirism and subsurface composition by identifying the accompanying units.

The geologic mapping of the Sintana quadrangle reveals structures, such as secondary crater chains, overprinting by large impact craters and boulders and indicates an asymmetric ejecta deposition. Those observations are even more distinct in other regions of Ceres in the vicinity of large impact craters. Quadrangle and global color composites (Fig. 1-3) that are ratios of Framing Camera filters, show asymmetric patterns and linear structures associated with impact craters (Stephan et al., 2017a). For instance, Occator crater (239.3°E, 19.8°N) is characterized by an asymmetric distribution of distal continuous ejecta (Nathues et al., 2017). In addition, there are long-ranging rays that apparently originate from craters. Those features are classified in bluish colors in color-coded images (Fig. 1-3, lower). Bluish colors represent a negative spectral slope (Stephan et al., 2017a) and blue-colored areas are associated with fresh features (Schmedemann et al., 2016) that vanish with time. Stephan et al. (2017a) suggest that the bluish material was either exposed by the impact process or generated by the impact itself. The reddening of the slope with time is explained by space weathering. A preliminary numerical study of the Urvara/Yalode impact by Schmedemann et al. (2017) suggests that the fast-rotating, low-gravity regime of Ceres influences material deposition to a great extent. The goal of this study is to further evaluate this hypothesis. Thus, in addition to the geologic mapping, ballistic calculations are used to test, whether the fast rotation of Ceres is the cause for irregular distributed surface structures in order to explain observations in the Sintana quadrangle and global observations.

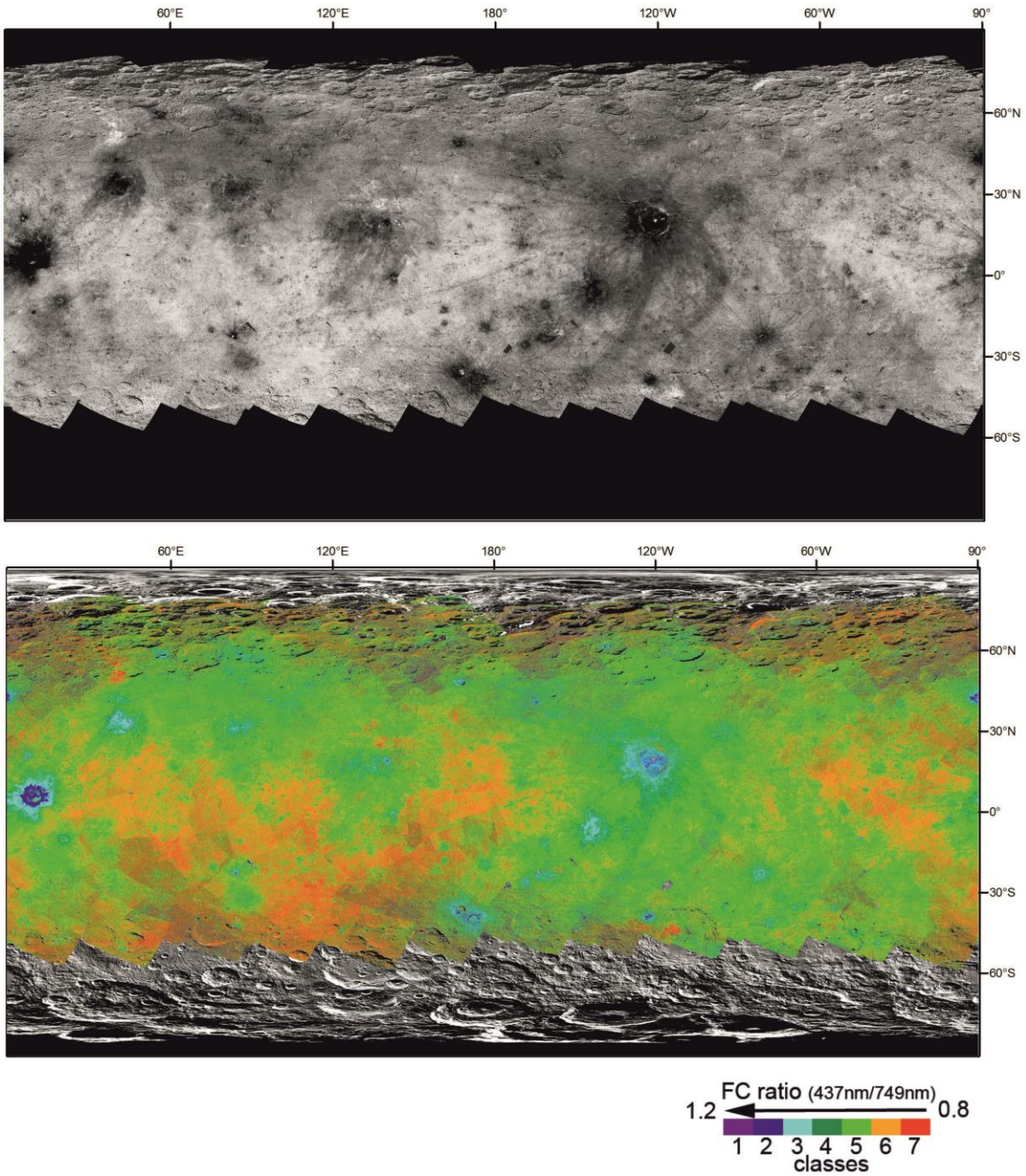

Fig. 1-3. Color filter images of Ceres that illustrate supposable irregular ejecta deposits. The upper image shows a ratio of two filters (F8/F3) produced with images at HAMO resolution. The lower image shows a filter ratio (F8/F3) produced with images at HAMO resolution on top of a clear filter LAMO mosaic. Those ratios are arranged in color-coded classes. Images prepared by K. Stephan.

1.3 Structure of the Thesis

The thesis is organized in six chapters. The first two chapters cover the introduction, the methods and the scientific background. The thesis includes peer-reviewed articles that are included as chapters. The author's contribution is indicated below.

Chapter 3 has been published as F. Schulzeck, K. Krohn, I. v. d. Gathen, N. Schmedemann, K. Stephan, R. Jaumann, D.A. Williams, D.L. Buczkowski, S.C. Mest, J.E.C. Scully, E. Kersten, K.-D. Matz, A. Nass, F. Preusker, T. Roatsch, C.A. Raymond, C.T. Russell, 2018. Geologic mapping of the Ac-11 Sintana quadrangle: Assessing diverse crater morphologies. Icarus. 316, 154-166. https://doi.org/10.1016/j.icarus.2017.12.007. It describes the geologic mapping of a part of Ceres' southern hemisphere and the interpretation of the observed features. The authors individual contributions are as follows: The mapping was done by the author of the thesis and the text and all figures have been prepared by the author of the thesis as well. The mapping database and instructions for mapping by using ArcGIS were provided by A. Naß. N. Schmedemann assisted with discussions about crater counting and absolute age determination and gave instructions to the software CraterStats and provided the newest production functions for Ceres. Several coauthors proofread the manuscript and helped to restructure the text and sharpen the argumentation. D. Williams, J. Scully and C. Russell especially helped as native speakers to improve the language. Mosaics were provided by T. Roatsch and E. Kersten and the DTM was calculated by F. Preusker.

Chapter 4 discusses the ballistic emplacement of ejecta on Ceres in general in comparison with other bodies. It evaluates the effect of crater location, crater size and impact geometry. Global re-impact sites are illustrated for selected craters on Ceres. For those craters, expected particle sizes are estimated as well.

Chapter 5 has been published as F. Schulzeck, S.E. Schröder, N. Schmedemann, K. Stephan, R. Jaumann, C.A. Raymond, C.T. Russell, 2018. Global and local re-impact and velocity regime of ballistic ejecta of boulder craters on Ceres. Planetary and Space Science. 153, 142-156. https://doi.org/10.1016/j.pss.2018.02.004. It describes the ejecta patterns as a function of velocity produced by boulder craters. Additionally, the distribution and velocities of those boulders are investigated. The authors individual contributions are as follows: The coding was done by the author of the thesis and text and figures have been prepared by the author of the thesis as well. Especially S. Schröder helped with detailed proofreading and helpful discussions about size-frequency distributions of boulders. N. Schmedemann helped with discussions about

ballistic calculations and input parameters. The other co-authors provided additional comments about manuscript structure and language.

The final chapter discusses the meaning of the findings of the thesis, puts the results into a broader context and provides an outlook for further research.

2 BACKGROUND AND METHODS

The following chapter includes a detailed discussion about all methods and crucial derivations of equations as well as important background information about the topics of planetary sciences that are relevant for this work. Parts of the following methods are also described in short in the method sections of the previously published papers in chapter 3 and 5.

2.1 PLANETARY MAPPING

Planetary geologic mapping is a tool to assess the planetary body's surface and shallow subsurface in order to understand its geologic evolution. The stratigraphy that is derived by the geologic mapping will provide insights in endogenic and exogenic processes that formed the planetary surfaces (e.g. Tanaka et al., 2009; Wilhelms, 1990). After Batson et al. (1990), planetary cartography started in the pre-photographic era. The first sketch maps of Mars and Moon were already conducted in the 17th century. More information could be gained with the start of practical photography in astronomy at the end of the 19th century. Planetary mapping reached a new level with the availability of spacecraft data in the second half of the 20th century. In the late 1990th, planetary scientists started to use geographical information systems (GIS) for their data analyses (v. Gasselt and Nass, 2011).

A global geologic mapping campaign was already conducted for the asteroid Vesta (Williams et al., 2014). The description of the mapping campaign for Ceres closely follows Williams et al. (2018a). The mapping campaign at Ceres was an iterative process. Starting from survey orbit data, first geologic and stratigraphic information were provided and refined with increasing spatial resolution. The cartographic products include a global map, 4 hemispheric maps and 15 regional quadrangle mosaics. The latter are based on FC clear filter mosaics, processed by the German Aerospace Center (DLR). First maps were produced with HAMO mosaics. Supplemental data includes digital elevation models, photometrically corrected mosaic, color composites and data from the VIR and GRaND instruments. The goal of the mapping was to determine the geologic processes that produced the identified units. The quadrangle maps were produced with the ArcGIS 10 software. Base data and feature layers according to the USGS standards (USGS, 2006) were provided by Naß et al. (2015). Guidelines were discussed and updated with the mapping process. Absolute ages were determined using the ArcGIS crater counting extension CraterTools (Kneissl et al., 2011) and the software CraterStats (Michael and Neukum, 2010; Michael, 2013) to derive ages from size-frequency distributions. A more detailed description of the process can be found in the mapping publication in section 3.2.

2.1.1 IMPACT CRATERING

Impact craters are the most important structures on planetary surfaces that help to gain information about surface ages, subsurface processes and composition, because they occur in various shapes depending on the subsurface properties, impact energy and geometry and may excavate subsurface units (Osinski and Pierazzo, 2012). In this thesis, impact craters are investigated during the geologic mapping and used as a tool to determine Ceres' surface composition and to estimate ages of geologic units. It is also investigated how ejecta contributes to the global geology.

2.1.1.1 The Impact Process

The process of impact cratering can be divided into three sequences that were first proposed by Gault et al. (1968): The compression stage, the excavation stage and the modification stage. The following description closely follows Melosh (1989). When the impact contacts the planetary surface, kinetic energy is transferred as shock waves that propagate into target and projectile. The energy release may result in the complete melting and vaporization of the projectile and shock metamorphism, melting and/or vaporization of the target material.

In the second stage, the shock wave leads to the radial excavation of target material that is called ejecta. A transient cavity is the result. The transient cavity is divided into an upper "excavated zone", where the material is ejected beyond the cavity and a lower "displaced zone", where the material forms the base of the expanding cavity (Osinski and Pierazzo, 2012). Ejecta is divided into continuous and discontinuous ejecta. On airless bodies, ejecta is emplaced ballistically (Melosh, 1989). An atmosphere interacts with purely ballistic trajectories due to winds/turbulences and the frictional drag (Schultz, 1992). After Kurosawa et al. (2018) the ejection process during the excavation stage can be classified into three stages: jetting (early stage, ejection velocity higher than impact velocity), spallation (lightly shocked, high-velocity ejecta) and normal excavation (ejection velocity lower than impact velocity) that depend on ejection timing, ejection velocity, pressure and location. Ejecta can be divided into proximal ejecta deposits in the vicinity of an impact crater and distal ejecta that can be found distant from the crater (Osinski and Pierazzo, 2012).

The third phase is the modification stage. During this stage the transient crater collapses under gravity. Processes of this stage include debris slides, slump terraces and the rise of central peaks or peak ring formation (Melosh, 1989).

2.1.1.2 Classification of Impact Crater Morphologies

The two most important crater types are simple and complex craters. The following descriptions closely follow the terminology in Melosh (1989). The transition between simple and complex craters is defined by a threshold diameter that is specific to a planetary body. It scales inversely to the gravitational acceleration of the parent body. At some point, the crater collapses under gravity. Simple craters are bowl-shaped and have a circular, raised rim and a smoothly decreasing interior slope that leads to a parabolic interior profile (Fig. 2-1). Their rim-to-floor depth ratio is approximately 1/5. The second morphologic crater shape is a complex crater. Complex craters are shallower than simple craters and usually show some or all of the following features: terraces, a central peak, landslide deposits, a flat floor and a scalloped crater rim (Fig. 2-1). Other types include peak-ring craters, multi-ringed basins, central pit craters on icy satellites, elliptical craters due to highly oblique impacts and polygonal craters due to strong regional joint trends.

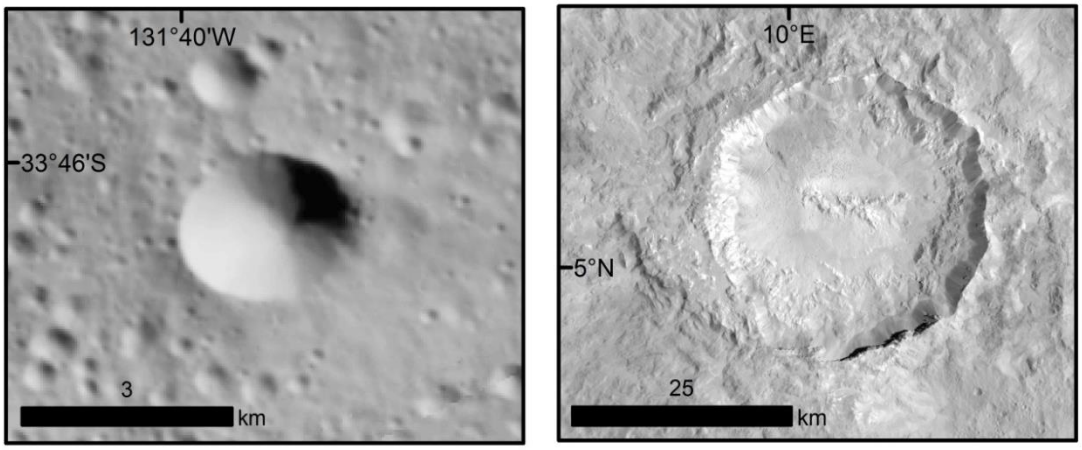

Fig. 2-1. Classification of impact craters on Ceres. An unnamed simple (left) and the complex crater Haulani (right, 34 km) on Ceres

2.1.1.3 Secondary Craters

After McEwen and Bierhaus (2006), secondary craters are "produced by fallback of high-velocity ejecta blocks" of larger impact craters and their occurrence depends on the planetary body's atmosphere, the surface gravity and resurfacing rates as well as the impact angle and other impact factors. Secondary craters that are deposited with and around the time of the primary impact bias crater counts (McEwen and Bierhaus, 2006). McEwen and Bierhaus (2006) argue that the steep size-frequency distributions (SFD) of secondary craters can be explained by the size-velocity relationship of impact ejecta. Those craters are not sufficient for age dating because they formed nearly simultaneously with their primary crater (McEwen and Bierhaus, 2006). In addition, the minimum velocity for secondary crater formation is assumed to be 200 m/s (McEwen and

Bierhaus, 2006). Even if some of those secondary craters occur in chains and clusters, there might be distant uncluttered secondaries that can hardly be distinguished from primary craters (Shoemaker, 1962). At least below a crossover diameter, secondary craters could dominate the crater populations (McEwen and Bierhaus, 2006). The authors conclude that there is not yet a perfect solution in the distinction between primary and secondary craters. There are only assisting approaches, for example to only use craters above the crossover diameter that is defined as the change in slope of the SFD.

2.1.1.4 Ejecta Blocks

Boulders or ejecta blocks are positive relief features of different shapes and a part of a crater's ejecta (e.g. Lee et al., 1996). Diameter size-frequency distributions (SFDs) of boulders are studied on various other bodies, because those blocks are the projectiles that produce secondary craters when they impact into the surface (Xiao and Strom, 2012). The knowledge of boulder sizes might allow conclusions about secondary crater sizes and the other way around. In consequence, SFDs of boulders are often as steep-sloped as SFDs of secondary craters (Jiang et al., 2015; Krishna and Kumar, 2016). Additionally, SFDs are studied, because they provide information about the degree of rock fragmentation and therefore about underlying effects, such as impact rates and other resurfacing processes. The SFDs of boulders of the asteroid Toutatis, for instance, have steeper slopes than those of the asteroid Itokawa, which is interpreted to be the result of a different preservation state of the boulders (Jiang et al., 2015). On the comet Churyumov-Gerasimenko, varying block SFDs for different parts of the comet are explained by processes, such as fracturing due to thermal stresses, outgassing and burial by debris (Pajola et al., 2015). On the Moon, Bart and Melosh (2010b) found that larger boulders of large craters are ejected at very low velocities. In contrast, large boulders of smaller crater are ejected at a wider range of velocities. Bart and Melosh (2010a) also found that there is an inverse relationship between ejection velocity and regolith depth. Most of the boulders are destroyed via catastrophic disruption by meteorites (e.g. Basilevsky et al., 2013; Hörz et al., 1975). Basilevsky et al. (2015) estimated that the life time of meter-sized boulders on Ceres and Vesta is 1/30 of the survival time of boulders on the Moon, because of a higher meteorite flux.

2.1.1.5 The Age of Planetary Surfaces

The basic idea of a chronological classification of planetary surfaces is that the age of a surface is related to the number of its impacts assuming a constant impact rate (Michel and Morbidelli, 2007). To determine surface ages, knowledge about the population of projectiles, such as sizes and orbits, and the still not fully understood impact cratering process that is described by scaling

laws is required (Michel and Morbidelli, 2007). Crater distributions are moreover influenced by mechanisms, such as erosion and plate tectonics (e.g. Earth), atmospheric effects (e.g. Venus) and potential secondary craters (Michel and Morbidelli, 2007). The authors note that so far, an absolute chronology up to 3.8 Ga has yet been established for lunar craters only by a calibration with lunar samples from the Apollo and Luna missions. While there has been a relatively constant impact flux on the Moon during the last 3.6 Ga (Shoemaker, 1998), there has been a spike in the cratering rate at ~3.85 Ga ago, which is known as the Late Heavy Bombardment (LHB) (Koeberl, 2003). The most recent explanation by Gomes et al. (2005) proposes that a rapid migration of the four giant planets followed by the destabilization of the surrounding planetesimal disk triggered this event.

Closely following the description in Fassett (2016), the first step to derive an age for a region of a planetary surface is to measure the crater population by defining the area of interest, mapping all superposed craters and measuring the diameters of the complete crater population. The crater population is typically represented by size-frequency plots (cumulative, differential or relative). The next step is to determine the age from the measured size-frequency distribution by finding a model of "how fast craters of a given size are produced per unit area" (Fassett, 2016). Therefore the author defines two quantities: the cumulative density as the total number of craters per unit area and its time derivative, the cratering production rate. The cumulative density is the product of the time-independent production function and the integrated form of the chronology function and describes the isochrone. The crater production rate varies between planetary bodies because of differences in impactor and target properties and local inhomogeneity, such as a geographic variation of the impact rate.

There are two approaches to establish a planetary chronology. A widely used approach for terrestrial bodies is the extrapolation and adaption of lunar records (Fassett, 2016). The second method is to derive ages by directly modeling the impactor flux for the target body based on observations of asteroids and comets (Marchi et al., 2009; Tanaka and Hartmann, 2012.). This method is limited by the uncertainties about impact rates in the early stages of the solar system and incomplete observations of objects below 5 km diameter (Schmedemann et al., 2014).

The application of the aforementioned methods beyond the terrestrial planets, like for asteroid belt objects, such as Ceres and Vesta, is more challenging since there is only limited knowledge about the relevant impactor populations (Fassett, 2016). The difference between Vesta and Ceres is that there are no known meteorites that originated from Ceres that would help to calibrate crater counts. In contrast, radiometric dated HED (Howardite, Eucrite, Diogenite) meteorites could be directly linked to Vesta (Binzel and Xu, 1993). There is an ongoing debate about the use

of the right chronology method for objects in the asteroid belt. Schmedemann et al. (2014) scale the lunar production function to impact conditions on Vesta in order to be independent of incomplete projectile observations. O'Brien et al. (2014) argue that scaling the lunar impact rate and chronology function to the asteroid belt "is not based on any specific physical scenario" and produces an "unreasonable large primordial impact rate". They present a chronology that is based on models of the dynamical evolution of the asteroid belt. Publications as part of the Dawn mission to Vesta and Ceres usually report both chronologies (Hiesinger et al., 2016; Schmedemann et al., 2015).

2.2 Ballistics on Planetary Bodies

Ejecta dynamics are used in this thesis to describe the emplacement of ejecta of Cerean craters as a function of rotation. Especially the range and asymmetry of ejecta are of interest. The rotational influence is described by the Coriolis effect.

2.2.1 The Coriolis Effect

The Coriolis force (Eq. 2-1) is a fictitious force (because it is only experienced within the moving system) that acts on objects with the mass m that moves with a velocity $\vec{v}$ relative to a rotating frame with the angular speed $\vec{\omega}$ (Arora, 1981). After Lowrie (2007), the result is an additional centrifugal acceleration with the corresponding force in Eq. 2-1. The direction in which the force acts depends on the velocity components (east-west, north-south, up-down). Horizontal velocity components result in acceleration with both a vertical and a horizontal component. The vertical component is called Eötvös effect. It in- or decreases gravity at a small amount. A vertical velocity component results also in a horizontal deviation. A falling body will be deflected towards east and an upward moving body towards west (Chandrasekar, 2010). Fig. 2-2 illustrates the horizontal deflection of an object that moves parallel to the horizontal plane. In the northern hemisphere, an object will be deflected to the right and in the southern hemisphere it will be deflected to the left of its direction of motion. This effect is maximal at the poles and zero at the equator. A planetary body rotates with a latitude dependent speed which results in a latitude dependent Coriolis force (Gabler et al., 2008).

$$F_c = - 2m (\vec{v} \times \vec{\omega}) \quad (2\text{-}1)$$

.

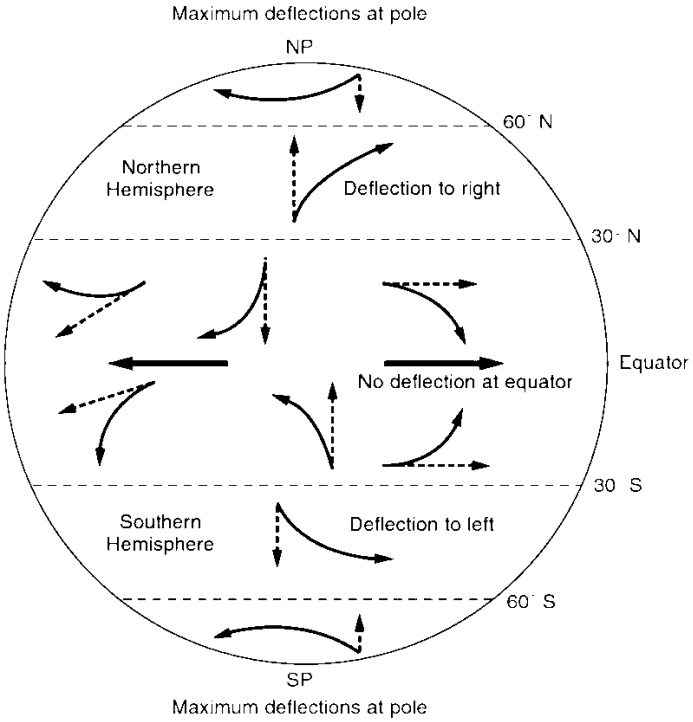

Fig. 2-2. The Coriolis effect acting on horizontal directions of movement. Image by Gabler et al. (2008).

2.2.2 The Fate of Ejecta

Ejecta dynamics are investigated under a variety of aspects. They are helpful, for instance, to quantify the material exchange between different planetary bodies (Alvarellos et al., 2005; Alvarellos et al., 2017; Dobrovolskis et al., 2010). Mass transfer between different planetary bodies influences the age determination of planetary surfaces. Nayak et al. (2016) show that ejecta re-accretion and transfer from large impacts between the Martian satellites Deimos and Phobos can lead to resurfacing of large parts of their surfaces. The analysis of the fate if ejecta is also used to find the source region for specific geologic units (Lorenz, 2000; Wrobel, 2004).

Analytical calculation as in this study are performed for the Earth (Alvarez, 1996; Schedl, 2015), Mercury (Dobrovolskis, 1981), Mars (Wrobel, 2004) and the Moon (Bart and Melosh, 2007; Giamboni, 1959). In addition, numerical models that integrate the particle orbits in the gravity field of the planetary body are widely used (e.g. Alvarellos et al., 2002; Geissler et al., 1996; Lorenz, 2000; Nayak and Asphaug, 2016; Schultz and Wrobel, 2012).

2.2.3 Derivation of Elliptical Trajectories

To analytically analyze the effect of Ceres' rotation on the deposition of ejecta, landing sites for a given number of test particles ware calculated. The calculation of the landing sites in the next section is based on elliptical trajectories that are derived in this section.

The following derivation of ballistic trajectories in a vacuum is taken from Morris (1964). The three base equations that allow the calculation of ballistic trajectories are the equation of the conservation of angular momentum (Eq. 2-2), the conservation of energy (Eq. 2-3) and the equation of an ellipse (Eq. 2-4). Variables include the magnitude radius vector from the center of the planetary body r, the velocity v, the standard gravitational parameter μ, the flight path angle ζ, the semi-major axis a, the true anomaly υ, the semi-latus rectum p, and the eccentricity ε of the elliptical orbit (Fig. 2-3).

$$rv\cos(\zeta) = \sqrt{\mu p} = \text{const.} \tag{2-2}$$

$$v^2 = \mu\left(\frac{2}{r} - \frac{1}{a}\right) \tag{2-3}$$

$$\frac{1}{r} = \frac{1+\varepsilon\cos(\upsilon)}{p} \tag{2-4}$$

The parameters μ, a, p and ε can be calculated as follows:

$$\mu = g_0 r_{planet}^2 \tag{2-5}$$

$$a = \frac{1}{2}(r_A + r_P) = \frac{r_L}{2 - v_L^2} \tag{2-6}$$

$$p = r_L v_L^2 \cos(\zeta_L) \tag{2-7}$$

$$\varepsilon = \sqrt{1 - (2 - v_L^2) v_L^2 \cos^2(\zeta_L)}\,. \tag{2-8}$$

The equations 2-5 – 2-13 use the subscripts L for launch, T for terminus, A for apoapsis (farthest point) and P for periapsis (nearest point). r_A and r_P are the planet-centered radii at apoapsis and periapsis, respectively. The range angle $\Delta\phi_{LA}$ in Eq. 2-9 from launch to the apoapsis is given by the difference in the true anomalies of these two points ($\upsilon_A > \upsilon_L$). Eq. 2-10 provides the range angle from apoapsis to the terminal altitude. The range is given by the difference in the true anomalies of these two points ($\upsilon_T - \upsilon_A$). The total range is then the sum of the two sub ranges

(Eq. 2-11). The equation can be simplified (Eq. 2-13), if the launch and terminal altitude (h_L, h_T) are chosen to be the same.

$$\Delta\phi_{LA} = \upsilon_A - \upsilon_L = \pi - \cos^{-1}\left[\frac{1}{\varepsilon}\left(\frac{p}{r_L} - 1\right)\right] = \cos^{-1}\left[\frac{1}{\varepsilon}\left(1 - \frac{p}{r_L}\right)\right] = \cos^{-1}\left[\frac{1}{\varepsilon}\left(1 - v_L^2\cos^2(\zeta_L)\right)\right] \tag{2-9}$$

$$\Delta\phi_{AT} = \upsilon_T - \upsilon_A = \cos^{-1}\left[\frac{1}{\varepsilon}\left(\frac{p}{r_T} - 1\right)\right] - \pi = \cos^{-1}\left[\frac{1}{\varepsilon}\left(1 - \frac{p}{r_T}\right)\right] = \cos^{-1}\left[\frac{1}{\varepsilon}\left(1 - \frac{r_L}{r_T}v_L^2\cos^2(\zeta_L)\right)\right] \tag{2-10}$$

$$\Delta\phi = \Delta\phi_{AT} + \Delta\phi_{LT} \tag{2-11}$$

$$\Delta\phi = \cos^{-1}\left(\frac{1 - v_L^2\cos^2(\zeta_L)}{\varepsilon}\right) + \cos^{-1}\left(\frac{1 - \frac{r_L}{r_T}v_L^2\cos^2(\zeta_L)}{\varepsilon}\right) \tag{2-12}$$

$$\Delta\phi = 2\cos^{-1}\left(\frac{1 - v_L^2\cos^2(\zeta_L)}{\varepsilon}\right) = 2\tan^{-1}\left(\frac{v_L^2\sin(\zeta_L)\cos(\zeta_L)}{1 - v_L^2\cos^2(\zeta_L)}\right) \tag{2-13}$$

The projected range δ on the surface then is defined as $\delta = \Delta\phi\, R_{planet}$ (Fig. 2-4).

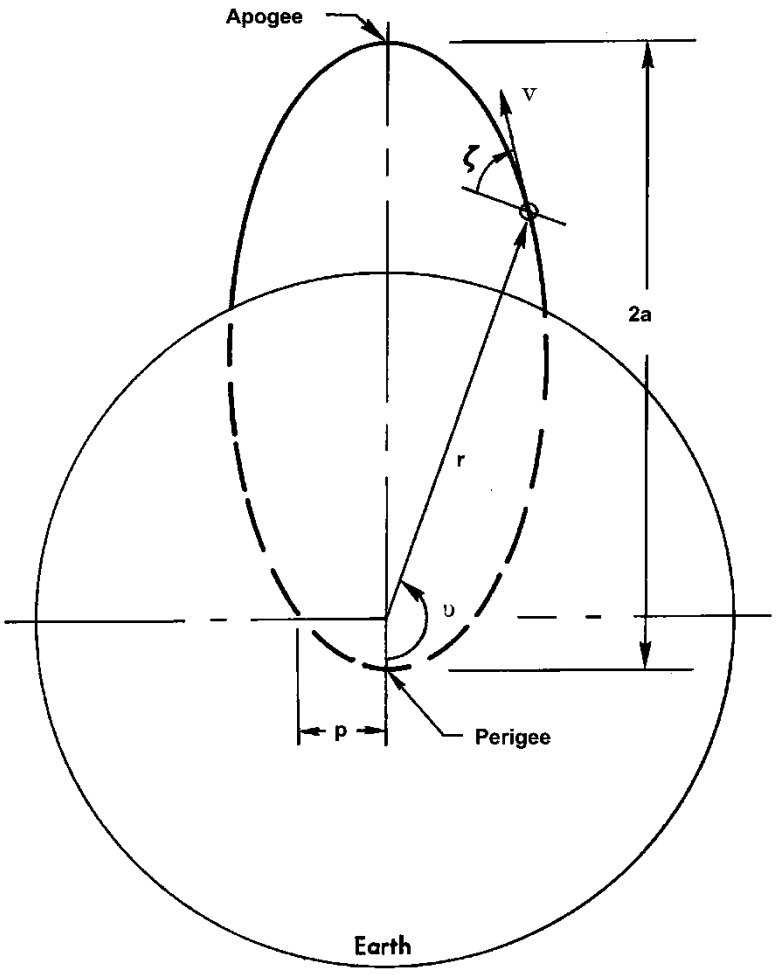

Fig. 2-3. Elliptical geometry adapted from Morris (1964)

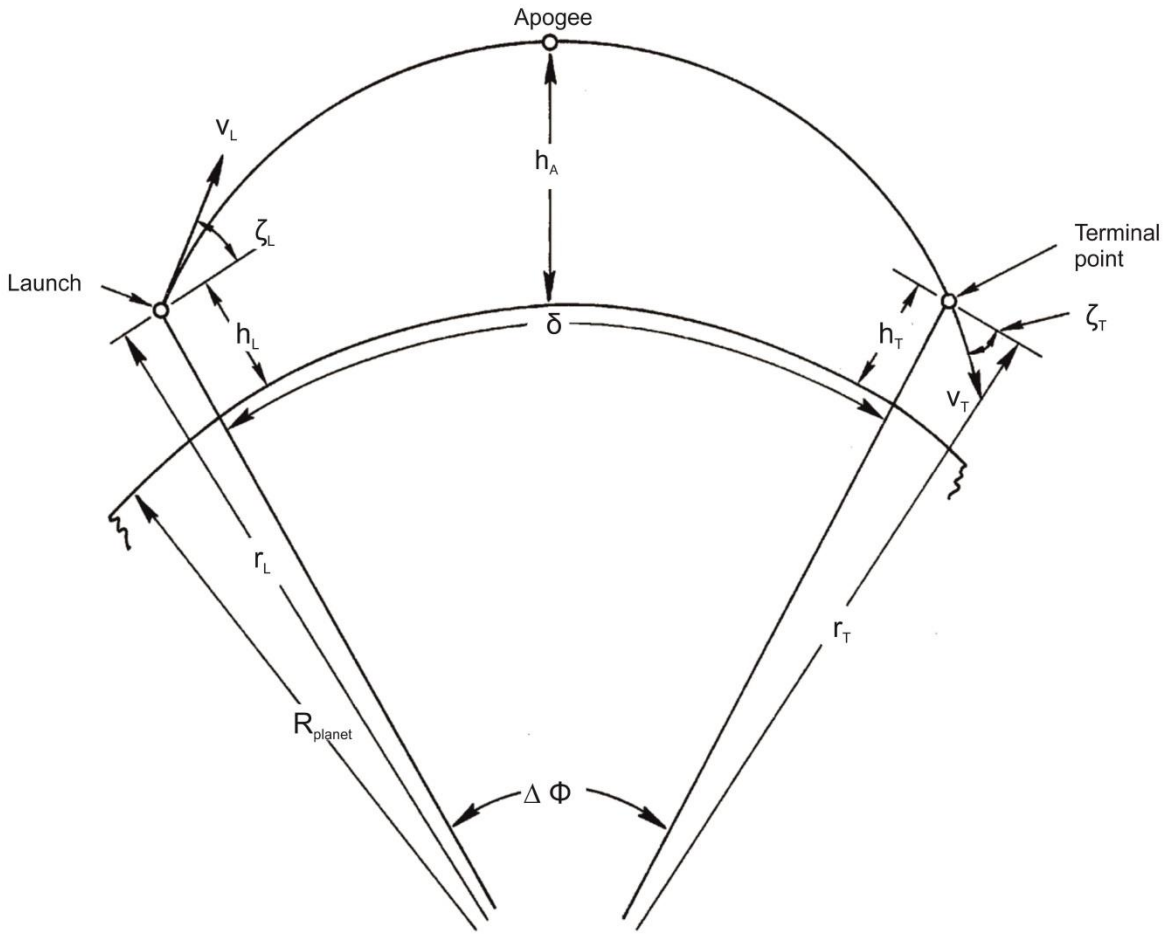

Fig. 2-4. Geometry of ballistic trajectories adapted from Morris (1964). The altitude is h. The launch and terminal altitudes are set to be equal.

2.2.4 Calculation of Particle Landing Locations in a Rotating Planetary System

This thesis follows an approach introduced by Dobrovolskis (1981) to calculate re-impact sites of ballistically ejected particles. The model makes some simplifications: The planetary body is approximated by a sphere. Ceres is nearly spheroidal. It has a polar flattening of 0.075 (Park et al., 2016) and its equatorial axes differ by ≈2 km (Ermakov et al., 2017). In addition, calculations are performed in a vacuum, atmospheric influences are not considered. For Ceres, that assumption is appropriate, because only a very thin and local transient atmosphere might have been detected (Russell et al., 2016). The velocity change during the flight due to gravity is neglected as well as gravitational effects by other planetary objects. To some extend there is ejecta that escapes into orbit, but returns to the surface and subsequently produces so-called sesquinary impacts (Nayak and Asphaug, 2016). Such exceptions are not part of the calculation of velocities below the escape velocity. Furthermore, collisions between fragments are not considered. The calculations are summarized in the following. The initial velocity v of particle with an ejection angle φ (to the

vertical: φ_v=180- φ) and an azimuth θ (measured eastward from the local north) can be split into the following components:

$$v_x = v \sin(\varphi_v) \sin(\theta)$$
$$v_y = v \sin(\varphi_v) \cos(\theta)$$
$$v_z = v \cos(\varphi_v). \quad (2\text{-}14)$$

Calculations are performed in an inertial frame. Inertial frames are fixed or move with a constant velocity, they do not accelerate. A non-inertial reference frame is a frame that is accelerating or rotating. Pseudo-forces, such as Coriolis or centrifugal force act in a non-inertial reference system as an opposite force to the real forces in the inertial system (e.g. Goel, 2007; Jha, 2009). A non-inertial system would be applied, if the observer looks at the trajectory of an ejected particle from the surface of the planetary body. To transform the speed v_0 to the inertial frame, the factor $b= \omega R \sin\psi$, with the colatitude ψ of the ejected particle, is added to the eastward velocity component v_x (Eq. 2-15). The approach chooses dimensionless units of measure to simplify calculations, where the mass M, radius R, gravitational constant G and gravitational acceleration g are set to 1. Accordingly, the escape velocity $v_{esc}= \sqrt{2GM/R} = \sqrt{2}$. The planetary body's bulk density is ϱ_b. The dimensionless angular speed ω is given by $\omega = 3.3hr/\sqrt{\varrho_b}\, P$, where P is the period of rotation.

$$v_0 = \sqrt{v^2 + b^2 + 2vb \sin(\varphi_v) \sin(\theta)} \quad (2\text{-}15)$$

The launch angle φ_{v0} and azimuth θ_0 in the inertial space are given in Eq. 2-16 and 2-17. For a negative eastward component of the initial velocity, the new azimuth takes values between π and 2π.

$$\varphi_{v0} = \cos^{-1}\left(\frac{v}{v_0}\cos(\varphi_v)\right) \quad (2\text{-}16)$$

$$\theta_0 = \cos^{-1}\left(\frac{\tan(\varphi_v)}{\tan(\varphi_{v0})}\cos(\varphi_v)\right) \quad (2\text{-}17)$$

The horizontal component of the velocity in inertial space is given by:

$$v_h = v_0 \sin(\varphi_{v0}). \quad (2\text{-}18)$$

The trajectory is given by the polar equation of the ellipse in Eq. 2-4. The eccentricity ε, semi-major axis a, the eccentric anomaly at the starting point E, the dimensionless mean motion n, and the travel time T are defined in Eq. 2-19 – 2-23. Inserting Eq. 2-18 in Eq. 2-13 gives a different notation of the distance of flight in Eq. 2-24. The colatitude ($CoLat_{land}$) and the longitude (Lon_{land}) of the re-impact location with no rotation are given in Eq. 2-25 and 2-26.

$$\varepsilon = \sqrt{1-v_h^2(2-v_0^2)} \tag{2-19}$$

$$a = \frac{1}{2 - v_0^2} \tag{2-20}$$

$$E = \cos^{-1}\left(\frac{v_0^2 - 1}{\varepsilon}\right) \tag{2-21}$$

$$n = \sqrt{\frac{GM}{a^3}} \tag{2-22}$$

$$T = 2\left(\pi - E + \varepsilon \sin(E)\right)a^{\frac{3}{2}} \tag{2-23}$$

$$\Delta\phi = 2\cos^{-1}\left(\frac{1 - v_h^2}{\varepsilon}\right) \tag{2-24}$$

$$CoLat_{land} = \cos^{-1}\left(\cos(\Delta\phi)\cos(\psi) + \sin(\psi)\sin(\Delta\phi)\cos(\theta_0)\right) \tag{2-25}$$

$$Lon_{land} = \begin{cases} \cos^{-1}\left(\dfrac{\cos(\Delta\phi) - \cos(\psi)\cos\left(CoLat_{land}\right)}{\sin(\psi)\sin(CoLat_{land})}\right); & \text{for } 0 \le \theta_0 \le \pi \\ (-1)\cos^{-1}\left(\dfrac{\cos(\Delta\phi) - \cos(\psi)\cos\left(CoLat_{land}\right)}{\sin(\psi)\sin(CoLat_{land})}\right); & \text{for } \pi < \theta_0 < 2\pi \end{cases} \tag{2-26}$$

The longitude of the final impact, considering the rotation, is then: $Lon_{final} = \left(Lon_{land} - \omega T\right) + Lon_{crater}$.

2.2.5 START PARTICLE CONFIGURATION

For the calculation of particle landing locations, test particles are ejected, and their trajectories calculated. The number of test particles does not reflect the actual amount of ejecta material. Ejecta is usually launched from inside the crater, between the projectile radius R_p and the transient crater radius R_t. Therefore, test particles, for a given crater diameter, are randomly distributed within the limits of transient crater radius and projectile radius on a unit sphere (radius = 1). The relation between Cartesian (x, y, z) and spherical coordinates (ϱ, Θ, Φ) is defined in Eq. 2-27 with the radius ϱ, the inclination Θ, the azimuth Φ (Zwillinger, 2011).

$$x = \varrho \cos(\Theta) \sin(\Phi)$$
$$y = \varrho \sin(\Theta) \sin(\Phi)$$
$$z = \varrho \cos(\Phi) \tag{2-27}$$

The following equations produce n random points uniformly distributed on the surface of a unit sphere (Steeb, 2004):

$$z = \text{rand}(n)2 - 1$$
$$\Theta = \text{rand}(n)2\pi$$
$$x = \sqrt{1 - z^2} \cos(\Theta)$$
$$y = \sqrt{1 - z^2} \sin(\Theta). \tag{2-28}$$

Particles are ejected from a ring between two predefined radii, at which R_p is the inner (projectile) and R_T the outer (transient crater) radius. Both radii are normalized by the radius of Ceres. The individual small circle z-coordinates are given in Eq. 2-29.

$$z1 = \text{rand}(n) \left(\cos\left(\frac{R_T}{R_{Ceres}}\right) - 1 \right) - \cos\left(\frac{R_T}{R_{Ceres}}\right)$$
$$z2 = \text{rand}(n) \left(\cos\left(\frac{R_P}{R_{Ceres}}\right) - 1 \right) - \cos\left(\frac{R_P}{R_{Ceres}}\right) \tag{2-29}$$

The z-coordinates of the points in the ring between the two circles are given by the pseudocode in Eq. 2-30.

$$z = z1 \; (z1 > \max(z2)) \tag{2-30}$$

As a result, the launch locations in the crater are obtained for a crater located at the South Pole. For other locations, the points need to be rotated and centered at the crater's coordinates as illustrated in Fig. 2-5. The colatitude of the crater center is α and the center longitude is β. After Wille et al. (2013), the rotation matrix for a rotation around the y-axis to place the uniformly distributed random points around the crater center latitude (x', y', z') is then:

$$\begin{pmatrix} \cos(\alpha) & 0 & \sin(\alpha) \\ 0 & 1 & 0 \\ -\sin(\alpha) & 0 & \cos(\alpha) \end{pmatrix} \cdot \begin{pmatrix} x \\ y \\ z \end{pmatrix} = \begin{pmatrix} x' \\ y' \\ z' \end{pmatrix}. \tag{2-31}$$

To rotate the points to the right longitude (x", y", z"), the new coordinates are rotated again, but this time around the z-axis:

$$\begin{pmatrix} \cos(\beta) & -\sin(\beta) & 0 \\ \sin(\beta) & \cos(\beta) & 0 \\ 0 & 0 & 1 \end{pmatrix} \cdot \begin{pmatrix} x' \\ y' \\ z' \end{pmatrix} = \begin{pmatrix} x'' \\ y'' \\ z'' \end{pmatrix}. \tag{2-32}$$

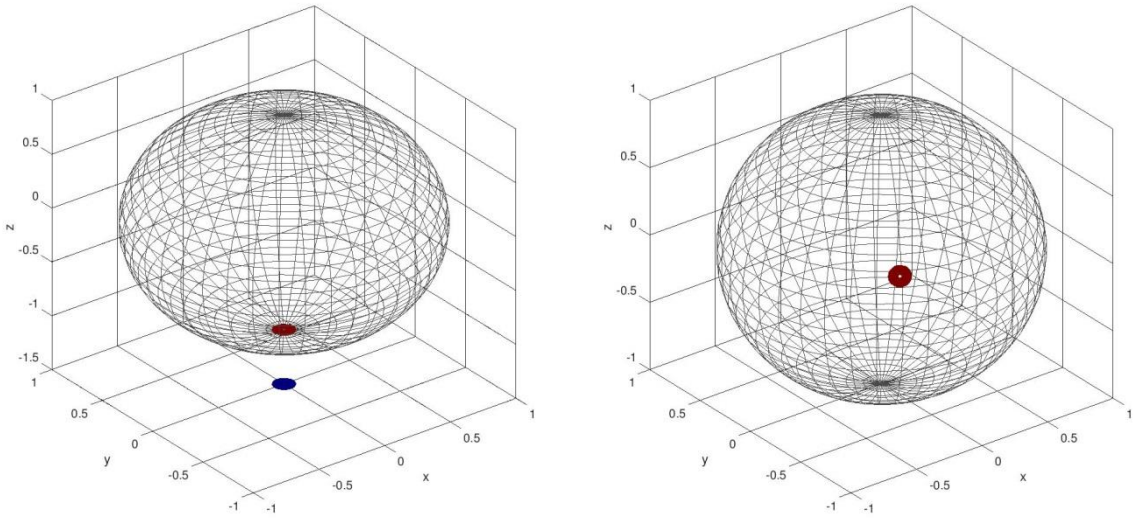

Fig. 2-5. Test particle set-up. Test particles are distributed inside the crater between projectile and transient crater radius. Left) Planar data in comparison with data on the surface of the sphere. Right) Points are rotated to the longitude and latitude of the desired crater.

2.2.6 CRATER SCALING

Crater scaling laws are used to derive the transient crater diameter, the projectile size and the ejection velocity as a function of the distance from the crater center. Impact crater scaling laws defined by theory and laboratory experiments describe the relationship between impactor, target and the resulting impact crater (Werner and Ivanov, 2015). For a detailed analysis see e.g. Ivanov (2001) or Werner and Ivanov (2015).

Croft (1985) defines the transient crater diameter D_t for complex craters using the simple-to-complex transition diameter D_{sc} and the measured crater diameter D by:

$$D_t = D_{sc}^{0.15} D^{0.85}. \tag{2-33}$$

The transient diameter for a simple crater is defined after Werner and Ivanov (2015) as:

$$D_t \approx \frac{D}{(1.25 \pm 0.05)}. \tag{2-34}$$

For scaling the final crater size, Holsapple (1993) draws a distinction between strength and gravity regime, depending on the size of the impactor. For the strength regime, the strength of the target material is large compared to the lithostatic pressure introduced by the crater gravity. It

applies to smaller projectiles. In the gravity regime, the surface gravity dominates the crater modification process. One scaling law that describes the relationship between projectile size and the transient crater diameter is defined by Schmidt and Housen (1987). It makes use of the π-theorem (Buckingham, 1914), which puts parameters in dimensionless groups ("pi-groups") (Dowling and Dowling, 2013). Schmidt and Housen (1987) define the projectile size for a target of nonporous, zero friction rocks by:

$$D_p = D_T \cdot \frac{(g\, D_T)^{0.282}}{\left\{1.16 \left(\frac{\delta}{\sigma}\right)^{\frac{1}{3}} (v_p \sin(\alpha))^{0.44}\right\}^{\frac{1}{0.78}}}. \tag{2-35}$$

D_p is the diameter of the projectile, g the gravitational acceleration of the target body, δ the density of the projectile, σ the target density, v_p the velocity and α the impact angle of the projectile. Another possibility is to incorporate the strength-to-gravity transition into the previous equations (Ivanov, 2008; Neukum and Ivanov, 1994; Schmidt and Housen, 1987). The result is:

$$D_p = D_T \cdot \frac{\left(g(D_T + D_{sg}\right)^{0.282}}{\left\{1.16 \left(\frac{\delta}{\sigma}\right)^{\frac{1}{3}} (v_p \sin(\alpha))^{0.44}\right\}^{\frac{1}{0.78}}}. \tag{2-36}$$

D_{sg} is the strength-to-gravity transition diameter. The crater diameter out of a projectile diameter is calculated with Eq. 2-36. The ejection velocity as function of the crater rim is given in Housen et al. (1983):

$$v(x) = C \sqrt{gR_t} \left(\frac{x}{R_t}\right)^{-e_x} \tag{2-37}$$

,with the particle velocity v, the gravitational acceleration g, the transient crater radius R_t, the distance from the crater center x and the constants C and e_x. Richardson et al. (2005) improved this equation, by allowing the velocity to drop to zero at the crater rim for a gravity-dominated regime:

$$v(x) = \frac{2\sqrt{gR_t}}{(1+e_x)} \left(\frac{x}{R_t}\right)^{-e_x} - \frac{2\sqrt{gR_t}}{(1+e_x)} \left(\frac{x}{R_t}\right)^{\lambda}. \tag{2-38}$$

A value of e_x=2.44 derived for impacts into Ottawa sand by Housen et al. (1983) and the material constant λ=10 according to Bart and Melosh (2010a) for a lunar setting are used, because there are no better constrained material constants for Ceres.

2.2.7 Impact Angle and Ejection Velocity for an Oblique Impact

For the calculation of the particle ejection angle in dependence of the distance from the crater center as well as the angle and direction of the primary impact, equations derived by Richardson et al. (2007) are used. They are based on experimental (e.g. Anderson et al., 2003; Anderson et al., 2004; Cintala et al., 1999; Schultz et al., 2005.) and numerical studies (Collins and Wünnemann, 2007). In a first-order approximation, the ejection angle φ is linearly decreasing with distance x from the impact center (2-39). φ_0 and φ_d are the starting and dropping angles, respectively. Close to the center of the crater at the projectile radius, particles are ejected with higher angles than farther away from the crater center. Particles at the projectile radius are ejected with the highest angle $\varphi_0$and particles at the transient crater radius are ejected with the lowest angle φ_d. Values of $\varphi_0 \approx 52°$ and $\varphi_d \approx 18°$ are taken from Cintala et al. (1999).

$$\varphi(x) = \varphi_0 - \varphi_d \left(\frac{x}{R_t}\right) \tag{2-39}$$

For an oblique impact, the direction θ and angle α of the impactor need to be included. The particle azimuth θ is now measured from the impactor's incoming direction. In consequence, there is a lowering of ejection angles on the downrange side:

$$\varphi_L(x,\theta) = \varphi - \left\{30°\cos(\alpha)\left(\frac{1-\cos(\theta)}{2}\right)\left(1-\frac{x}{R_t}\right)^2\right\} . \tag{2-40}$$

Another effect of an oblique impact is that the ejection velocities on the downrange side will be higher. This effect is described by Richardson et al. (2007) by the following equation:

$$v_L(x,\theta) = \left((v\sin(\varphi))^2 + \left(\frac{v\sin(\varphi)}{\tan(\varphi_L)}\right)^2\right)^{\frac{1}{2}}. \tag{2-41}$$

Asymmetric ejection angles for oblique impacts are illustrated in Fig. 2-6 for a 50-km test crater at the equator of Ceres. The projectile incoming direction is north. The impact velocity is 4.79 km/s (O'Brien and Sykes, 2011) and the projectile consists of dense rock (Collins et al., 2005). Additional parameters for Ceres are listed in Table 4-1. Ejection angles for a 10° and a 45°

impact (to the horizontal) are much higher at the side of the impacting projectile (uprange). For the 45°-impact, the uprange (side of the impact) and downrange (opposite side of the impact) side are specifically asymmetric. Ejection angles for a vertical impact are radial symmetric. The effect on ejection velocities is less significant as illustrated in Fig. 2-7. Asymmetric ejection velocities occur at the projectile radius at the inner edge of the ring for the 10°-impact and less significant for the 45°-impact. A fraction of the ejected particles is ejected at very high velocities up to 22 km/s. Most of the particles have velocities below that value.

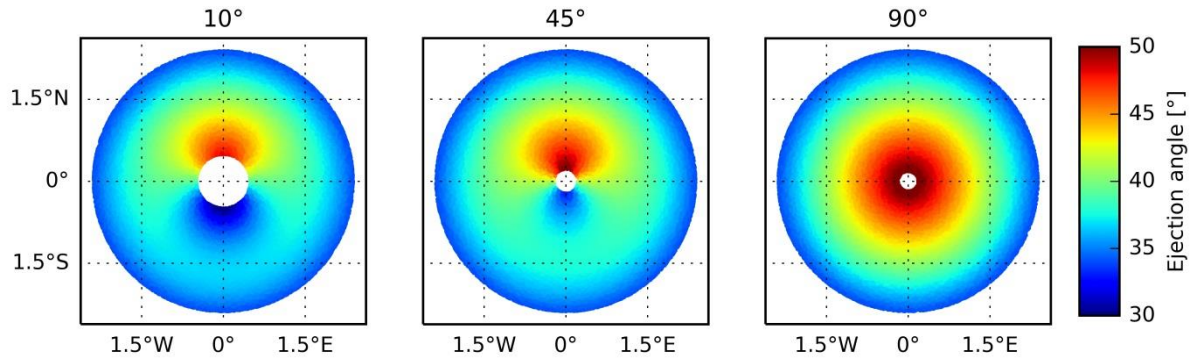

Fig. 2-6. The effect of the impact angle on ejection angles. Simulated ejection angles for a 50-km crater with impact angles of 10°, 45° and 90° to the horizontal. The projectile impacts from the north (top) for the oblique cases.

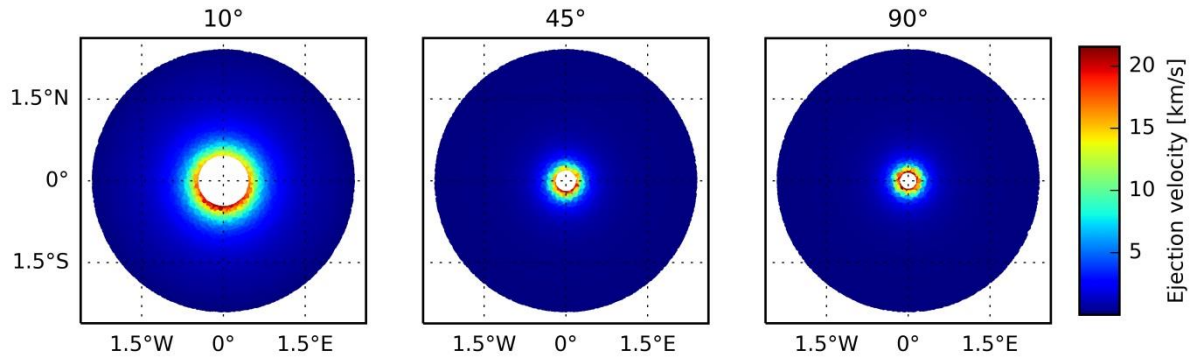

Fig. 2-7. The effect of the impact angle on ejection velocities. Ejection velocities for a 50-km test crater with impact angles of 10°, 45° and 90° to the horizontal. The projectile impacts from the north (top) for the oblique cases.

2.2.8 Particle Diameter

After the calculation of re-impact sites and the modelling of trajectories, the actual size distribution of the ejected particles is analyzed in order to evaluate the effect on the local morphology.

Using relations developed by Melosh (1984) and Grady and Kipp (1980), Artemieva and Ivanov (2004) relate the largest fragment size l_a to the ejection velocity v by:

$$l_a = \frac{T_f D_p}{\sigma v^{\frac{2}{3}} v_p^{\frac{4}{3}}} \tag{2-42}$$

,where T_f is the tension at fracture/tensile strength, D_p the projectile diameter, σ the target density and v_p the velocity of the projectile. The dynamic tensile strength is defined as the "the stress above which microscopically observable cracks appear" (Ai and Ahrens, 2004) and it depends on the target material and its physical properties.

2.3 Power-Law Distributions

Power-law distributions are a tool to mathematically describe size-frequency distributions of ejecta blocks.

The theory for power-law distributions of empirical data is discussed in Clauset et al. (2009) and Newman (2005). The data series x with the exponent or scaling factor α obeys the power law if it follows the probability function in Eq. 2-43.

$$p(x) \propto x^{-\alpha} \tag{2-43}$$

The complementary power law distribution function is given by Eq. 2-44 . The minimum value at which power-law behavior holds is defined as x_{min}.

$$p(x) = Cx^{-\alpha} \tag{2-44}$$

The constant C is provided by the normalization requirement in Eq. 2-45.

$$1 = \int_{x_{min}}^{\infty} p(x)dx = C\int_{x_{min}}^{\infty} x^{-\alpha}dx = \frac{C}{1-\alpha}\left[x^{1-\alpha}\right]_{x_{min}}^{\infty} \tag{2-45}$$

With $\alpha > 1$, we get for the constant C:

$$C = (\alpha-1)x_{min}^{\alpha-1} . \tag{2-46}$$

Then we get for the complementary power law distribution function:

$$p(x) = (\alpha-1)\, x_{min}^{\alpha-1}\, x^{-\alpha} = \frac{(\alpha-1)}{x_{min}} \left(\frac{x}{x_{min}}\right)^{-\alpha}. \quad (2\text{-}47)$$

The calculation of the cumulative distribution function allows to plot the probability P(x) that x has a value of x or greater (Eq. 2-48).

$$P(x) = \int_{x}^{\infty} p(x')dx' = \left(\frac{x}{x_{min}}\right)^{-\alpha+1} \quad (2\text{-}48)$$

3 GEOLOGIC MAPPING OF THE AC-11 SINTANA QUADRANGLE : ASSESSING DIVERSE CRATER MORPHOLOGIES

This chapter has been published as the following peer-reviewed article:

F. Schulzeck, K. Krohn, I.v.d. Gathen, N. Schmedemann, K. Stephan, R. Jaumann, D.A. Williams, D.L. Buczkowski, S.C. Mest, J.E.C. Scully, E. Kersten, K.-D. Matz, A. Nass, F. Preusker, T. Roatsch, C.A. Raymond, C.T. Russell, 2018. Geologic mapping of the Ac-11 Sintana quadrangle: Assessing diverse crater morphologies. Icarus. 316, 154-166.

The article may be found using this link: https://doi.org/10.1016/j.icarus.2017.12.007

A detailed description of the contribution of the thesis author can be found in section 1.3.

ABSTRACT

A geologic map at a scale of 1:1,000,000 of the Ac-11 Sintana quadrangle (21-66°S and 0-90°E) from the dwarf planet Ceres and based on data from NASA's Dawn spacecraft, was produced as part of a geologic mapping campaign in order to investigate the surface structure, stratigraphy, composition and surface modifying processes. The Sintana quadrangle is geologically dominated by cratered terrain with morphologically distinct crater types. The most prominent craters, Sintana, Hamori, Jarimba, Tupo, Annona and Darzamat, have complex structures including smooth crater material covering their floors, collapsed crater walls forming terraces, and central ridges. Multiple gravity-driven blocky mass wasting features indicate post-impact crater modification and are indicative of an ice-rich subsurface, in which there is no topographic or structural evidence of endogenic activity visible in the quadrangle. Absolute age estimates suggest that the entire surface in the quadrangle was resurfaced ~1.1 Ga ago, possibly by Kerwan-related impact-induced melting.

3.1 INTRODUCTION AND GEOLOGIC SETTING

Launched in September 2007, NASA's Dawn spacecraft arrived at the dwarf planet Ceres on March 6, 2015, with the goal to investigate the largest massive body in the asteroid belt in order to understand its origin, evolution, composition and the variety of geologic processes that were active in the early Solar System (McCord and Sotin, 2005; Russell and Raymond, 2011). A combined approach of gravitational studies (Konopliv et al., 2011), visible and near-infrared spectroscopic measurements (De Sanctis et al., 2011), gamma-ray and neutron spectroscopy (Prettyman et al., 2011) and photogeologic and topographic analysis with Dawn's Framing Camera (Sierks et al., 2011) was used to study Ceres. Both new data and models are used to refine our knowledge about Ceres' interior and shape. Recent Dawn-based gravity models describe

Ceres as a partially differentiated body with a rocky core (Ermakov et al., 2017; Park et al., 2016). Pre-Dawn models suggested a pure water-ice shell for Ceres and hence predicted a sparsely cratered surface due to viscous relaxation (Bland, 2013; Castillo-Rogez and McCord, 2010; McCord and Sotin, 2005), instead Dawn observed a heavily cratered surface (Buczkowski et al., 2016; Hiesinger et al., 2016). Pristine crater morphologies and Dawn-derived shape and gravity models indicate a strong crust and suggest a rock-ice mixture with less than 40% ice instead of a pure water-ice shell (Bland et al., 2016; Fu et al., 2017; Hiesinger et al., 2016; Park et al., 2016). Viscous relaxation is found to be only relevant for scales of several hundreds of kilometers, such as for the partially relaxed Kerwan crater (284 km) (Fu et al., 2017; Hiesinger et al., 2016; Williams et al., 2018b, this issue). Ceres' global geology is dominated by impact craters as the most ubiquitous surface features (Hiesinger et al., 2016), with a variety of shapes and structures, such as polygonal craters, floor-fractures, terraces, central peaks, smooth crater floors, flow-like features, mounds and central pits (Buczkowski et al., 2016). Morphologies of craters with diameters up to 30-40 km are remarkably similar to those on icy satellites in the outer Solar System (Hiesinger et al., 2016; Schenk et al., 2016). Hiesinger et al. (2016) found that the transition from fresh simple-bowl shaped craters to modified complex craters occurs at 7.5-12 km. On Ceres, craters larger than 300 km are absent (Hiesinger et al., 2016), suggestive of a geologically young surface. The Dawn Science Team established a geologic mapping campaign for Ceres, similar to that undertaken for the asteroid Vesta (Williams et al., 2014; Yingst et al., 2014), in order to assess the geological history of Ceres. A series of 15 quadrangle geologic maps (Fig. 3-1) provides geologic context information for the analysis of surface features observed in Framing Camera images as the baseline for further investigations and models. The Ac-11 Sintana quadrangle, which is named after one of its prominent impact craters Sintana, is located in Ceres' southern hemisphere between 21-66°S and 0-90°E. In addition to providing an overview of the main geologic units in the area of the Sintana quadrangle, major goals of this work are (1) the investigation of the diversity of crater morphologies and the progression from a recently emplaced to a geologically old degraded impact feature. (2) The southern hemisphere of Ceres is less heavily cratered than its northern hemisphere, because of resurfacing caused by large impacts such as Kerwan, Urvara and Yalode (Hiesinger et al., 2016; Marchi et al., 2016). Therefore, we use a combination of geologic mapping and crater size frequency distribution (CSFD) measurements to look for evidence of resurfacing either by impact ejecta emplacement or internal activities.

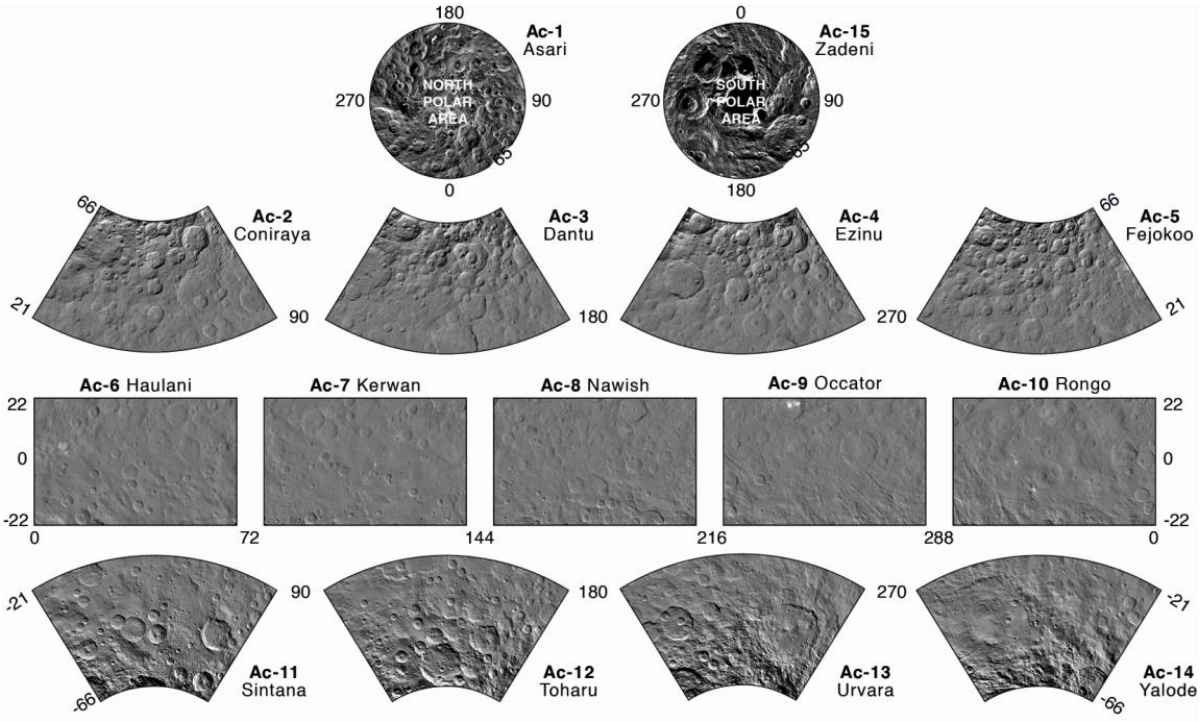

Fig. 3-1. Cartographic scheme of 15 quadrangles used for HAMO- and LAMO-based regional geologic mapping (Roatsch et al., 2016a)

3.2 Data and Methodology

We used Dawn Framing Camera (FC) data sets of different spatial resolutions to obtain a comprehensive understanding of the study area. For a more detailed description of the Dawn mapping approach, we refer readers to the introductory paper of this issue by Williams et al. (2018a, this issue). Clear filter mosaics based on Dawn Framing Camera images (Sierks et al., 2011) are the primary base for mapping. The Dawn Framing Camera (FC) data sets that have been acquired during different phases of the Dawn mission are: Survey Orbit (415 m/pixel), High Altitude Mapping Orbit (HAMO, 140 m/pixel) and Low Altitude Mapping Orbit (LAMO, 35 m/pixel) (Roatsch et al., 2016a). The final geologic map used an uncontrolled LAMO clear filter mosaic (Fig. 3-2). Information about the albedo is based on photometrically corrected clear filter images. Furthermore, HAMO FC clear filter images have been used to produce a stereophotogrammetry-based digital terrain model (DTM) (Fig. 3-3) (Preusker et al., 2016), which enables the assessment of the topography in the quadrangle. It also allows for the determination of slopes and profiles that are used for relative steepness analyses. In addition, images acquired in the seven color filters of the FC camera provide spectral information and support the investigation of relationships between stratigraphy and composition. We use the ratio of the filters F8 (438 nm) and F3 (749 nm), which have been identified as a useful additional tool in roughly estimating relative surface ages by weathering related spectral alteration of surface

materials (Schmedemann et al., 2016; Stephan et al., 2017a). Ratio values are directly correlated to the visible spectral slope, which particularly can indicate differences in the chemical, but mostly in the physical surface properties (Stephan et al., 2017b). Ratio values <1 indicate a positive ('red') spectral slope and ratio values >1 point to a negative (blue) spectral slope (Stephan et al., 2017a). The values of the two photometrically corrected color filters are divided on a pixel-by-pixel basis. We applied a median filter of 8 by 8 pixels onto the resulting ratio image, which reduces the image resolution by a factor 8, but considerably improves the signal-to-noise ratio (SNR) and provides a high-quality ratio image sufficient for our analysis. The resulting color-coded ratio map (Fig. 3-4) shows variations in the resulting ratio values between 0.9 and 1.05 throughout the Sintana region, implying changes from a reddish to a bluish visible spectral slope between 438 and 749 nm.

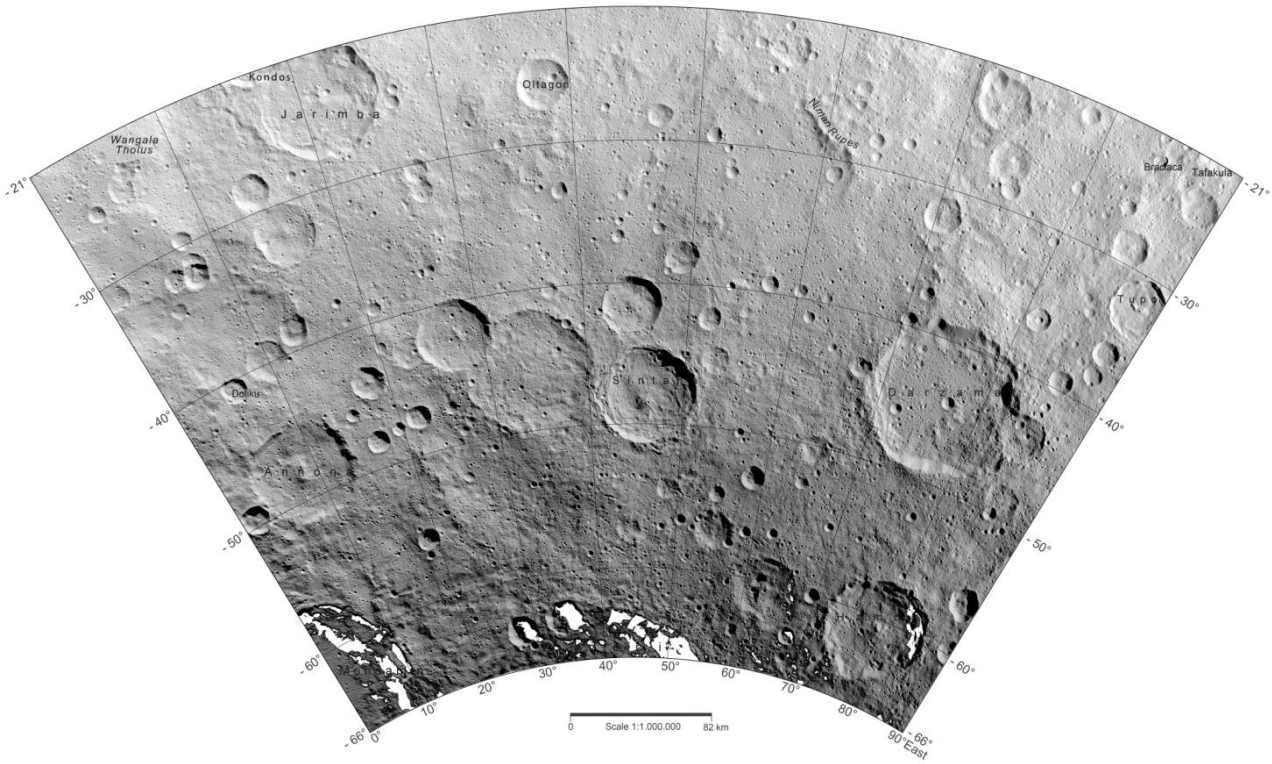

Fig. 3-2. Dawn FC clear filter mosaic of the Ac-11 Sintana quadrangle

The geologic mapping was performed within the Esri's ArcGIS Suite (release 10.3). An ArcGIS mapping template (Naß et al., 2015) that provides the standardized cartographic symbols for planetary mapping (Naß et al., 2011) based on the FDGC Digital Cartographic Standard for Geologic Map Symbolization (USGS, 2006) was used by the mapping team. The final map scale is 1:1,000,000, while the detailed geologic mapping was conducted at a higher scale of 1:100,000. Individual features such as the diameter of craters or the length of linear structures and polygonal sides were mapped down to a size of 5 km. The mapping accuracy of the boundaries of single

structures ranges from several tens of meters to a few hundred meters, dependent on the sharpness of individual contacts.

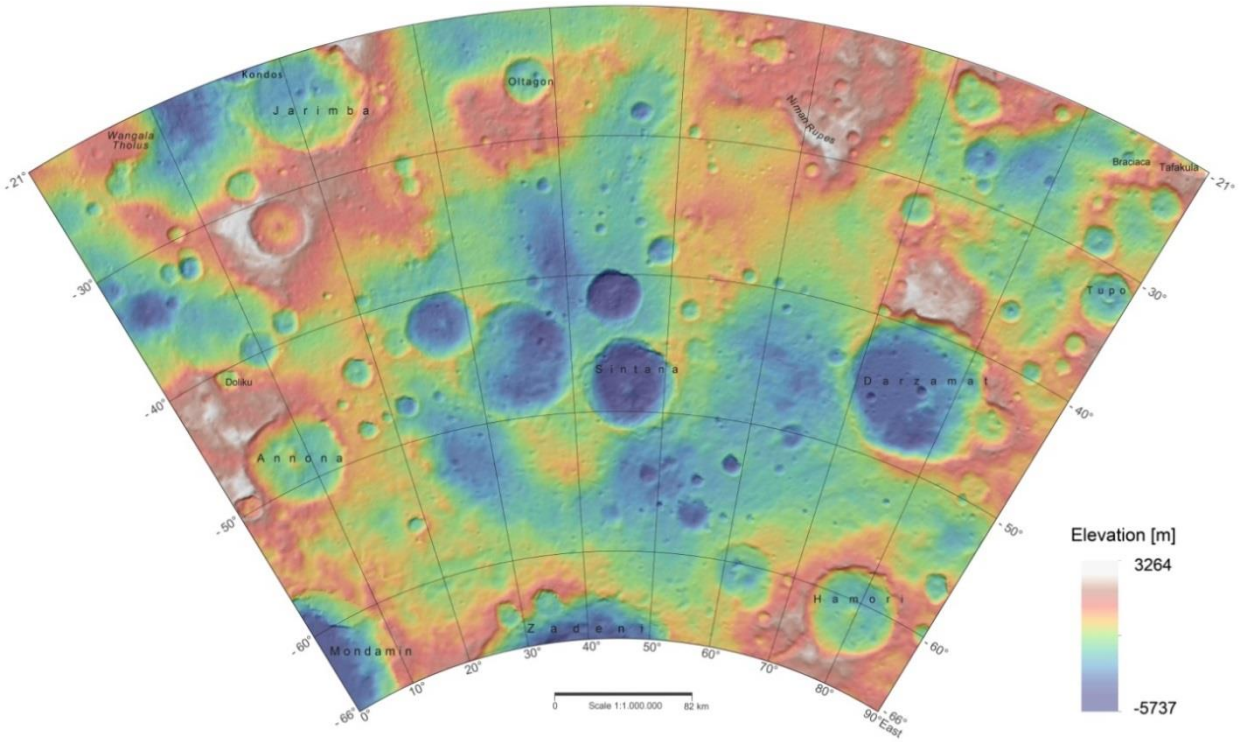

Fig. 3-3. HAMO-based digital terrain model (50% transparency) derived from Dawn Framing Camera images on top of a hillshade. The variation in topography is about 9 km.

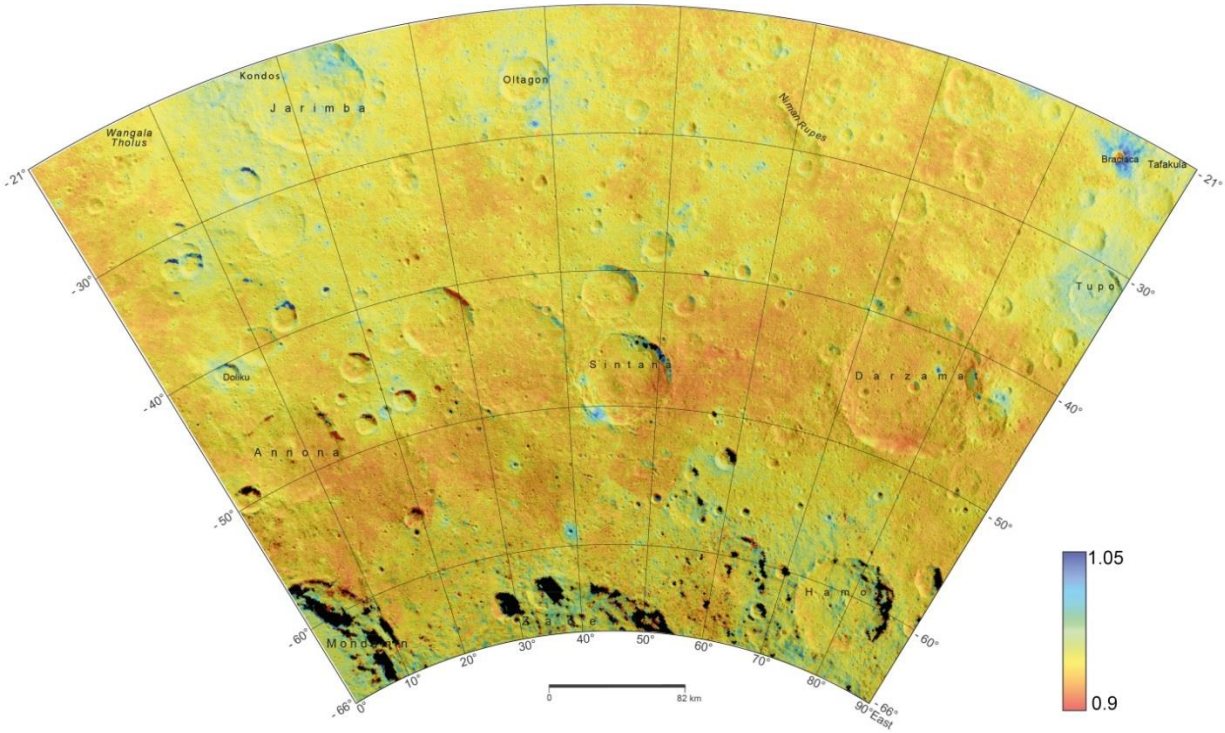

Fig. 3-4. Color ratio F8 (438 nm) / F3 (749 nm) displayed with a transparency of 40% on a hillshade

Crater size frequency distributions (CSFD) were used to support relative age estimation of geologic units. The CSFD is measured with the standardized approach described in Kneissl et al. (2011) using the CraterTools extension for Esri's ArcMap. This program minimizes distortion effects on account of different map projections. Crater modeling ages are then determined using the CraterStats software (Michael and Neukum, 2010; Michael, 2013) by fitting the observed CSFD to the production function. The production function (PF) can then be used to derive crater model ages from the chronology function (CF). Two types of production function and chronological model ages are used for Ceres: the lunar-derived model (LDM), which adapts lunar CF and PF to Cerean impact conditions as well as the asteroid-derived model (ADM) (Hiesinger et al., 2016). For our study, results from both chronology systems are reported. For the cratered terrain, only craters larger than 5 km were included to avoid secondary craters whose diameters usually are below 5 km. The maximum size of secondary craters is usually 5% of the size of their primary crater (e.g. Shoemaker, 1965). Using craters larger than 5 km will avoid most secondaries, but still allows the inclusion of as many craters as possible. In addition, randomness analyses (Michael et al., 2012) were applied to test for clustering with secondary craters. We used the M2CND (Mean 2^{nd}-closest neighbor distance) as the measure for spatial configuration. It descibes the distribution of the real data and randomly distributed configurations generated by a Monte Carlo simulation via various iterations. The result is a histogram describing the relative likelihoods of derived values.

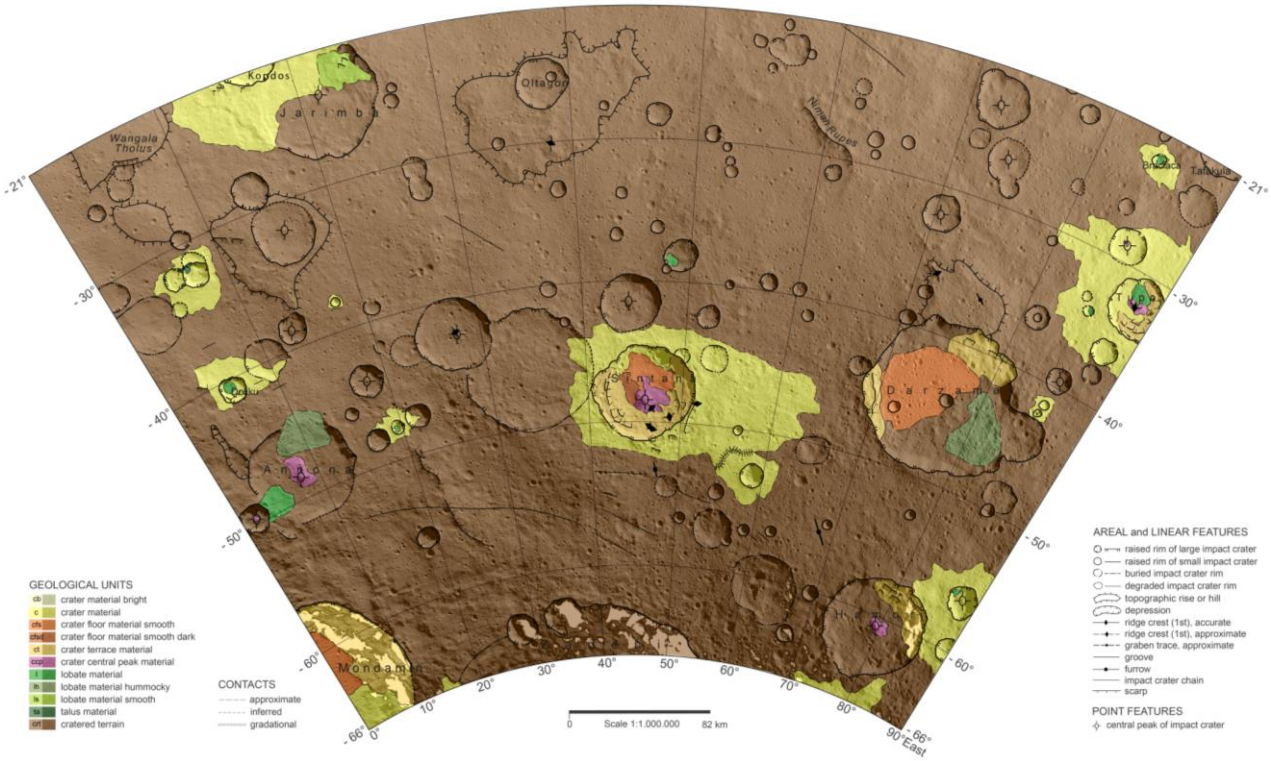

Fig. 3-5. Geologic map of the Ac-11 Sintana quadrangle on top of a clear filter LAMO mosaic. Units are displayed with a transparency of 50%. For a larger version of the map, we refer to the supplementary material.

3.3 RESULTS

3.3.1 TOPOGRAPHY AND STRUCTURAL FEATURES

The DTM of the Ac-11 Sintana quadrangle shows an undulating surface with topographic variations ranging over ~9 km, with a minimum at -5.7 km and a maximum at 3.2 km. An extended depression, with its center near the impact crater Sintana, characterizes major portions of the cratered terrain. This depression is part of an impact basin planitia C (~500 km in diameter) postulated by Marchi et al. (2016) based on the investigation of long wavelength topography. The quadrangle region is also characterized by several local regions of high topography (Fig. 3-3) that are mapped as topographic rises. The positive topographic feature at 6.64°E, 21.62°S is characterized by a domical hill and is best described as a tholus (Wangala Tholus). The tholus has an irregular basal shape that extends to its south and exhibits moderately sloping flanks. There are also prominent topographic rises that occur next to and around impact craters. Examples can be observed north of the rim of the Darzamat crater, around the Oltagon crater (28 km, 37.96°E, 25.95°S) and around the 46-km large crater south of the Jarimba crater. Besides their variation in topography, they show no specific textures or colors (i.e., compositions). Widespread crater chains also occur in the southern region of the Ac-11 Sintana quadrangle. Most of them are oriented SE-NW, while shorter chains with overall smaller craters occur all over the quadrangle with varying sense of direction. Some of the larger chain craters reveal crater rims that distinguish them from pit craters (Wyrick, 2004). Therefore, the crater chains are interpreted as secondary crater chains. There are two large scarps: Niman Rupes, and a less prominent scarp to the east of Annona crater. Those scarps are probably related to topography produced by ancient impacts. In addition, Tupo crater exhibits concentric fractures in its interior.

3.3.2 MAP UNITS

In the following sections we provide a description and interpretation of map units, which are displayed on the geologic map, as shown in Fig. 3-5.

3.3.3 CRATERED TERRAIN (CRT)

Description: Cratered terrain is the dominant geologic unit of the quadrangle and exhibits the highest crater density with a variety of different crater preservation and degradation stages. All other units superimpose this one. The morphologies of ejecta blankets are highly subdued and erased by subsequent impacts and impact gardening.

Interpretation: Because of its crater density and the superimposition by younger units, the cratered terrain unit is interpreted to be the oldest unit of the quadrangle representing Ceres' ancient crust that is heavily degraded by ancient and recent impact events.

3.3.4 CRATER MATERIALS (C, CB)

Description: The unit of cratered terrain is superimposed by different types of crater material that are deposited in and around craters with more distinctive fresh morphological features (e.g., sharper rims, preserved terraces, etc.). Continuous crater material units have been mapped, for instance, around Tupo crater and Kondos crater (44 km). Kondos' crater material covers large parts of the adjacent Jarimba crater (21.25°E, 24.08°S), which has a diameter of 69 km. High albedo crater material is mapped as bright crater material. The bright crater material (cb) appears mostly around extremely small craters. One example is the larger deposit surrounding the 8 km Braciaca crater at 84.4°E, 22.8°S. Crater material sometimes correlates with a higher F8/F3 ratio values (Fig. 3-4).

Interpretation: Crater material is interpreted as continuous ejecta blankets of relatively young impact craters. Morphologically it is mostly visible for fresh craters. One exception is the degraded Sintana crater. Bright crater materials are associated with ejecta blankets of very fresh impacts, which is supported by the high F8/F3 ratio values that characterize most of Ceres' young impact craters (Stephan et al., 2017b).

3.3.5 LOBATE MATERIALS (L, LH, LS)

Description: Lobate material occurs as a positive relief feature and is deposited on a topographic gradient. Its deposition is always linked to a crater. It occurs in the craters Annona, Tupo, Darzamat, Jarimba and also in a few smaller ones (Fig. 3-5). The unit is classified into undivided (l), smooth (ls), and hummocky lobate material (lh). The classification mainly results from the degree of overprinting by craters. Smooth units have few overprinting craters. Hummocky units, on the other hand, exhibit many small craters on top. Undivided lobate material lies in between these two cases. Annona, for instance, shows a unit of undivided material (Fig. 3-6a). This unit trends downslope, starting from a fresh crater on Annona's southeast crater rim, with maximum length of approx. 17 km and a maximum width of approx. 15 km. Two frontal lobes characterize its downslope front. Units of undivided lobate material (l) occur in different shapes ranging from lobate-shaped (Fig. 3-6b) to blocky in appearance (Fig. 3-6c). An example of a smooth lobate material unit occurs adjacent to the small impact crater (~15 km) on the northeast crater wall of Jarimba crater (69 km, 21.25°E, 24.08°S) (Fig. 3-6d), which has a particularly smooth surface

texture. Annona also exhibits an example of hummocky lobate material with a rugged and chaotic surface structure (Fig. 3-6e), similar to a unit inside the 92 km Darzamat crater (76.4°E, 44.21°S).

Interpretation: The lobate material unit is interpreted to have been emplaced by mass wasting processes.

3.3.6 SMOOTH CRATER FLOOR MATERIAL (CFS, CFSD)

Description: Smooth crater floor material (Fig. 3-7a and b) occurs inside craters and is characterized by a low variation in topography. It is present in the craters Sintana (58 km), Mondamin (126 km) and Darzamat (92 km). Smooth crater floor material (cfs) always occurs on the lowermost floors of the craters. The interior of the Sintana (Fig. 3-7a and b) crater additionally contains a unit of dark smooth material (cfsd).

Interpretation: Smooth crater floor material is interpreted as impact melt (Schenk et al., 2016). Deposits of darker smooth crater floor material are interpreted as dark impact melt with a possibly different composition.

3.3.7 CRATER TERRACE MATERIAL (CT)

Description: Terrace material was mapped inside large complex craters, like Sintana (Fig. 3-7a, and b) and Hamori (60 km). In most cases, only parts of the crater walls are terraced. There are always multiple terraces with varying widths concentric to the crater rim. Terrace material can have a smooth or hummocky texture. A type location for terrace material with a smooth surface structure is the southern interior of Sintana crater (Fig. 3-7a). A type location for terraced material with a more hummocky surface structure is, for instance, the western crater wall of Tupo crater (Fig. 3-6e).

Interpretation: Terrace material is a unit of mass wasting material, formed during the modification stage of the impact when the transient cavity collapses. Some parts of the terraces might have already been degraded.

3.3.8 TALUS MATERIAL (TA)

Description: Talus material is restricted to crater walls and is designated as fine material whose lineations suggest a downslope direction of movement. In the majority of cases, areas of talus material are too small to be mapped. One area of larger extent is located at a western slope of a young crater at 7.5°E, 32.3°S with a diameter of 16 km (Fig. 3-6f).

Interpretation: Talus material is interpreted to be debris of displaced material transported downslope due to slope instability. The texture of the mapped talus material suggests that it is composed of loosely consolidated materials.

3.3.9 CENTRAL PEAK MATERIAL (CCP)

Description: The central peak material unit is used for topographically elevated areas in the approximate center of an impact crater. Sintana (Fig. 3-7a and b), Hamori, Annona have large central peaks and Tupo (Fig. 3-7e and f) has a central ridge. Central peak material is usually characterized by steep flanks, with slopes up to 25°. In the quadrangle area, central peaks are observed for craters larger than 15 km. In contrast, they are missing in several large craters, such as Darzamat and the crater west of Sintana.

Interpretation: Central peaks form during the crater's modification stage due to uplift (e.g. Melosh and Ivanov, 1999).

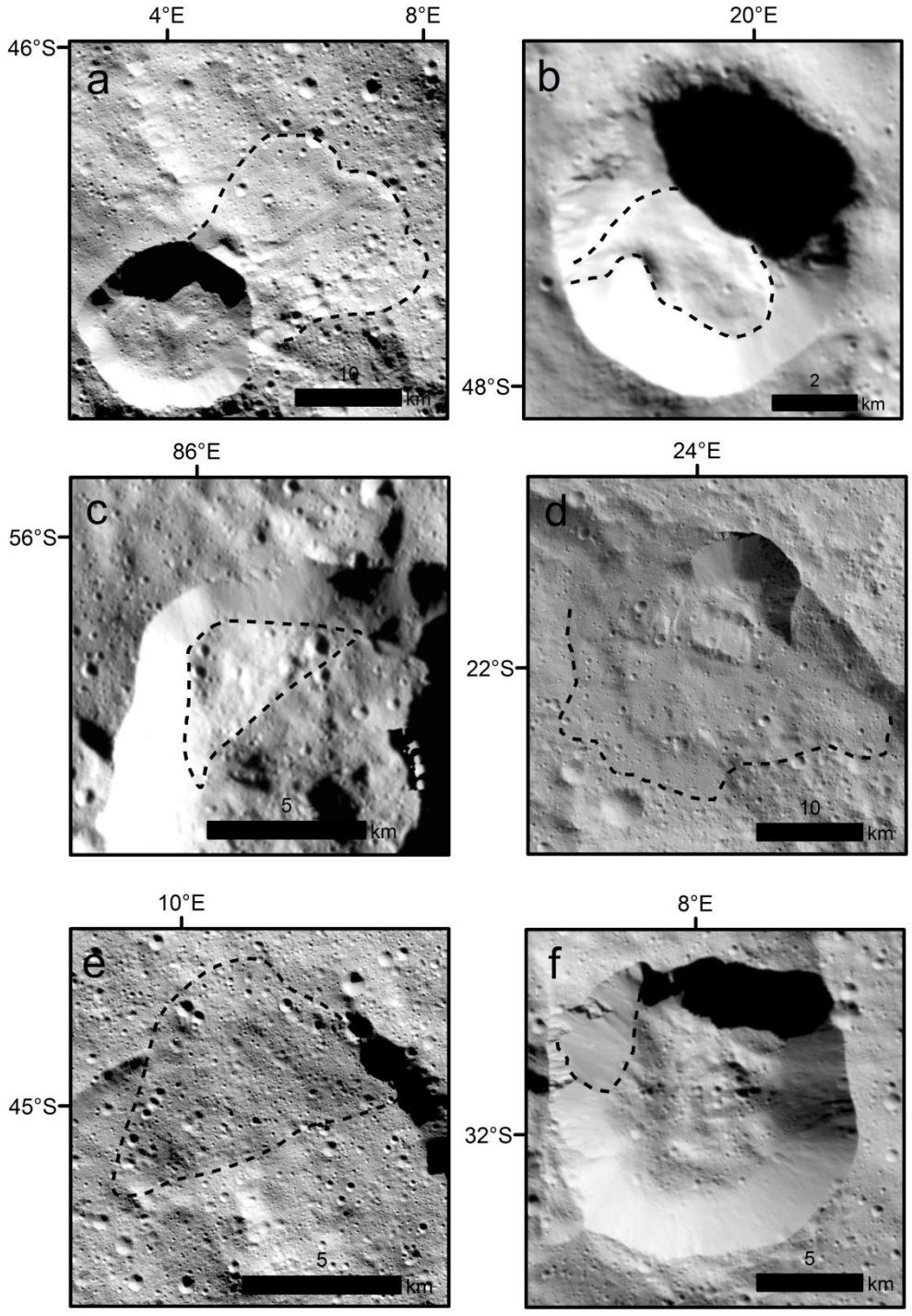

Fig. 3-6. Mass wasting features mapped as lobate (l, ls, lh) or talus material (ta) on clear filter mosaic images in LAMO resolution. (a) A lobate-shaped landslide in Annona mapped as undivided lobate material (l). The crater an Annona's crater rim from which the landslide emerges has a diameter of ~ 19 km. (b) A lobate shaped landslide in an unnamed crater mapped as undivided lobate material (l). (c) A blocky mass wasting feature mapped as undivided lobate material (l) in an unnamed crater(~18 km). (d) A landslide in Jarimba crater mapped as smooth lobate material (ls). (e) A mass wasting block in Annona mapped as humocky lobate material (lh) (f) and talus material (ta) inside an unnamed crater at 7.5°E, 32.3°S with a diameter of 16 km.

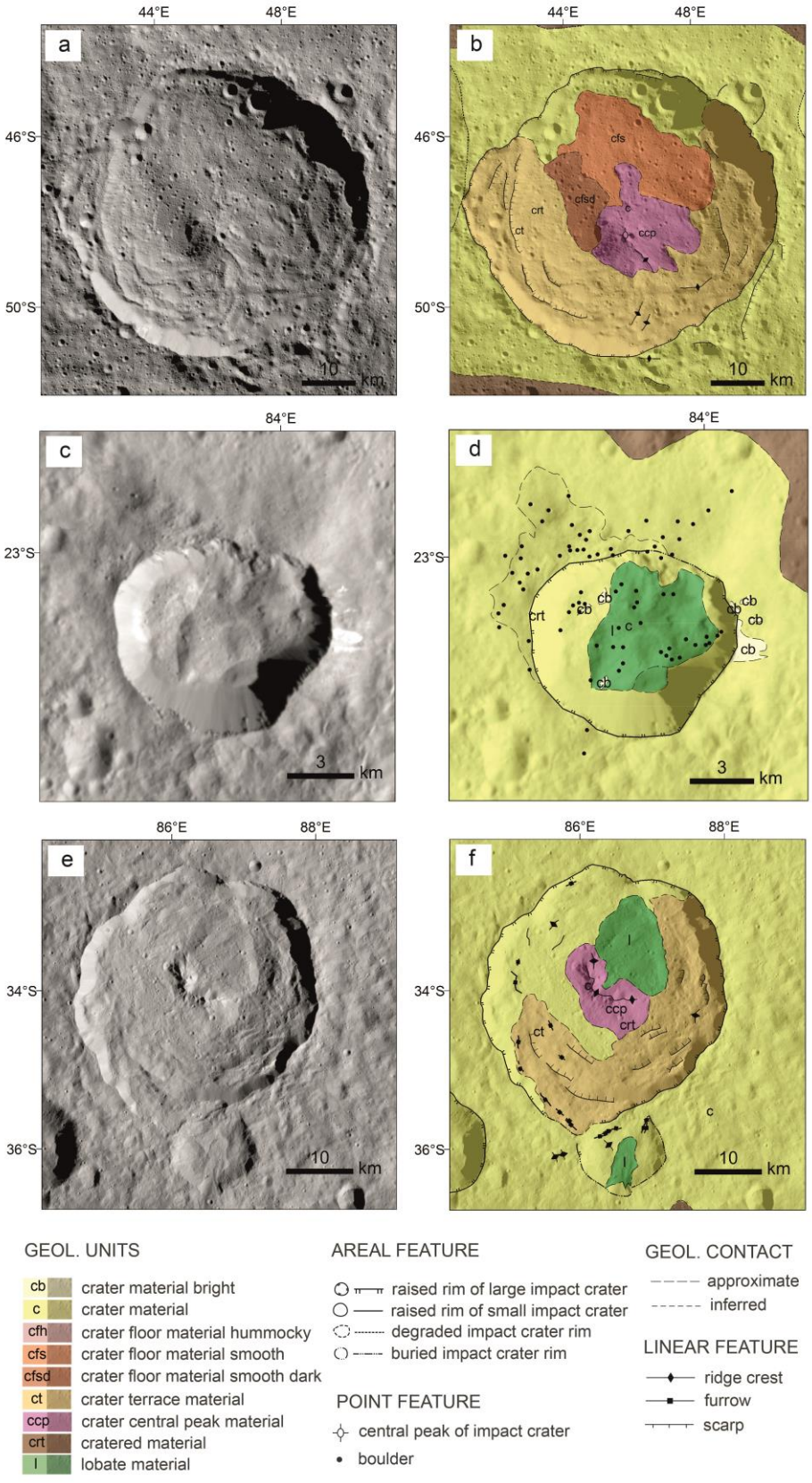

Fig. 3-7. Highlighted craters of the Sintana quadrangle with multiple inner crater structures. The craters are mapped in greater detail than the global map (Fig. 3-5). (a) LAMO clear filter image of Sintana crater. (b) Detailed map of Sintana crater. Several inner crater units were identified. (c) A LAMO-based clear filter image of Braciaca crater with rim deviated accumulated lobate material in the interior. (d) A

detailed map of Braciaca crater's units and features. (e) LAMO clear filter image of Tupo crater. (f) Detailed map of Tupo crater including small-scale tectonic structures and peak deviated accumulated lobate material.

3.4 HIGHLIGHTED CRATERS

The Sintana quadrangle shows several complex craters, with different inner structures and features. Some particularly unique examples are discussed in the following sections.

3.4.1 SINTANA CRATER

The 58-km crater Sintana (46.2°E, 48.07°S) is one of the largest craters in the quadrangle, and its collapsed interior formation and central peak are unique in this area. Sintana is located between two other large craters. Sintana is the morphologically youngest of the three craters with a large central peak (Fig. 3-7a). Flow fronts mark the termination of the crater material to the east (Fig. 3-2), which is interpreted to be the remnants of an ejecta blanket. The crater wall of the large degraded and thus older crater west of Sintana is buried, likely due to Sintana ejecta. Terraces have formed up to the actual rim of Sintana crater. The interior of the crater is characterized by multiple curved ridges and scarps (Fig. 3-7a and b). Concentric terraces stretch across the whole crater wall, except for the northern section. The southern crater floor is covered by curved ridges. The closer they are to the crater center, the more radial is their orientation with respect to the crater center.

3.4.2 BRACIACA CRATER

Braciaca crater (8 km in diameter) is located at 84.4°E, 22.8°S. It has one of the highest F8/F3 ratios in the quadrangle (Fig. 3-4). It is characterized by an irregular shape, a sharp crater rim, and steep crater walls (Fig. 3-7c and d). The interior of the Braciaca crater is filled with landslide deposits and appears spectrally red (Fig. 3-4). These landslides originated from several places at the northern and northwestern crater wall. Clear filter images reveal bright crater material to the east of the crater rim (Fig. 3-7c). Color ratios show an even more extensive ejecta layer with rays far beyond the morphologically visible part (Fig. 3-4). The visible ejecta to the north of the crater rim is much smoother than the parts to its south, which presumably is thinner, because small craters below the ejecta layer are still visible (Fig. 3-7c). Furthermore, there is a rough patch on the smooth ejecta deposit outside the northwest crater rim covered with many boulders (Fig. 3-8). Boulders also occur on the crater floor and on the lobate material inside the crater. Several dozen single boulders were identified with estimated diameters ranging from several tens to a few

hundred meters. Boulders on Ceres are found to be predominantly clustered around craters with a fresh appearance (Schröder et al., 2016).

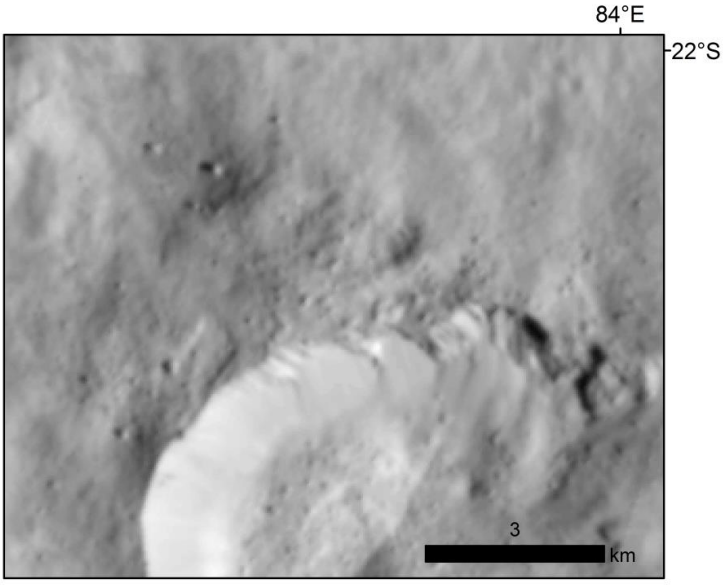

Fig. 3-8. A close-up showing the rich morphology of the northwestern part of Braciaca's ejecta blanket covered with boulders

3.4.3 TUPO CRATER

Tupo crater (88.4°E, 32.3°S) has a diameter of 36 km and its morphology shows characteristics of a young complex crater because of its well-defined crater rim and pristine ejecta layer, which is clearly visible in clear filter images as well as in color ratios (Fig. 3-4). Tupo's complex interior exhibits an extensive, curved central ridge. The material around the central ridge is slightly smoother and brighter than the surrounding terrain. In addition to its widespread ejecta layer, Tupo crater features furrows at the outer edge of the crater floor that are concentric to the crater rim (Fig. 3-7e and f) and part of the crater's terraces. Additionally, there are several scarps that form extensive terraces, indicative of crater wall collapse that took place after the impact. The southeastern part of the terraced terrain is more hummocky than the southwestern part. Below Tupo's northeastern rim, there is a landslide that consists of a large block (Fig. 3-7e). It is mapped as lobate material. The block moved as a whole from the crater rim downslope as far as the central peak. The extent of its top is approximately 14 km. It lenses out downslope in contrast to explicitly lobate shaped landslides, such as in the Annona crater. A crater, about 13 km in diameter adjoins Tupo's southern crater rim. The rim of the smaller crater is not as well defined as Tupo's, because it is overlain by the Tupo ejecta of Tupo crater, which makes it stratigraphically older.

3.5 GEOLOGIC EVOLUTION

Fig. 3-9 contains the correlation of map units within the Sintana quadrangle. The relative chronostratigraphy has been derived from the observed superposition relations of geologic/geomorphological units supported by absolute age modeling (Fig. 3-10 and Fig. 3-11).

The oldest unit is the cratered terrain, because it is superposed by all other units. Crater counting provides an age of 1.1 ± 0.1 Ga with the LDM and 1.0 ± 0.3 Ga with the ADM, respectively (Fig. 3-10a). While the LDM fits the data much better at all crater diameters, the ADM allows the fit of two diameter ranges, because of the straight shape of the chronology function. The fit of larger diameters (~30-90 km) is in good agreement with the LDM-derived age. Fitting only the smaller diameters (~8-25 km) would yield a much younger age of 490 ± 60 Ma. The results of the randomness analysis (Fig. 3-10) show that the data values lie mostly within one standard deviation of the Monte Carlo-derived mean, therefore a random distribution of the counted craters can be inferred. Most of the ages that are reported for cratered terrain elsewhere on Ceres are older, ranging from 1.8 Ga (Platz et al., 2018) and 2 Ga (Williams et al., 2018b) up to 3.1 Ga (Pasckert et al., 2018). However, the age of the cratered terrain in the Sintana quadrangle is close to the age of ~1.3 Ga (LDM) and 0.2 - 0.9 Ga (ADM), as reported for the Kerwan smooth material that is interpreted as impact-induced melting of volatile, ice-rich crust (Williams et al., 2018b, this issue). The Kerwan impact (124°E, 11°S) is located to the northeast of the Sintana quadrangle. Based on the derived ages, we suggest that the Kerwan smooth material might have resurfaced the cratered terrain in the Sintana quadrangle. Parts in the north of the Sintana quadrangle were previously mapped as Kerwan smooth material on a global map using HAMO data (Mest et al., 2017). To test whether the young age of only the cratered terrain is restricted to a part of the quadrangle, we divided our counting area in two regions: the smaller region is the area that was mapped as Kerwan smooth material on the global map, and the remaining quadrangle area (Fig. 3-10b and c). We derived absolute ages of 1.2 ± 0.2 Ga (LDM) and 410 ± 50 Ma (using crater diameters of ~6-25 km) to 1.2 ± 0.3 Ga (using crater diameters of ~25-90 km) (ADM) for the southern region (Fig. 3-10b) and 1.1 ± 0.2 Ga (LDM) and 400 ± 80 Ma (ADM) for the possible resurfaced northern region of the quadrangle (Fig. 3-10c). The ages for the two subareas are close to the ones derived for the whole quadrangle. Thus, morphologic and ages estimates suggest that possible resurfacing events in the Sintana quadrangle were not restricted to specific areas.

Younger than the cratered terrain are several large degraded craters, such as Darzamat, Hamori and Annona. Their interior features, such as central peaks (ccp), terraces (ct), hummocky lobate

material (lh) and smooh crater floors (cfs) are associated with the impact and crater modification. Consequently, those structures are nearly as old as their parent craters.

Sintana crater is the morphologically oldest crater that exhibits an ejecta blanket. The ejecta blanket is not as prominent as ejecta blankets of younger craters and is highly degraded. Most of the ejecta is mapped to the east of the crater. Another unit mapped only inside the Sintana crater is the dark smooth crater floor material (cfsd).

The morphologically youngest features in the Sintana quadrangle are the craters Kondos, Doliku, Tupo, Braciaca, and a few smaller unnamed craters. In contrast to the other craters, only the ejecta blanket of Tupo is sufficiently broad to allow for reliable crater counts. It overprints all other units and shows no signs of secondary cratering, which is confirmed by the randomness analysis. The model age using the LDM is 29 Ma ±2 and the ADM model age is 24 ± 2 Ma (Fig. 3-11). The LDM fits the data more exactly, especially in the larger diameter range. The randomness analysis gives values up to +/-3 standard deviations from the Monte Carlo-derived mean, which is still considered to be most likely random. The 8-km Braciaca crater is characterized by a fresh morphology, such as a distinct crater rim. Parts of its ejecta blankets are bright in clear filter images. It also has one of the highest F8/F3 ratios in the quadrangle, indicative of a young absolute age. Fig. 3-12 illustrates the correlation of the ejecta blankets of the fresh craters Tupo and Braciaca correlate with a high F8/F3 color ratio. By comparing color ratios F8/F3 and F8/F5 (365 nm) with absolute age measurements, Schmedemann et al. (2016) found that model ages increase with decreasing color ratio. The spectral analysis also shows that a smaller 2.7 band mostly correlates with morphologically young features (De Sanctis et al., 2017b). These correlations have been interpreted to be associated with changes in the physical properties of the unweathered surface material or as a result of the impact event (De Sanctis et al., 2017b; Stephan et al., 2017b). Those changes diminish with increasing surface age due to surface processes such as space weathering (Stephan et al., 2017b). Units that occur inside young craters are talus material (ta) and smooth and (undivided) lobate.

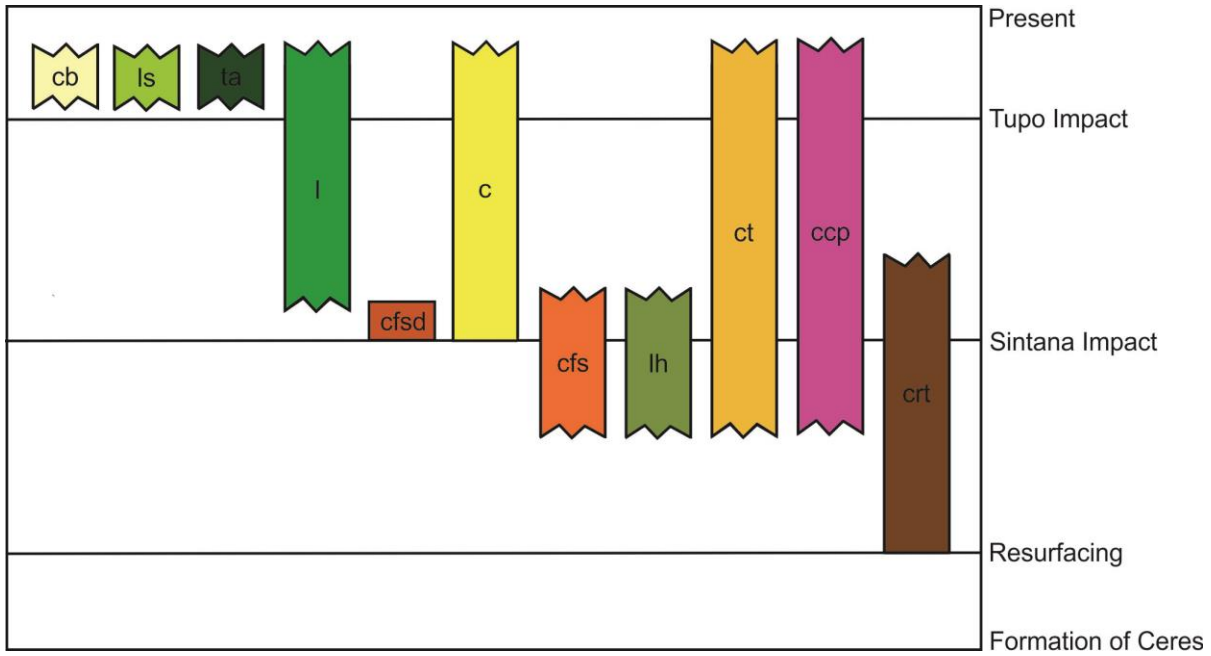

Fig. 3-9. Correlations of map units (COMU) for the Ac-11 Sintana quadrangle. Schematic axes classification.

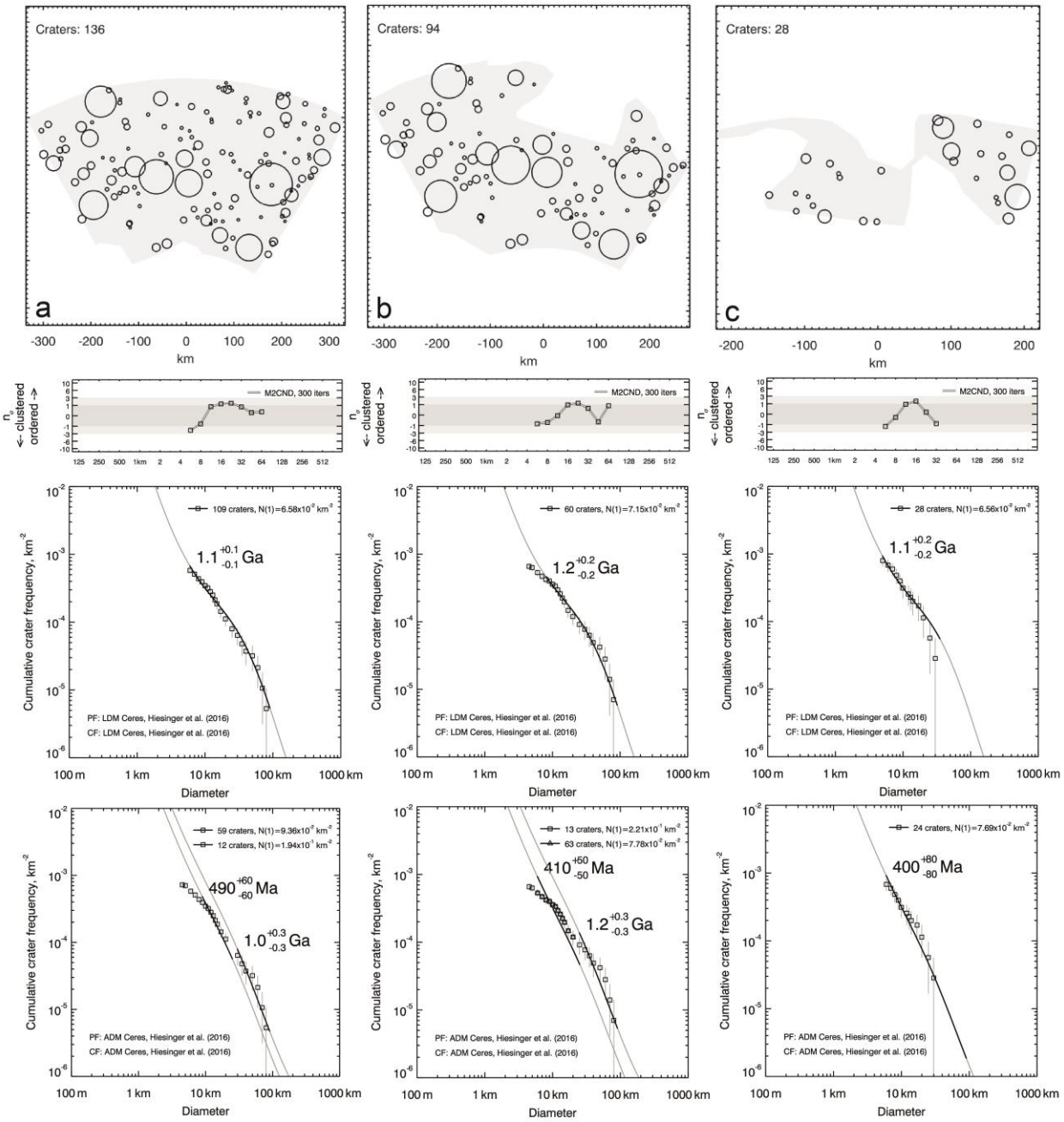

Fig. 3-10. Crater size-frequency distributions and best-fit model ages for the cratered terrain (crt). (a) Craters > 5 km with their center in the Sintana quadrangle were used to determine an absolute age for the quadrangle-wide area. The upper image shows the counting area with all counted craters. Below, the results of the randomness test and the best-fit model ages using the LDM and the ADM. (b) Absolute ages using craters > 5 km were estimated for the southern region of the quadrangle. The region that is supposingly overprinted by the Kerwan smooth material is left out. The upper image shows the counting area with all counted craters. Below, the results of the randomness test and the best-fit model ages using the LDM and the ADM. (c) Absolute ages were estimated for the region that possibly was resurfaced by the Kerwan smooth material. The upper image shows the counting area with all counted craters. Below, the results of the randomness test and the best-fit model ages using the LDM and the ADM.

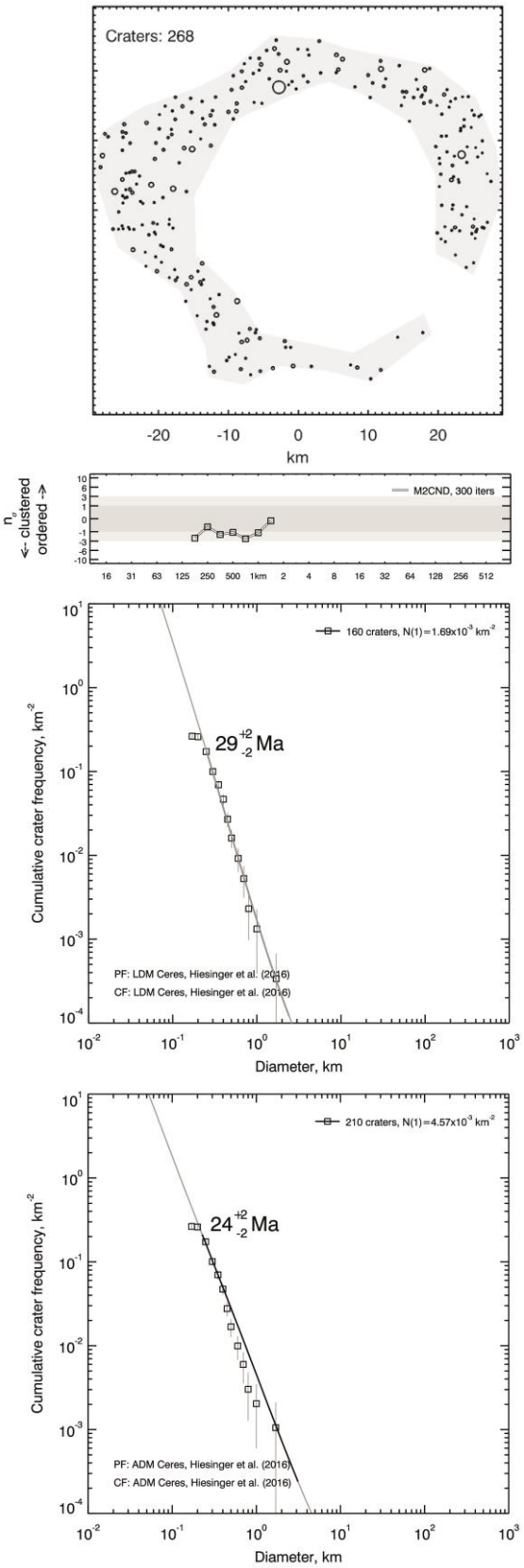

Fig. 3-11. Age determination for Tupo crater. The upper image shows the counting area with all counted craters. The results of the randomness test, the crater size-frequency distribution and the best-fit model ages (LDM and ADM) are displayed below. Only craters > 200 m were used for the fit.

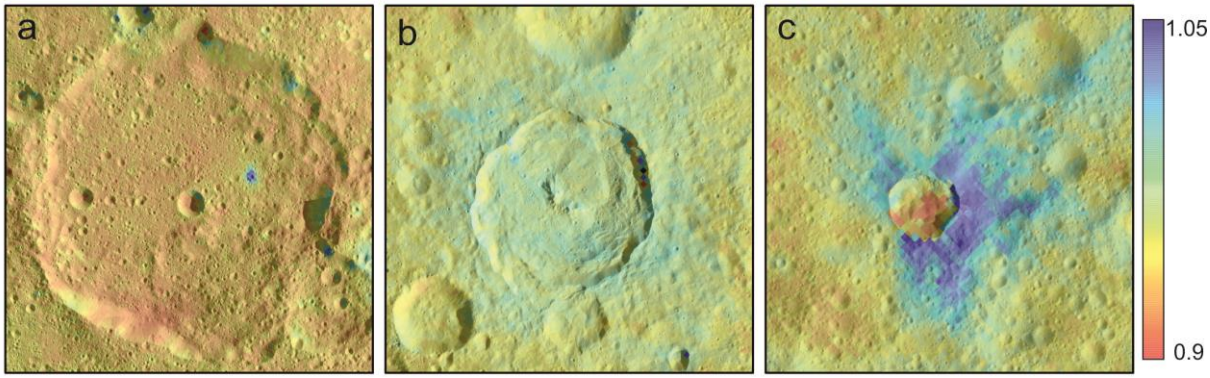

Fig. 3-12. Color ratio F8/F3 (60% transparency) on top of a clear filter mosaic for the craters Darzamat (a), Tupo (b) and Braciaca (c). The color ratio is increasing with decreasing age. The old degraded Darzamat crater has a lower F8/F3 color ratio than the younger Tupo and Braciaca craters. A very small impact inside Darzamat crater shows a high color ratio as well. In the Sintana quadrangle, Tupo is the largest crater with a high F8/F3 color ratio. In other regions of Ceres, there are also large craters, such as Haulani and Occator that are characterized by a higher ratio (Stephan et al., 2017b).

3.6 Discussion

The Ac-11 Sintana quadrangle of Ceres is mapped as part of the Dawn global geological analysis. Local features, such as craters, their morphology and deposits, and landslides were compared with similar ones on Ceres in order to understand how the Sintana quadrangle fits into the global geologic evolution. In addition, we estimate how tectonics and volcanic activity that have been identified in other regions on Ceres are relevant for the studied area in the southern hemisphere. For this purpose, gray-scale images, supported by topographic and color data of the Sintana quadrangle were used.

Absolute ages suggest that the Sintana quadrangle experienced a quadrangle-wide resurfacing by Kerwan impact melt, although distinct morphological deposits could not be identified. The north and south of the quadrangle show no difference in absolute age estimates. In contrast, spectral mapping of the Sintana and more eastern Toharu quadrangle reveals an increase in phyllosilicate and ammoniated phyllosilicate band intensity to the south of both quadrangles. This trend loosely coincides with topography, but is interpreted as the result of compositional heterogeneities in the Cerean crust (De Sanctis et al., 2017b). However, the age data indicate a possible significant influence of the Kerwan smooth material that might have affected at least the northern but more likely the whole quadrangle area. The less heavily cratered southern hemisphere of Ceres is associated with large impact events, such as Urvara and Yalode (Hiesinger et al., 2016), which could also have overprinted the Sintana quadrangle. However, the larger distances and reported absolute ages for the Yalode basin (580 ± 40 Ma, LDM) and Urvara basin (550 ± 50 Ma, LDM)

by Crown et al. (2018), which are younger than the material that fills and surrounds the Kerwan basin and the cratered terrain in the Sintana quadrangle, indicate that impact-induced melting from Kerwan impact is the quadrangle's most important resurfacing influence.

The features mapped in the Sintana quadrangle, such as crater shapes from highly degraded to fresh, landslides, secondary crater chains and concentric fractures, are typical for Ceres (Buczkowski et al., 2016). Craters in the Sintana quadrangle do not show pitted crater floors as observed for Haulani and Ikapati, which are interpreted to be an indicator for volatile-rich material deposited in such craters (Krohn et al., 2016; Sizemore et al., 2017).

Some large craters, such as the 80-km crater to the west of Sintana at 34.09°E, 45.62°S, do not have central peaks, while other craters of the same size in the quadrangle do contain central peaks. There could be several explanations for missing central peaks in large craters in the Sintana quadrangle. It has been postulated that viscous relaxation is limited to just some shallow craters indicating a spatially varying subsurface (Bland et al., 2016). Viscous relaxation is a wavelength-dependent change in topography. Long-wavelength topography is affected much more than short-wavelength topography (Hall et al., 1981). This effect would therefore lead to shallower craters, but with rims and central peaks that are still recognizable. Therefore, this model cannot fully explain the absence of central peaks in the quadrangle. Another effect could be the burial of the peak by mass-wasting material. A burial by lava that floods the crater floor, similar to what is observed for lunar craters (Pike, 1971), seems unlikely, even if cryovolcanism is considered for some features on Ceres (e.g. Krohn et al., 2016; Ruesch et al., 2016). The peaks might also have been destroyed by impact gardening, like what possibly occurred inside Darzamat crater, which has a small crater instead of a peak in its approximate center. Some large complex craters undergo modifications that lead to peak-ring craters. This transition is either explained by central peak collapse (e.g. Collins et al., 2002; Morgan et al., 2016) or by the nested melt-cavity model (Baker et al., 2011; Head, 2010). We find no peak-ring craters in our quadrangle, but those large craters without central peaks might have experienced a transition, even if it has not been completed.

Landslides in the Sintana quadrangle resemble features on other planetary bodies. Landslides that are most likely triggered by small impacts on crater rims are also observed on other small Solar System objects, such as Lutetia (e.g., Thomas et al., 2012). Numerical investigations by Elbeshausen et al. (2012) suggest that the localization and style of a landslide on asteroid (21) Lutetia, similar to the ones identified on Ceres, result from weakening due to acoustic fluidization caused by the impact process. Alternatively, blocky landslides were probably caused by a rotational slumping process. Some blocky landslides, such as the huge block inside Tupo (Fig.

3-7e), are similar to Toreva block landslides on Earth, which originate when a stronger unit collapses as a nearly intact block after the underlying weaker unit erodes (Melosh, 2011; Reiche, 1937). The landslide inside the Braciaca crater has a lower color ratio than the ejecta blanket of the crater. The mass wasting process probably transported older material into the crater, overlaying the young fall-back material deposits on the crater floor. This is similar to the 20-km Juling crater on Ceres at 168.4°E, 35.9°S (Stephan et al., 2017a).

Some landslides, mapped as undivided and smooth lobate material (Fig. 3-6a,b,d), correlate with identified flow features that are associated with ground ice (Schmidt et al., 2017). The three flow types described in Schmidt et al. (2017) have morphologies and aspect ratios that are more similar to ice-rich flows than to dry landslides. The undivided and smooth lobate material in the Sintana quadrangle are comparable to the type of flow described by Schmidt et al. (2017) as a long run-out landslide with circular to lobate toes.

The Sintana quadrangle lacks features that are related to volcanic activity. Hiesinger et al. (2016) identified several low crater density terrains on Ceres. Most of those areas are interpreted to have been formed by resurfacing. One of such areas in the Sintana quadrangle centered at 54.2°E/23.3°S, may have an endogenic origin as it displays features, such as dome-like structures and graben-like valleys and nested pits (Hiesinger et al., 2016). We, however, interpret possible dome-like structures as small variations in topography, probably related to impacts in this area. The resolution limits the distinction between pits and (secondary) craters. Tholi on Mars are of volcanic origin and show structures, such as channels, troughs and caldera pits (e.g. Plescia, 2004; Werner, 2009). In the Sintana quadrangle, tholi only differ topographically from surrounding terrain without morphological or compositional evidence for volcanic activity (Platz et al., 2015) or uplifting by diapirism or shallow intrusions (Fagents, 2003; Ruesch et al., 2016). They may be impact related remnants or part of the pre-impact surface but are no evidence for an active interior of Ceres within the Sintana quadrangle.

Linear structures are interpreted to be secondary crater chains or impact-related structures, such as concentric fractures in Tupo, similar to fractures in Occator and Dantu, which are interpreted to be the result of cooling-melting processes or the sinking of the crater floor (Buczkowski et al., 2016; von der Gathen et al., 2016). We suggest that the specific arrangement of ridges inside the Sintana crater is the result of a converging motion of terraces, similar to radial transpression ridges in craters described by Kenkmann and Dalwigk (2000) that are formed to compensate centro-symmetric motion of masses during the gravity-collapse of the crater, as illustrated in Fig. 3-13.

The mapping process is restricted by the limit of resolutions, especially for linear structures. A clear distinction between impact-generated secondary craters or tectonically generated pit craters cannot be drawn with absolute certainty. Additionally, there are a few image gaps in the mosaics, and unfavorable illumination conditions (shadows) towards the South Pole. Due to a high occurrence of secondary craters, we restricted age estimates to two units: the cratered terrain, by only using craters larger than 5 km, and Tupo ejecta as a low overprinted counting area. Besides contamination with secondary craters, there is a systematic error due to uncertainties in both production and chronology function and their interaction, and also the statistical error (Michael and Neukum, 2010).

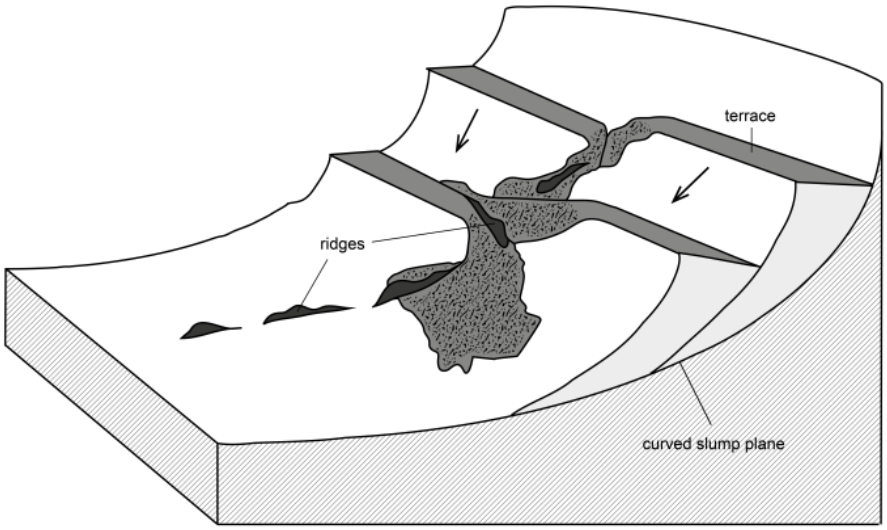

Fig. 3-13. Schematic illustration of two colliding terrace bundles in the southern part of Sintana crater. Collision results in radial ridges and chaotic slumps and landslides.

3.7 CONCLUSION

Absolute age estimates suggest that the Sintana quadrangle was overprinted, possibly by the same material that fills and surrounds the Kerwan impact basin, and therefore is less heavily cratered than other regions of Ceres' surface. Endogenic activity is not observed for this region of Ceres because there is a lack of morphologically distinct volcanic landforms and related tectonic structures. The absence of such structures might be due to the resurfacing by impact-induced melting or different interior conditions in this area of Ceres that might be related to a thicker crust or different temperature conditions in the interior. Identified mass wasting features support an ice-rich subsurface composition.

4 ROTATIONAL EFFECTS ON CERES' EJECTA DEPOSITION

4.1 INTRODUCTION

Geologic mapping of the Sinatana quadrangle in chapter 3, global imagery by the Dawn Framing Camera and numerical models (Nathues et al., 2017; Schmedemann et al., 2017) suggest that Ceres' rotation largely influences the deposition of ejecta. The following chapter evaluates to what extent the rotation of the dwarf planet influences the distribution of ejecta and provides physical constraints for the origin of structures, such as secondary crater chains and processes, such as resurfacing. In the following chapter, the ejection behavior on Ceres is compared with ejecta deposition on Mars in order to estimate the effect of the Coriolis force. Furthermore, the influence of the latitude-dependency of the Coriolis effect and the impact geometry on ejecta deposition is quantified. To analyze the origin of secondary cratering, particle sizes are estimated for the ejecta of several large craters on Ceres. The discussion is continued in chapter 5 for the special case of boulder craters.

4.2 RESULTS

4.2.1 ROTATIONAL EFFECTS ON CERES AND MARS

The rotational speed, but also the size of a planetary body, influences the shape of ejecta deposits, because the trajectories of the ejected particles are deflected by the Coriolis effect. Ceres rotates relatively fast with a period of ~9 hrs. In order to evaluate the influence of rotation, the rotational effects on ejecta deposition on Ceres are compared with the ejecta deposition on the slower rotating Mars using the ballistic model described in section 2.2 that assumes a spherical symmetric body.

The properties of Ceres, such as rotational period, gravitational acceleration and composition, differ from Mars. All parameters that are used to calculate the landing sites are listed in Table 4-1. Mars with a radius of 3390 km (Seidelmann et al., 2007) is much larger than Ceres (476 km) and has a higher gravitational acceleration. Ceres is nearly spheroidal (Park et al., 2016) and Mars is an oblate spheroid (Melosh, 2011).

Mars' rotational period is slower than the rotational period of Ceres. The target density is 1815 kg/m^3 (Park et al., 2016) for Ceres' ice-rock mixture and 2582 kg/m^3 for the rocky Martian crust (Goossens et al., 2017). The average projectile impact velocities depend on the location of the planetary body within the Solar System. The model does not account for atmospheric effects,

even if Mars has a thin atmosphere (Nier and McElroy, 1977). Ceres, on the other hand, might have no or only a transient atmosphere (Russell et al., 2016). The model uses a vertical impact at the equator with a projectile diameter of 5 km and a projectile density of 3000 kg/m^3 for dense rock (Collins et al., 2005).

The resulting crater diameter produced by the same projectile diameter varies between the different planetary bodies. A 5-km impactor produces a 58-km crater on Ceres and a 38-km crater on Mars. As different as the crater size is, the rotational effect on ejecta deposition is also different. Fig. 4-1 illustrates the re-impact sites for selected ejection azimuths of the two investigated planetary bodies. A single landing site trajectory is composed of landing sites from particles ejected at different velocities at the same azimuth (one color). The trajectories of ejecta on Mars and Ceres are both influenced by rotation. The effects that are described in section 2.2.1 include a rightward deflection of trajectories in the northern hemisphere, and a leftward deflection in the southern hemisphere along with a westward shift of the landing sites, especially at the equator. Ceres, the faster rotating body, exhibits more deflected landing site trajectories than Mars. Ejecta that is thrown out to the east of the crater is deflected westwards. Re-impact sites north of the equator describe a clockwise rotation and re-impact sites south of the equator describe a counterclockwise rotation. Additionally, the rotational effects on planetary ejecta deposition are illustrated by re-impact sites as a function of ejection velocity in Fig. 4-2. Those landing sites are mostly symmetric to the equator, because an equatorial impact location was chosen. Particles of lower ejection velocities impact radial-symmetric to the crater center. Fast particles' re-impact site trajectories, on the contrary, are highly disturbed. Very fast particles accumulate at the equator and in parallels (at constant latitude) near the equator. In summary, the fast rotation of Ceres produces especially asymmetric east-west ejecta deposition patterns compared to the planet Mars.

Table 4-1. Input parameters for Ceres and Mars

	Ceres	Mars
Mean Radius [km]	476 (Thomas et al., 2005)	3390 (Seidelmann et al., 2007)
Rotation Period [h]	9.075 (Thomas et al., 2005)	24.624 (https://ssd.jpl.nasa.gov/?planet_phys_par)
Escape Velocity [km/s]	0.51 (de Elía and Di Sisto, 2011)	5.03 (https://ssd.jpl.nasa.gov/?planet_phys_par)

Bulk Density [kg/m^3]	2162 (Park et al., 2016)	3934 (https://ssd.jpl.nasa.gov/?planet_phys_par)
Strength-to-Gravity Transition Diameter Dsg [km]	1.75 (Hiesinger et al., 2016)	0.1 (Ivanov, 2001)
Simple-to-Complex Transition Diameter Dsc [km]	10.3 (Hiesinger et al., 2016)	7 (Garvin et al., 2000)
Gravitational Acceleration [km/s^2]	0.00028 (Thomas et al., 2005)	0.00371 (https://ssd.jpl.nasa.gov/?planet_phys_par)
Average Impact Velocity [km/s]	4.79 (O'Brien and Sykes, 2011)	8.62 (Ivanov, 2001)
Target Density Surface (Outer Shell) [kg/m^3]	1815 (Park et al., 2016)	2582 (Goossens et al., 2017)

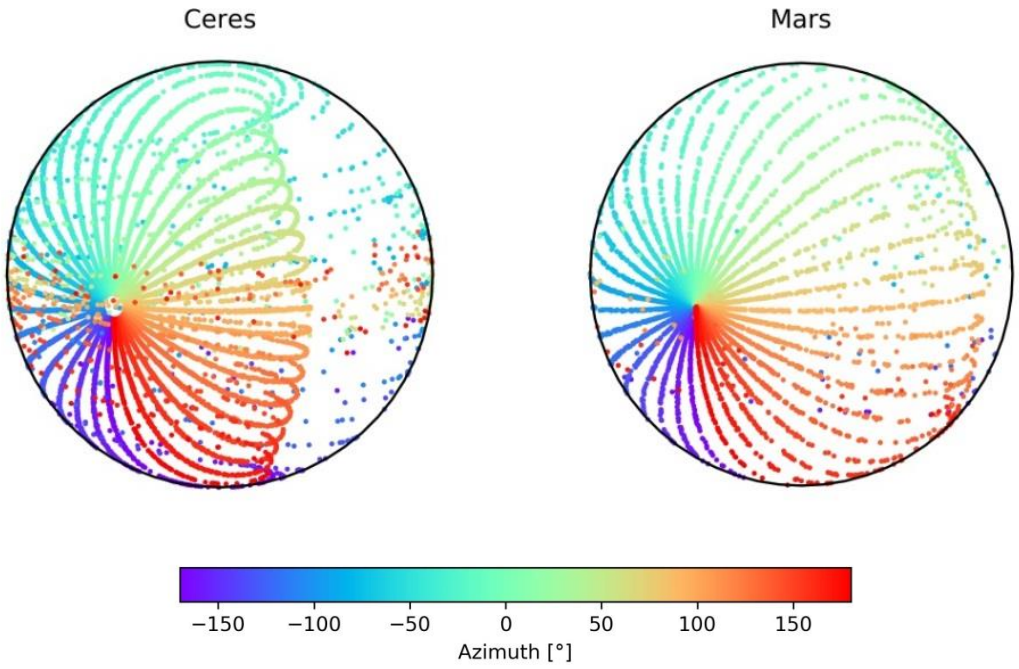

Fig. 4-1. Landing sites of particles ejected at the equator, color-coded by ejection azimuth, for Ceres and Mars. The pattern is composed of landing sites from particles ejected at different velocities from the same azimuth (one color). The orthographic projection is centered at 30°E and 10°N.

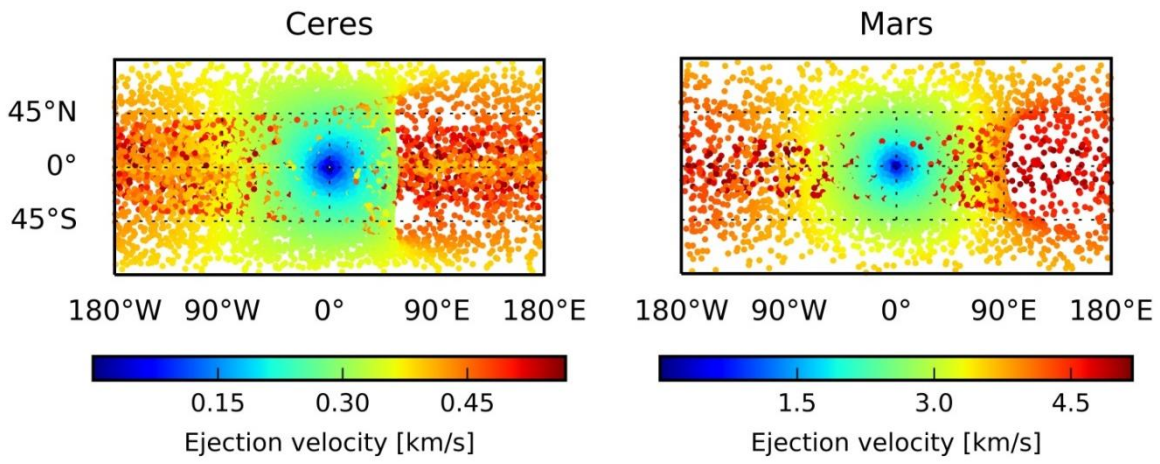

Fig. 4-2. Global re-impact patterns for Ceres and Mars are illustrated. Landing locations are color-coded by ejection velocity.

4.2.2 Parameters of Ejecta Deposition on Ceres

4.2.2.1 Crater Latitude

The following section discusses the latitude-dependency of the Coriolis effect. To demonstrate the latitudinal effects of ejecta deposition under Cerean conditions, a notional 50-km impact crater is placed at the two poles, the equator and the two mid-latitudes at ± 45°. The impact angle is vertical with respect to the surface. The parameters for Ceres are listed in Table 4-1. Fig. 4-3 illustrates particle trajectories of landing sites for an equatorial and the two mid-latitude impacts. Only landing sites for azimuths at intervals of every 10° as a function of ejection velocity in plate carrée projection are shown. They illustrate the relationship between ejection velocity and flight range. In addition, Fig. 4-4 illustrates particle landing sites for an equatorial and a mid-latitude impact for azimuths at intervals of 10° as a function of ejection azimuth in orthographic projection in order to illustrate the relationship between ejection direction and rotational effect. The landing sites of the crater at the equator are distributed symmetrically to it (Fig. 4-3 upper left). On the contrary, landing sites of the mid-latitude impact ejecta are asymmetric to the equator (Fig. 4-3 upper right, bottom). In the northern hemisphere, particle paths are deflected to the right of their original direction of motion as a result of the horizontal component of the Coriolis force that is maximal at the poles. Landing site trajectories of eastward moving particles are bent to the equator; landing sites trajectories of westward moving particles are bent to the poles. A clockwise rotation is the result (Fig. 4-4). That latter is not visible in the plate carrée projection because of the distortion of that projection. In the southern hemisphere, on the other hand, particle landing site trajectories are bent to the left of their path. Fast particles accumulate around the equator for an equatorial impact. In case of a mid-latitude impact, high-velocity

particles accumulate at the same latitude but at the opposite hemisphere. In the event of a polar impact, particle landing sites form a spiral (Fig. 4-5) and very fast particles accumulate around the pole of the opposite hemisphere. An impact at latitude of 45° shows an asymmetric re-impact pattern. The pattern is the same for an impact at -45° latitude but mirrored at the equator (compare the latitudes ±45° in Fig. 4-3). That effect is also evident in the global re-impact pattern (Fig. 4-6) that illustrates the landing sites of all test particles.

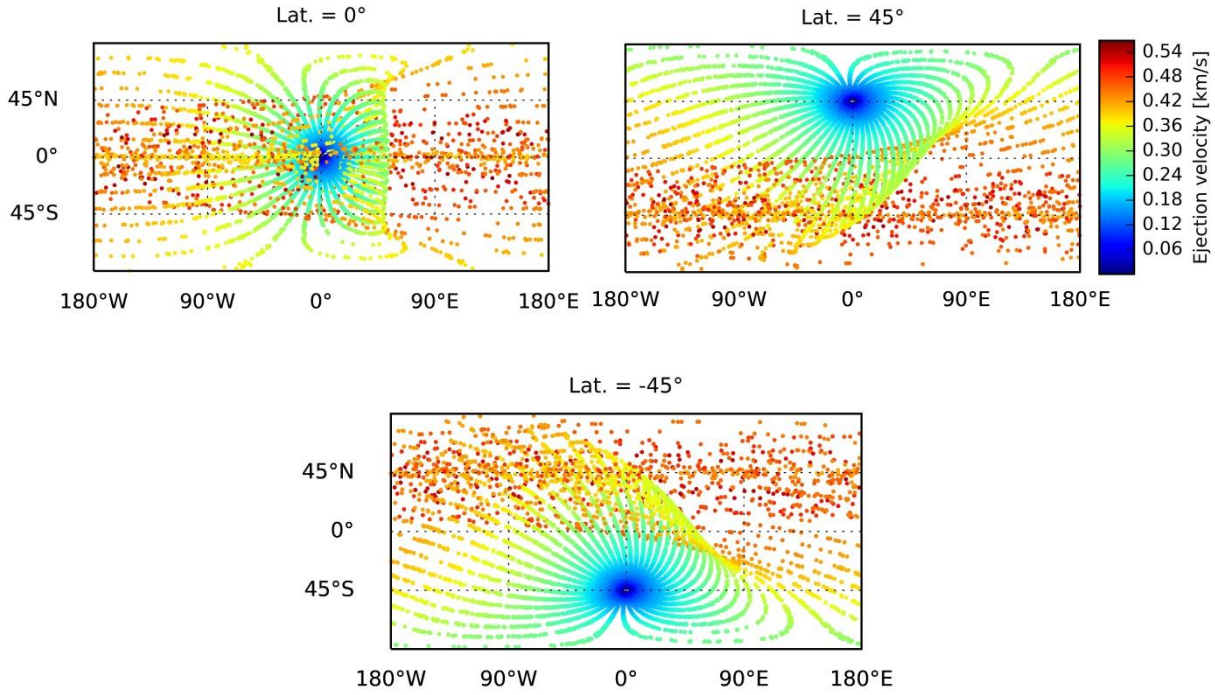

Fig. 4-3. Re-impact sites of particles ejected from a 50-km crater at the equator (upper left) and at a latitude of 45° (upper right) and -45° (lower image). The pattern is based on re-impact locations to specific start azimuths at intervals of 10° as a function of ejection velocity. Results are presented in a plate carrée projection.

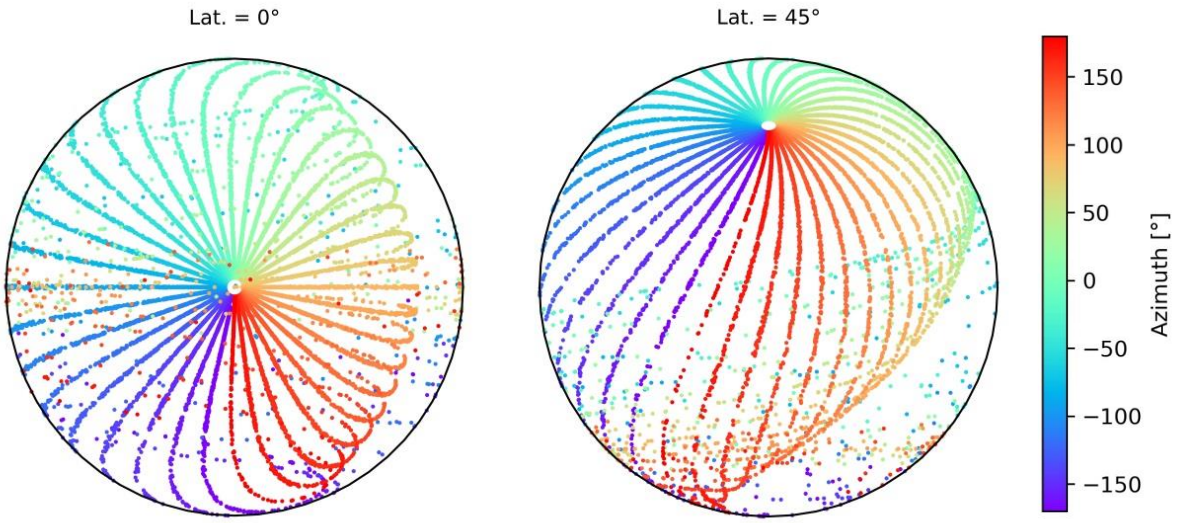

Fig. 4-4. Re-impact sites of particles ejected from a 50-km crater centered at the equator (left) and at a latitude of 45° (right). The pattern is based on re-impact locations to specific start azimuths at intervals of 10°. Impact locations are colored by start azimuth. Results are presented in an orthographic projection, centered at 0°E, 0°N.

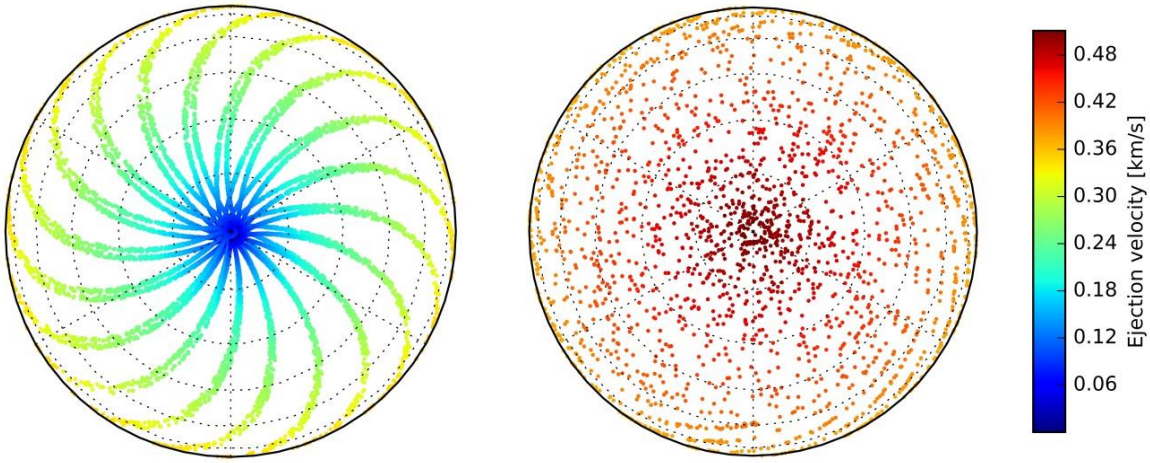

Fig. 4-5. Re-impact sites of particles ejected from a crater centered at the North Pole (90° latitude) out of re-impact locations to specific start azimuths at intervals of 10° as a function of ejection velocity. Left) The northern hemisphere with the impact location at the North Pole and a spiral landing site pattern. Right) The corresponding southern hemisphere. Fast particles accumulate at the South Pole. Results are presented in an orthographic projection.

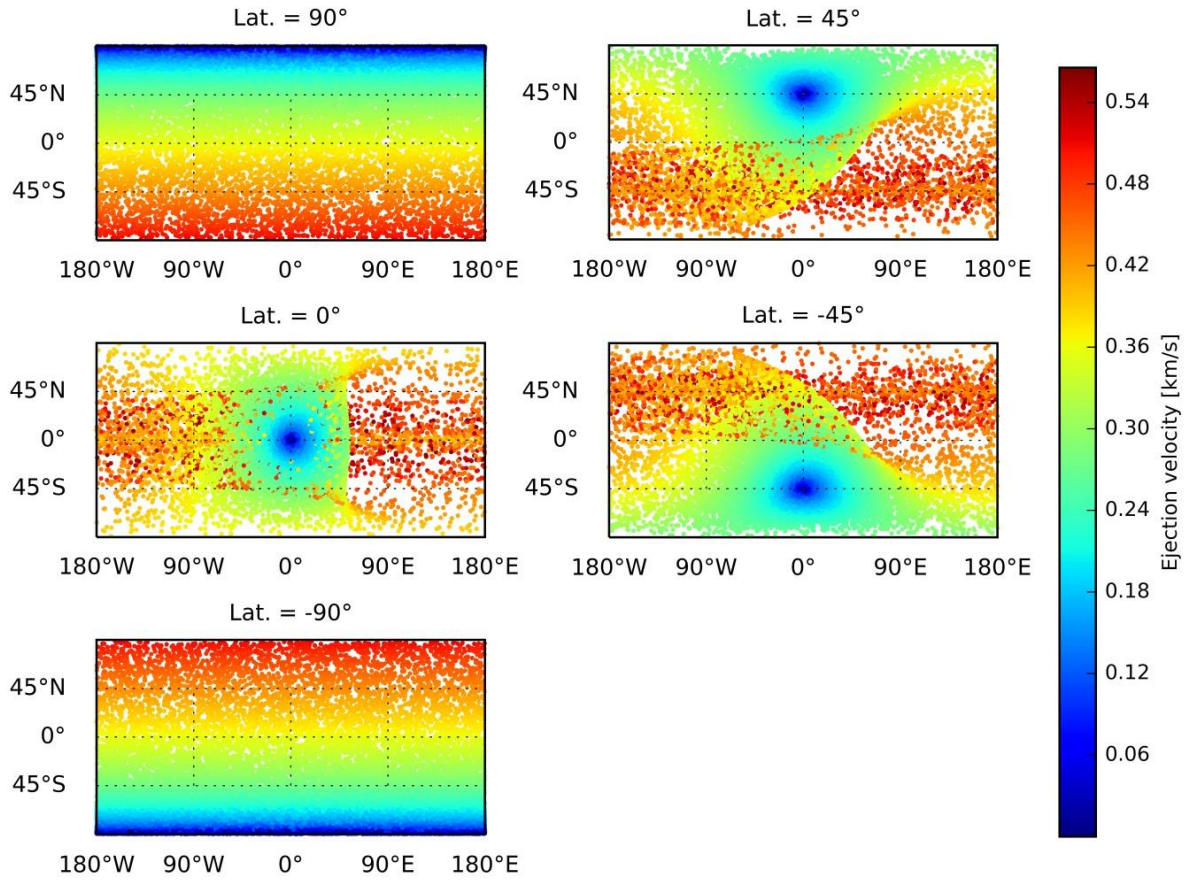

Fig. 4-6. Re-impact sites as a function of ejection velocity of a 50-km crater centered at different latitudes. Results are presented in a plate carrée projection. Note that particles might be faster than the escape velocity because the shown velocity is the velocity without rotation.

4.2.2.2 Crater Diameter

The size of the impact and hence the available energy influences the velocity range of ejected particles and consequently their flight distance. Ejecta patterns for final (not transient, compare section 2.1.1.1) crater diameters between 5 and 300 km were calculated to cover the crater size range of larger craters on Ceres. The largest crater on Ceres is the 280 km Kerwan basin. The size of an impact crater is determined by the projectile diameter, the impact velocity, the impact angle, Ceres' gravity and the material parameters of projectile and target. A generalized assumption can be that larger craters are produced by higher energetic impacts. The resulting re-impact patterns (Fig. 4-7) show that impacts that produce large craters provide a higher amount of high-velocity particles, given the same number of test particles. As discussed in section 4.2.2.1, fast particles accumulate at the equator or at parallel latitudes close to it. The larger the final crater size, the broader and fuller the high-velocity band at the equator. Based on the fact that the number of particles is the same for all diameters in this simulation, the ejecta of larger craters appears more widely spread across Ceres' surface. For the 5-km crater, re-impact trajectories of particles that

are ejected to the east turn westward below 60°E. For the 300-km crater, the trajectories turn westward at longitudes higher than 60°E.

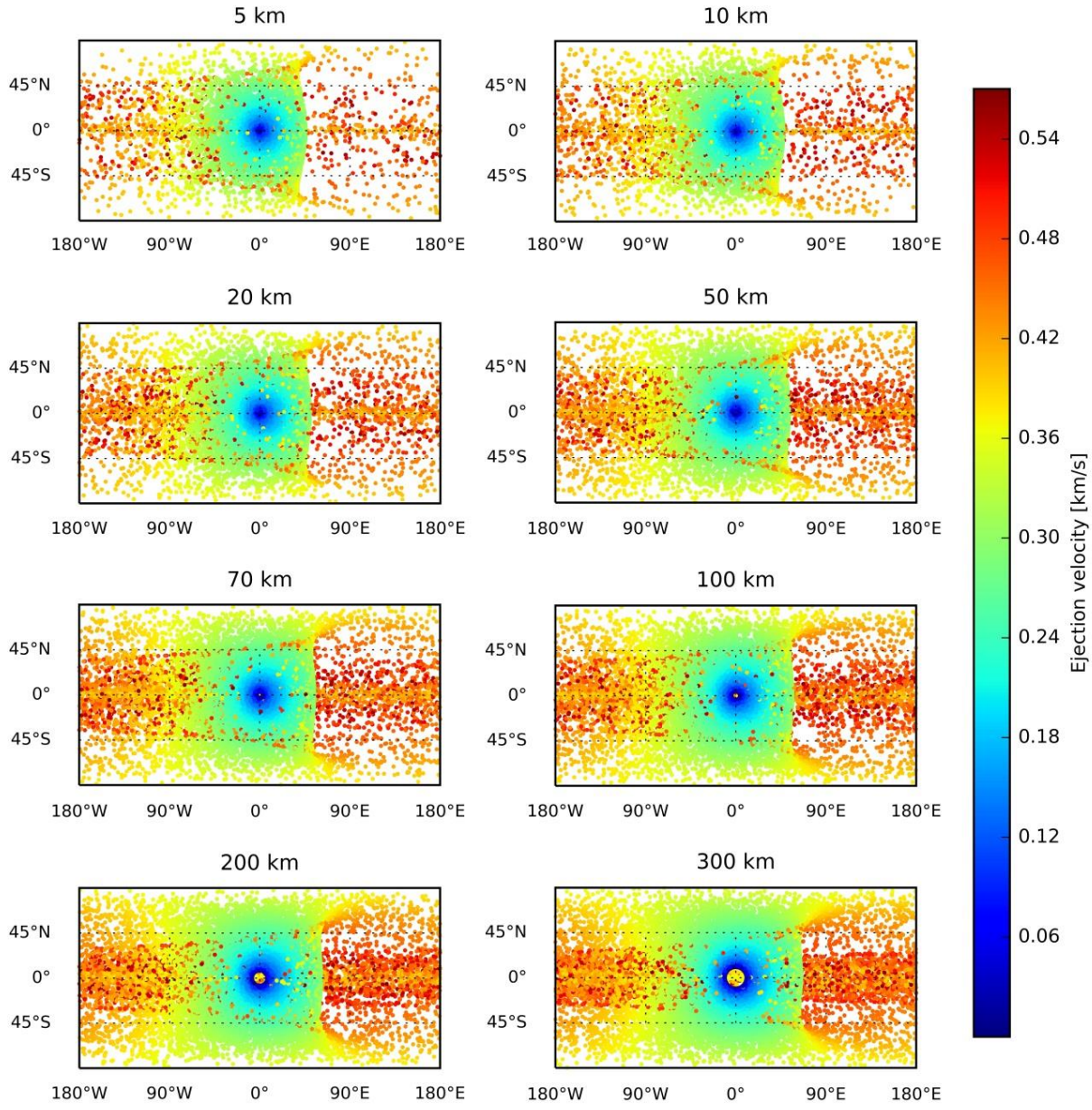

Fig. 4-7. Re-impact patterns for impact craters at the equator with diameters between 5 and 300 km. Note that particles might be faster than the escape velocity because the shown velocity is the velocity without rotation.

4.2.2.3 Impact Geometry

In reality, oblique impacts are very common (Shoemaker, 1962). The impact angle and the impact direction become relevant for the ejection distribution. The impact geometry is always a combination of impact angle and impact direction. Nevertheless, both parameters are analyzed independently in the following two sections by keeping the other parameter constant.

4.2.2.3.1 Impact Angle

To define the effect of the impact angle on both, re-impact pattern and single azimuthal landing site trajectories, the impact angle is varied at an interval of 10° between 10° and 90° with respect to the horizontal (surface). The notional impact direction is from the north (0°) and the diameter of the impact crater is 50 km. It is located at the equator. The impact angle of the projectile influences the particles' landing sites (Fig. 4-8). Oblique impacts produce irregular ejection angles and velocities between the downrange and uprange side of the impact. Moreover, in combination with the impact direction of 0°, oblique impact angles produce patterns that are asymmetric to the equator. The more oblique the impact, the more asymmetric are the eastern landing site trajectories to the equator. More precisely, eastern landing site trajectories to the north of the equator turn to the west at lower longitudes than eastern landing site trajectories to the south of the equator. The asymmetry is also prominent for east-west landing site trajectories that run in the vicinity of the equator. The variation in ejecta distribution between different impact angles is illustrated by the landing sites in Fig. 4-9. Keep in mind that the resulting pattern in Fig. 4-9 is a combination of impact direction and angle.

4.2.2.3.2 Projectile Incoming Direction

In the case of an oblique impact, the incoming direction of the projectile is an additional factor that is able to alter the ejecta deposition pattern. To define the effect of the impact direction on the re-impact pattern, the incoming direction of the projectile is varied at intervals of 45°. The impact angle is fixed at 45° and the 50-km crater is located at the equator. By azimuth color coded re-impact sites in Figure 4-10 illustrate that the incoming direction of the projectile alters trajectories in the line of that direction. The impact from a direction (azimuth) of 0° (north) distorts especially the flight paths to the north of the impact. In contrast, the same northern trajectories seem to be less influenced by an impact from 180° (south). This time, the landing site trajectories south of the impact are altered. In all cases, landing site trajectories close to the equator are much more scattered compared to the vertical impact scenario (e.g. Fig. 4-3). The trajectories are no more perfectly symmetric to the equator for an oblique impact. The effect of the incoming direction can be seen in the global re-impact pattern (Fig. 4-11). The pattern varies between different incoming directions, especially for specific parts of the surface. Particles that are ejected at lower velocities (<~0.3 km/s) are less influenced by the impact geometry, because the magnitude of the Coriolis force depends on the magnitude of the velocity. The flight path and time of flight of low-velocity particles are shorter than those of high-velocity particles.

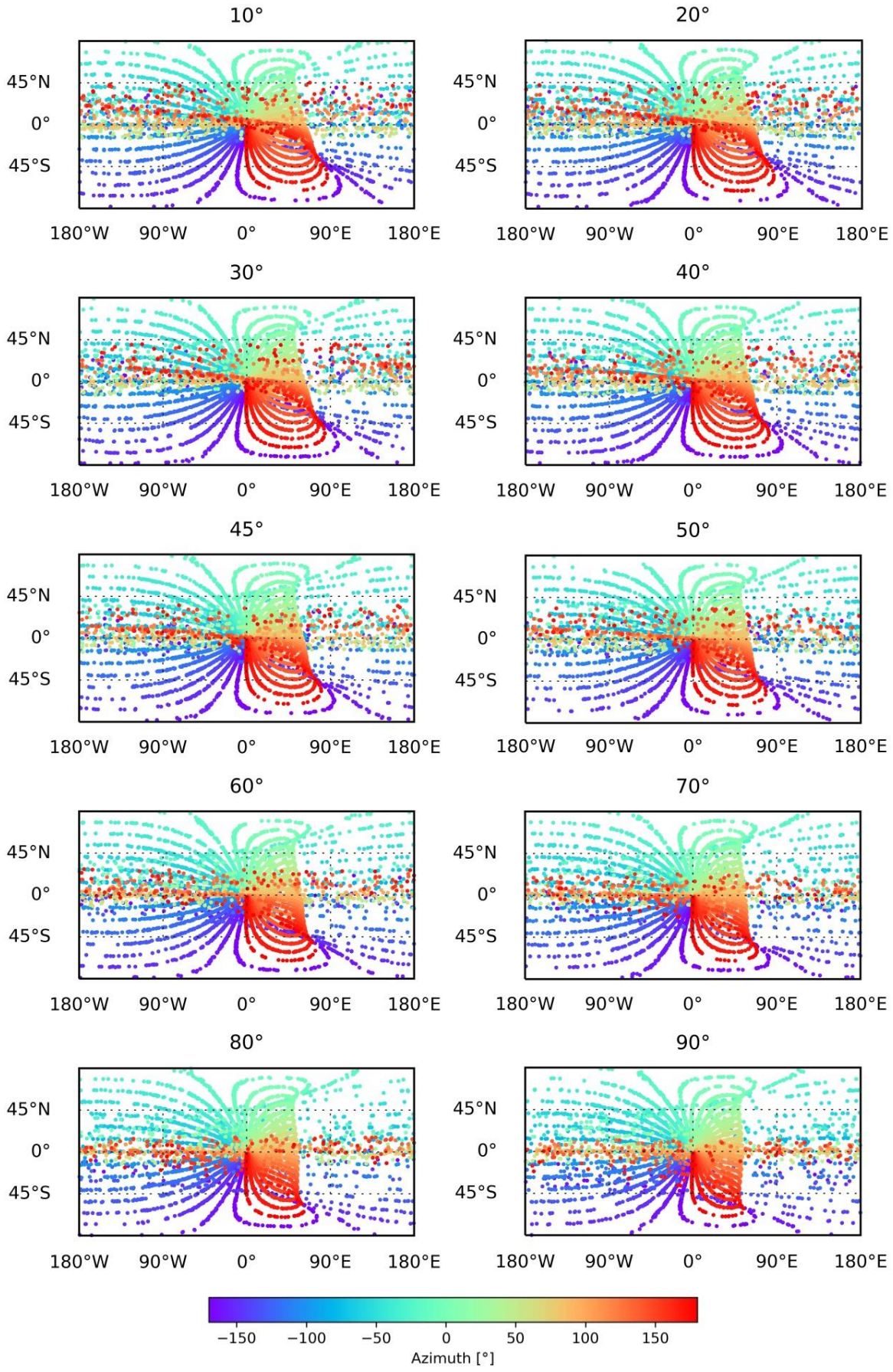
10°
20°
30°
40°
45°
50°
60°
70°
80°
90°
45°N
0°
45°S
180°W
90°W
0°
90°E
180°E
−150
−100
−50
0
50
100
150
Azimuth [°]

Fig. 4-8. Re-impact sites, color-coded by azimuth, at intervals of 10° for impact angles between 10° and 90° to the horizontal. The impact direction is north. The patterns are composed of landing sites from particles ejected at different velocities from the same azimuth (one color).

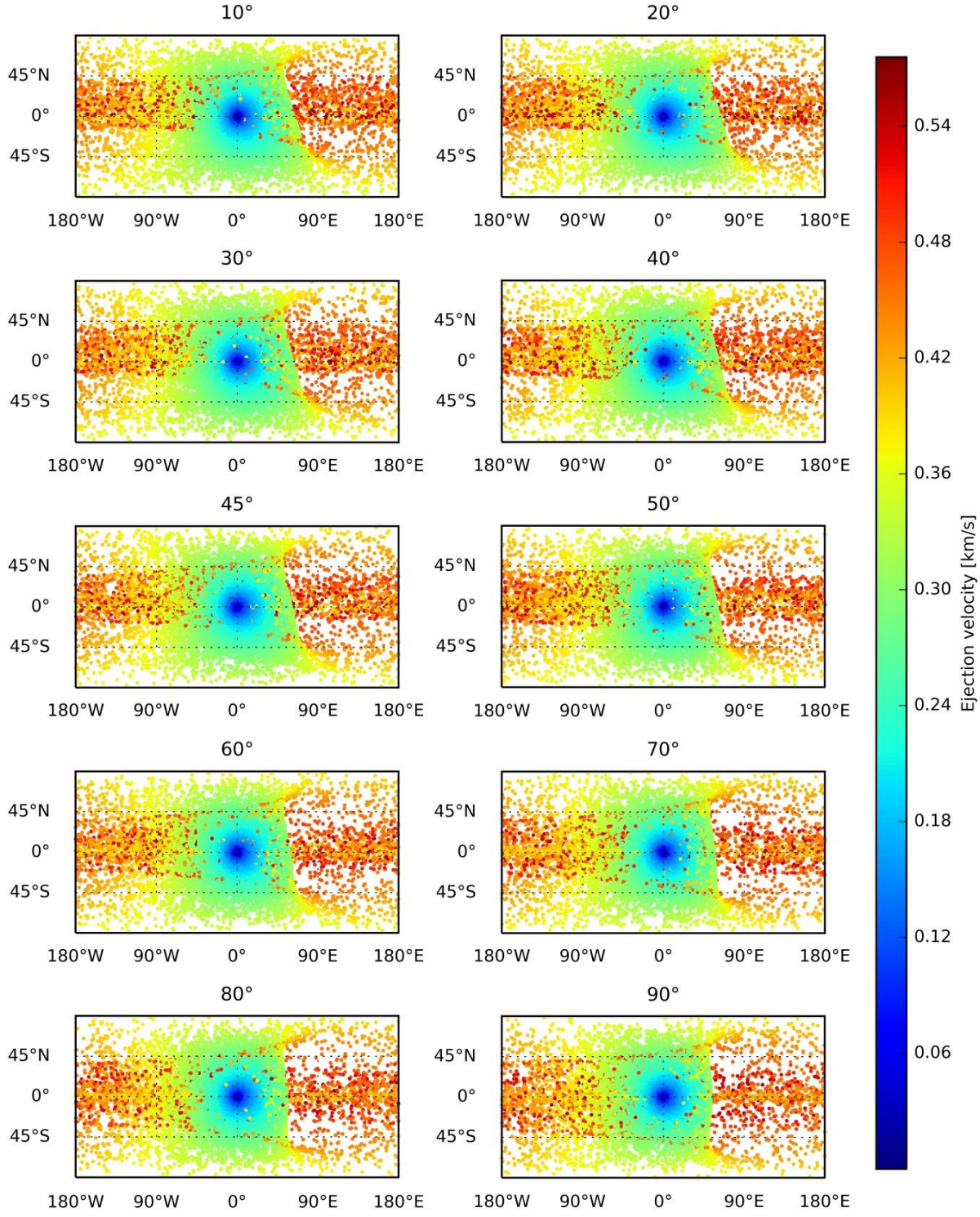

Fig. 4-9. Re-impact locations, color-coded by ejection velocity, for impact angles between 10° and 90° to the horizontal. The impact direction is north. Note that particles might be faster than the escape velocity because the shown velocity is the velocity without rotation.

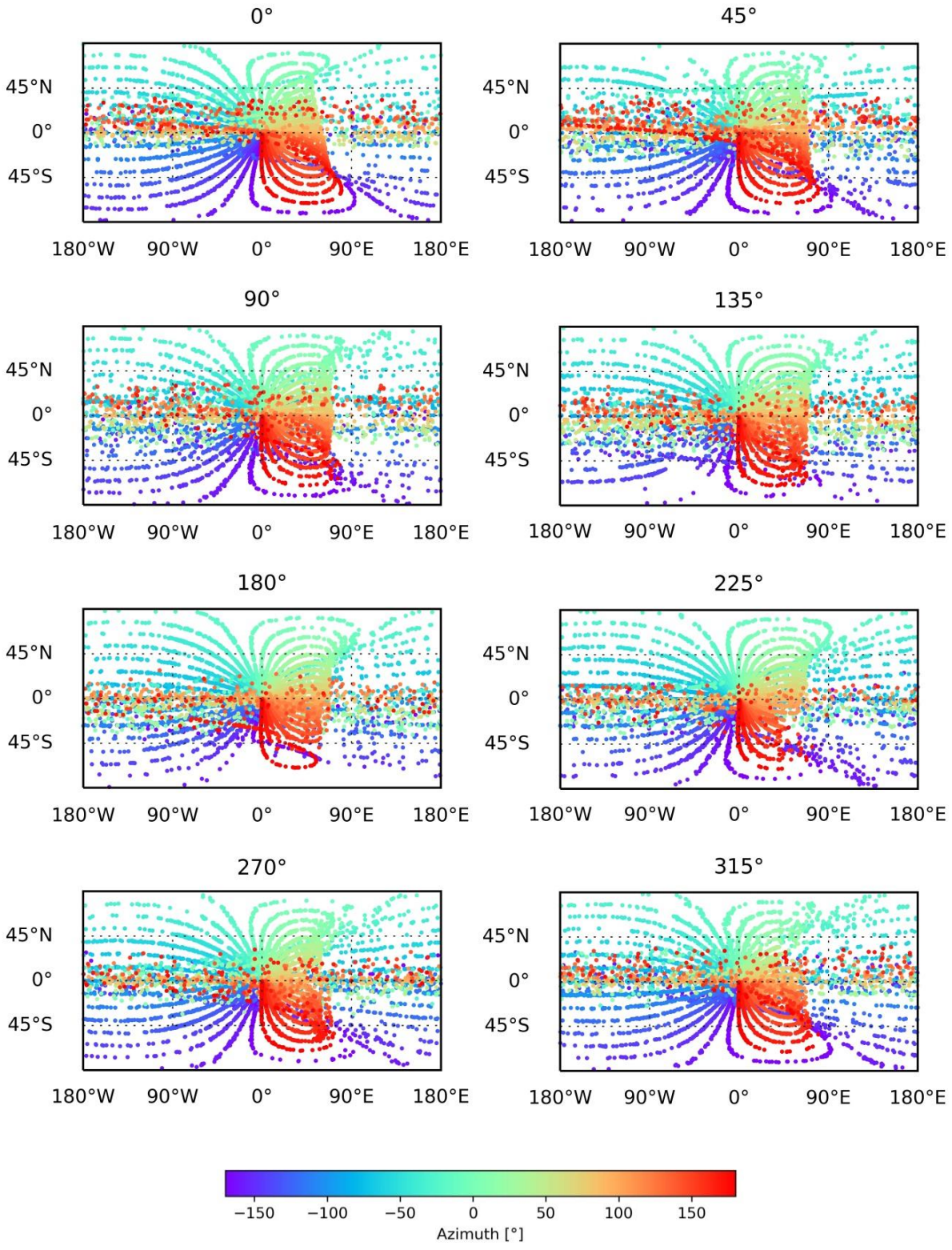

Fig. 4-10. Re-imapct sites, color-coded by azimuth, at intervals of 10° for different impact directions in an interval of 45°. The 0° direction corresponds to an impact from the north. The patterns are composed of landing sites from particles ejected at different velocities from the same azimuth (one color).

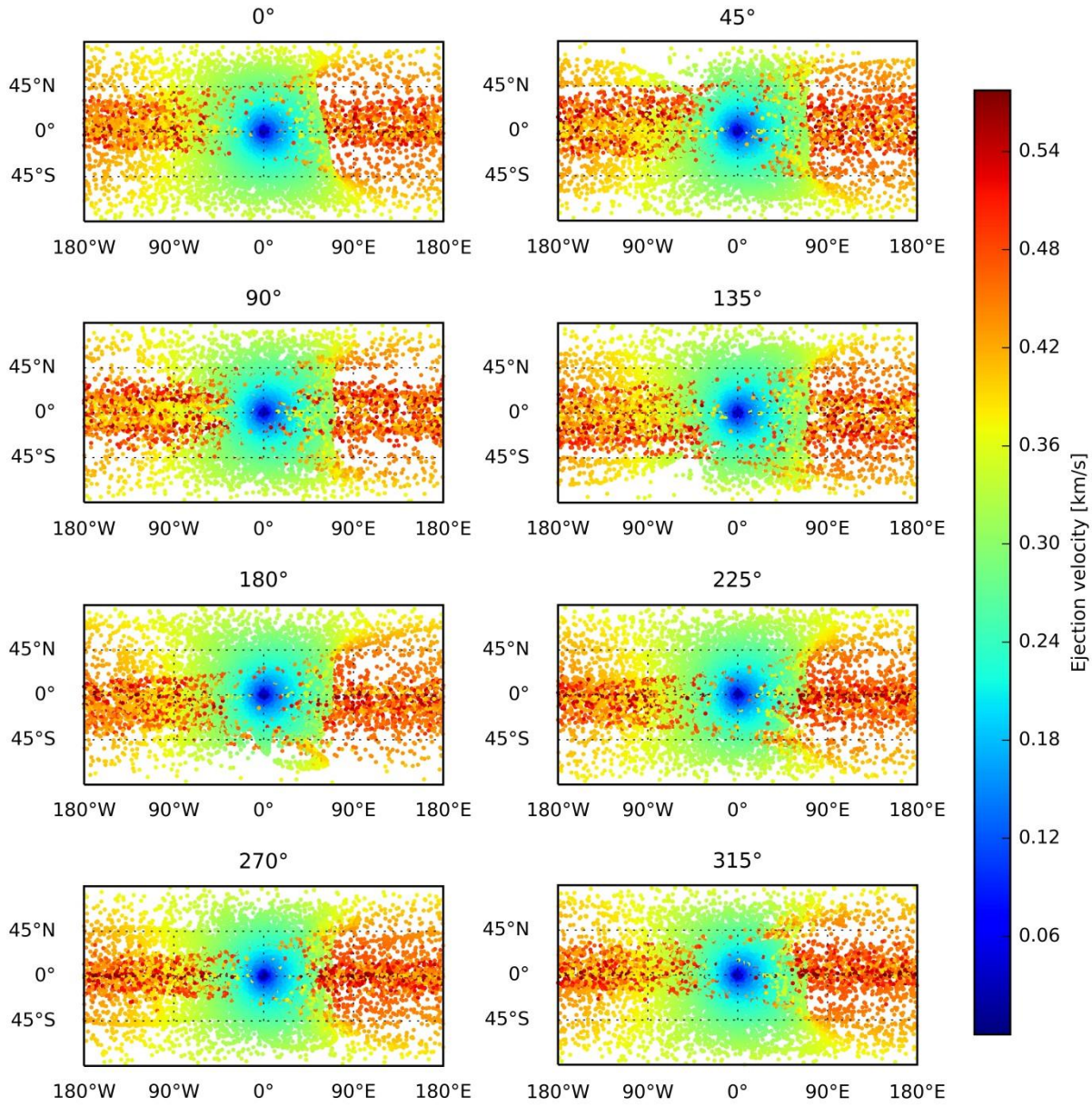

Fig. 4-11. Re-impact sites, color-coded by ejection velocity, for different impact directions at intervals of 45°. Note that particles might be faster than the escape velocity because the shown velocity is the velocity without rotation.

4.2.3 CRATERS ON CERES

Ceres' surface is dominated by several large impact craters. As demonstrated in the sections above, high-energetic impacts produce ejecta that covers large parts of the surface and their high-velocity ejecta is especially influenced by the rotation of Ceres. For many larger craters on Ceres, the ejecta blankets have vanished with time. Their original ejecta deposits are modeled in order to reconstruct the distribution of resurfacing one could expect from those craters. Re-impact sites are calculated for four of the most prominent craters of Ceres: Occator (92 km, 239.33°E, 19.82°N), Haulani (34 km, 10.77°E, 5.8°N), Yalode (260 km, 292.48°E, 42.58°S) and Kerwan (280 km, 123.99°E, 10.77°S). For Occator crater, Scully et al. (2018) conclude that the asymmetric ejecta of Occator along with furrows and impact crater chains in the northwest and the northeast of the crater hint to an impactor originating from northwest with an impact angle between 30 and 45°. The other craters' morphologies do not reveal the exact impact conditions. Therefore, the impact angle is chosen to be 45° for all craters as it is the most likely one (Shoemaker, 1962). The projectile incoming direction is set to northwest (315°) for Occator and north (0°) for the other craters.

The four selected craters demonstrate the strong latitudinal effect of ejecta deposition. Haulani is located in the vicinity of the equator. Its high-velocity particles accumulate close to the equator. The rest of the landing site trajectories run almost symmetrically to the equator (Fig. 4-12). Occator is located at latitude of ~20°. Its fast particles accumulate to the corresponding latitude south of the equator. As described before, the Coriolis effect leads to the phenomenon that particles that were ejected to the east turn and travel westwards. That observation has a north-south asymmetry. At lower latitudes it occurs at lower longitudes. Yalode is located at ~-43°S. Its fast particles accumulate at about the same latitude of the northern hemisphere. The re-impact pattern in Fig. 4-13 illustrates that Yalode ejecta might have covered the entire southern hemisphere.

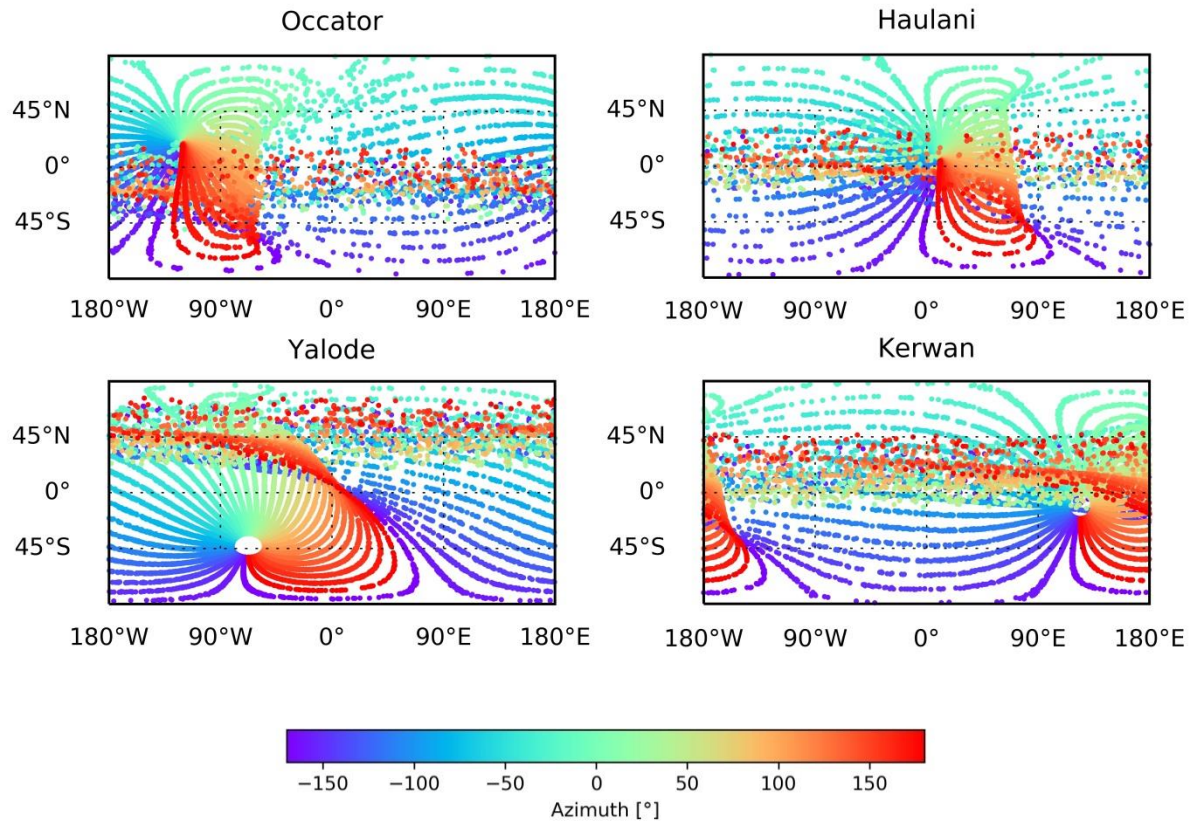

Fig. 4-12. The re-impact sites for the impacts Occator, Haulani, Yalode and Kerwan are color-coded by azimuths at an interval of 10°

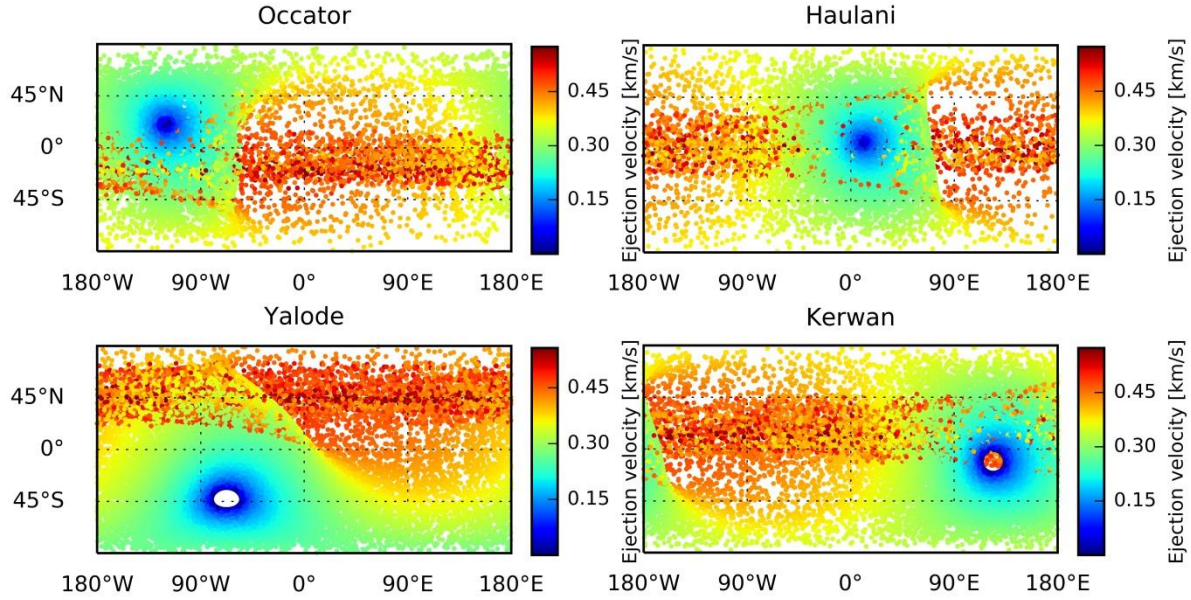

Fig. 4-13. By ejection velocity color coded re-impact locations for the Cerean craters Occator, Haulani, Yalode and Kerwan

4.2.4 Estimation of Particle Sizes

To estimate the sizes of ejected particles for given velocities, Eq. 2-42 is used. Particle sizes are estimated for the craters on Ceres that are discussed in section 4.2.3 and Urvara which is located directly next to Yalode, but has been proposed to be the source of secondary crater chains (Scully et al., 2017). The diameters of the projectiles that produced the impact craters Occator, Haulani, Yalode, Kerwan and Urvara are listed in Table 4-2. The ejection velocities of particles that return to the surface of Ceres are limited by the escape velocity of 0.51 km/s (de Elía and Di Sisto, 2011). The average impact velocity on Ceres is 4.79 km/s (O'Brien and Sykes, 2011) and the average surface density 1815 kg/m^3 (Park et al., 2016). The tensile stress of ice is reported to be 17 MPa (Weiss and Head, 2014), but it depends on the grain size and temperature (Petrovic, 2003). Ceres is an ice-rock mixture with at least 60% rock (Bland et al., 2016). Silicate content increases tensile strength (Petrovic, 2003). For a crystalline/sedimentary target, Weiss and Head (2014) report a tensile strength of 105 MPa and 170 MPa for a rocky target. For an ice-silicate mixture (30 wt % sand), Lange and Ahrens (1983) report a tensile strength of 22 MPa. Ceres' tensile strength will be somewhat higher than the reported mixture due to higher silicate content, but probably lower than the value reported for the fully rocky target. Presumably, the strength of the mixture will provide the minimum fragment size and the tensile strength of the sedimentary target the maximal fragment size that can be expected for Ceres.

Fig. 4-14 illustrates the range of fragment sizes that can be expected for each of the four chosen impacts for an ice-silicate mixture and a sedimentary surface composition. Ejection starts at the rim of the projectile. Overall, very slow ejection velocities will be related to large fragments. Especially at lower ejection velocities, an ice-rich target produces smaller fragments than a rocky target. In general, slower ejection velocities produce larger fragments. Slow and large fragments might be ejected and deposited as boulders. The fragment sizes for high-velocity particles (> 0.3 km/s) are illustrated in Fig. 4-15. The largest expectable fragment size depends on the applied tensile strength. Moreover, the available fragment sizes depend on the crater diameter. The smallest of the five craters Haulani would produce fragments as large of a couple of tens of meters in a sedimentary target. Fragments in an ice-silicate mixture would be smaller. Large basins, such as Yalode and Kerwan, would produce fragments that measure a couple of hundred meters in a sedimentary target and a couple of tens of meters in an ice-rich target. The resulting secondary crater diameters are calculated by using Eq. 2-34 and Eq. 2-36. Those secondary craters can measure several kilometers based on the maximum expected fragment sizes of a few hundred meters.

Table 4-2. Projectile diameters for the impacts that produced the Cerean craters Occator, Haulani, Yalode and Kerwan

Crater	Projectile Diameter [km]
Occator	7.26
Haulani	2.48
Yalode	22.22
Kerwan	24.32
Urvara	14.14

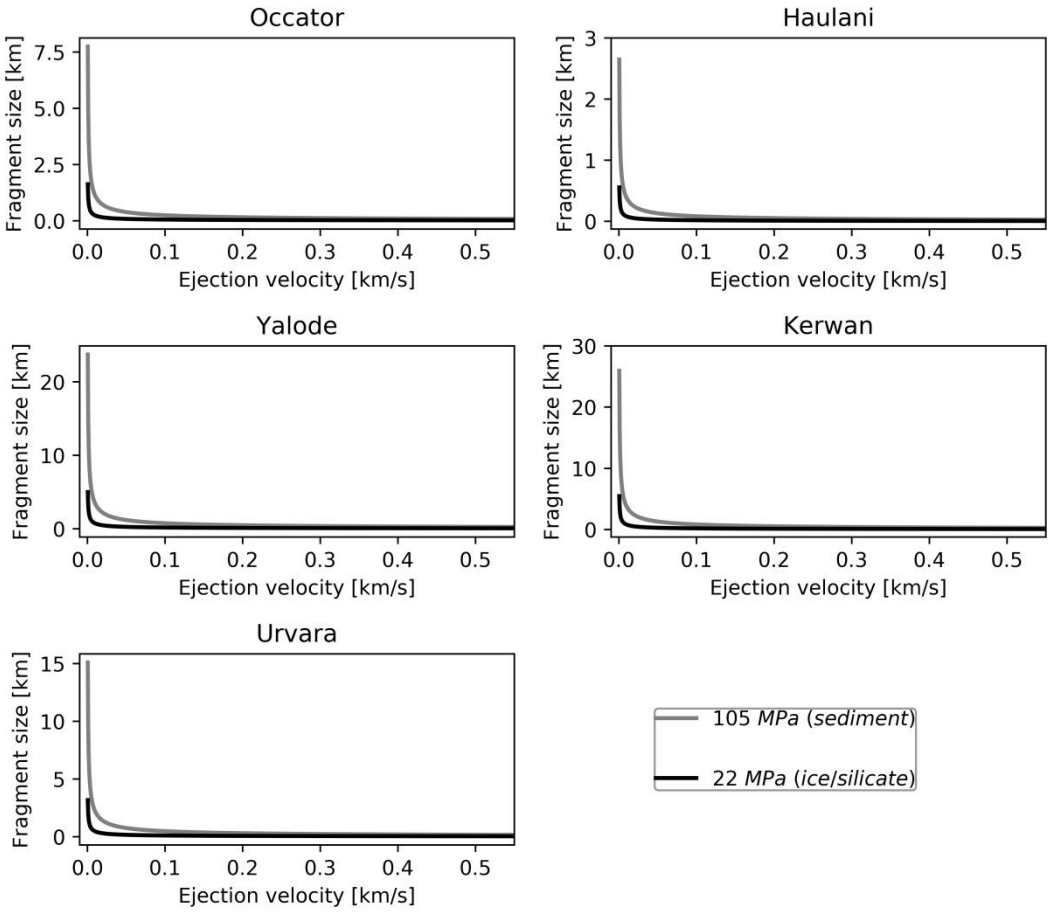

Fig. 4-14. Fragment sizes of particles in the ejection velocity range below the escape velocity of Ceres. Two materials are tested: sedimentary rock and an ice-silicate mixture with 30 wt % silicates.

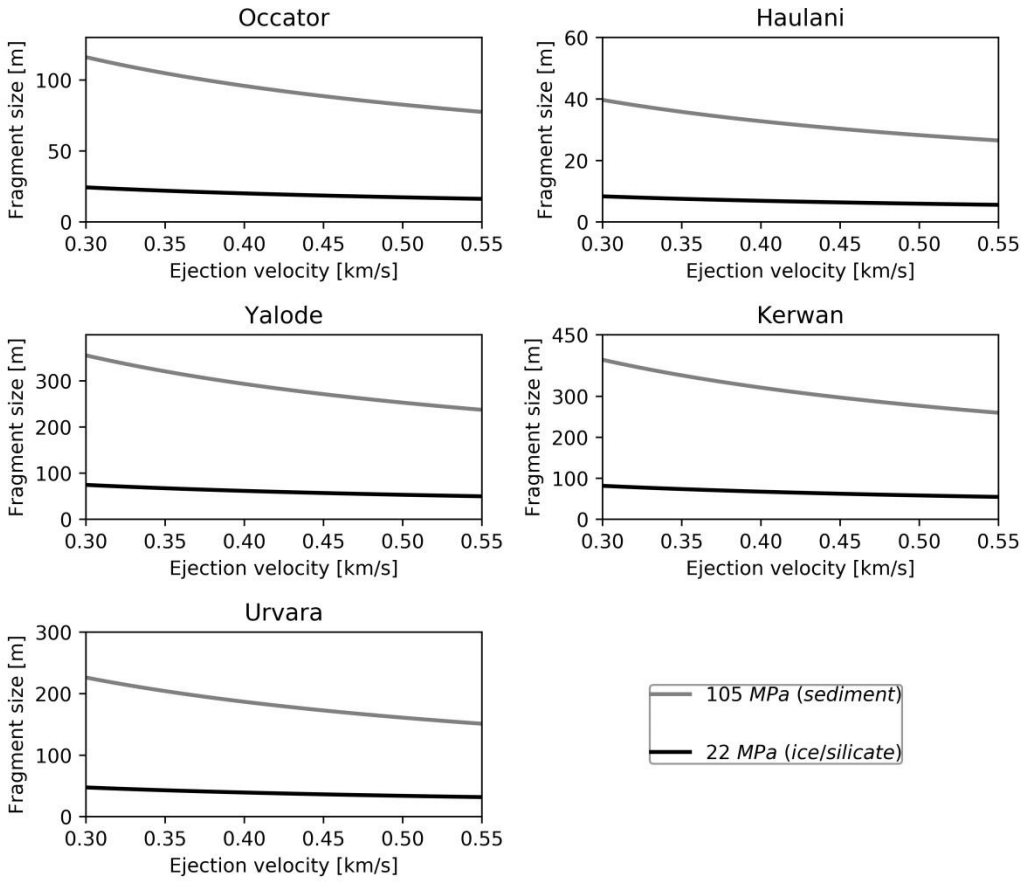

Fig. 4-15. Fragment sizes for particles ejected at high velocities above 0.3 km/s. Two materials are tested: sedimentary rock and an ice-silicate mixture with 30 wt % silicates.

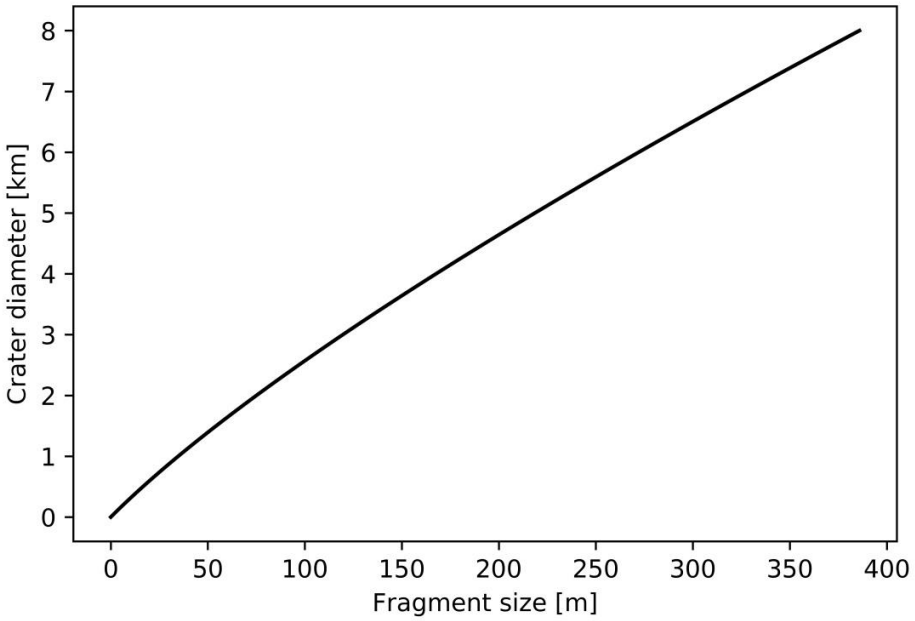

Fig. 4-16. Expected secondary crater diameters. Diameters are calculated from the estimated particles sizes in Fig. 4-15.

4.3 DISCUSSION

The model results of this chapter are important for the interpretation of observed surface morphologies. They show that ejecta of large craters, such as Yalode and Kerwan, could have resurfaced large parts of the Ceres' surface with irregular ejecta patterns, and hence covered preexisting craters and other structures. The latitude-parallel deposition of high-velocity particles might be an explanation for the east to west orientated secondary crater chains that cross large parts of Ceres' surface.

It should be noted that the analytical model only provides a general idea about the distribution of ejecta. The number of test particles does not reflect the exact amount and number of actually ejected particles. Material properties and impact geometry are always generalized assumptions. A more detailed discussion about the restriction in constraining material parameters for Ceres can be found in section 5.4. The simplifications of the applied model (spherical body, no atmosphere, no influence of other gravity fields …) that are described in section 2.2.4 are precise enough to provide helpful insights into Ceres' ejecta deposition, since it has no notable atmosphere, a spherical shape and it is not tidally-locked, such as icy satellites. The same still applies with some restrictions to Mars. A comparison with Vesta would be interesting, too, because it is also located in the asteroid belt and has an even more rapid rotation period than Ceres of 5.3 hours (Jutzi et al., 2013). Thus, the ejecta deposition is expected to be even more influenced by the Coriolis effect. The asteroid indeed shows many non-radial secondary crater chains with respect to the supposed primary craters. The northern hemisphere of Vesta, for instance, is highly contaminated with secondary impacts that probably originated from its largest impact crater Rheasilvia in the southern hemisphere (Schmedemann et al., 2014). Additionally, mass wasting in Rheasilvia shows spiral patterns that are explained by the Coriolis effect (Jutzi et al., 2013; Otto et al., 2013). The fragment sizes for the rocky surface of Vesta would be expected to be larger than for Ceres. Yet, the analytical model used in this work is not applicable for a comparison with other bodies, such as Vesta or icy satellites, as it would oversimplify the ejection scenario, because Vesta has an irregular shape (Konopliv et al., 2014) and icy satellites are highly influenced by the gravity field of their planet.

The rotational effects, such as the deflection of trajectories that are described in this chapter are in good agreement with existing models of Mercury (Dobrovolskis, 1981) and Mars (Wrobel, 2004). It has been previously shown by Wrobel (2004) that distal ejecta on Mars tends to wraps around the equator for low-latitude impacts and at the pole for high-latitude craters. As a consequence, craters, such as the high-latitude crater Lyot on Mars are able to provide high-velocity ejecta concentrated at distal areas in the opposite hemisphere. Wrobel (2004)

conclude that the distal ejecta therefore "should be rich in melt and/or glass". The example for Mars in this chapter is in agreement with those results. The ejecta of Ceres behaves in a similar manner, but the deflection of particle trajectories by the Coriolis effect is bigger, because of its rapid rotation. Thus, like on Mars, the surface areas on Ceres might be highly contaminated with distal ejecta.

The results of this work also suggest that the surface of Ceres might be resurfaced by the ejcta of large impacts. The calculated ejecta distribution agrees with results of numerical models of the impacts Urvara and Yalode (Crown et al., 2018; Schmedemann et al., 2017; Scully et al., 2017) that are shown in Fig. 4-17. Both model results are in good agreement with the assumption proposed in Hiesinger et al. (2016) that large craters in the southern hemisphere, such as Yalode and Urvara are responsible for a less heavily cratered southern hemisphere.

This work proposes non-linear secondary crater chains that originate from large impacts. Secondary crater chains are, for instance, observed in the Sintana quadrangle (section 3.3.1). Fig. 4-18 shows the most prominent linear features on Ceres including secondary crater chains (Scully et al., 2017). Many secondary craters concentrate in clusters or chains (Crown et al., 2018). Schmedemann et al. (2017) numerically modeled the ejecta distribution of the Urvara crater (170 km, 249.24°E, 45.66°S). The results indicate that the secondary crater chains Junina Catenae could have formed by Urvara ejecta. Junina Catenae (from ~12 to 46°N and ~95 to 265°E) consists of about eleven crater chains that are not radial to the proposed source crater Urvara. Mapping results agree with the numeral model observation that low-velocity ejecta will form radial secondary crater chains and high-velocity ejecta will form non-radial chains that are highly bent by the rotational effect (Scully et al., 2017). In the Urvara ejecta model that is compared with the morphology in Scully et al. (2017), secondary craters of Junina Catenae (Fig. 4-18 and Fig. 4-19) are produced by particles with high impact velocities of above ~ 400 m/s. The average width of the single chains is between 1 and 4 km. Those widths are in agreement with the calculated fragment sizes and the resulting crater diameters in section 4.2.4. Urvara fragments that can be as large as ~200 m would produce craters up to ~5 km. Very large fragments on the other hand might already disrupt during their flight, because of a break-up due to, for instance, collision or physical instability depending on the exact material composition (Li et al., 2016).

Superposed secondary craters can falsify planetary surface ages (Michael et al., 2012) as they tend to make surfaces older. Ceres' surface is highly contaminated with secondary craters and proximal craters often form clusters (Schmedemann et al., 2016). Age determination tools, such as CraterStats (Michael et al., 2012), are able to apply randomness analyses and check for clustering. Those clustered diameter ranges can then be excluded from the measurements. In addition,

secondary crater chains can be excluded directly during the process of crater counting. For the ages estimation of the background unit in the Sintana region, only craters larger than 5 km were included. Tupo crater was chosen, because its young ejecta blanket is supposed to be barely overprinted (section 3.2). However, there is no method to find randomly distributed secondary craters, because they are not distinguishable from primary ones.

To summarize, in agreement with numerical models and morphometric analyses, the asymmetric ejecta of large craters can reach the entire surface. Large particle diameters, even for high ejection velocities, infer that the chance of non-radial distal secondary crater chains needs to be considered for all larger craters on Ceres.

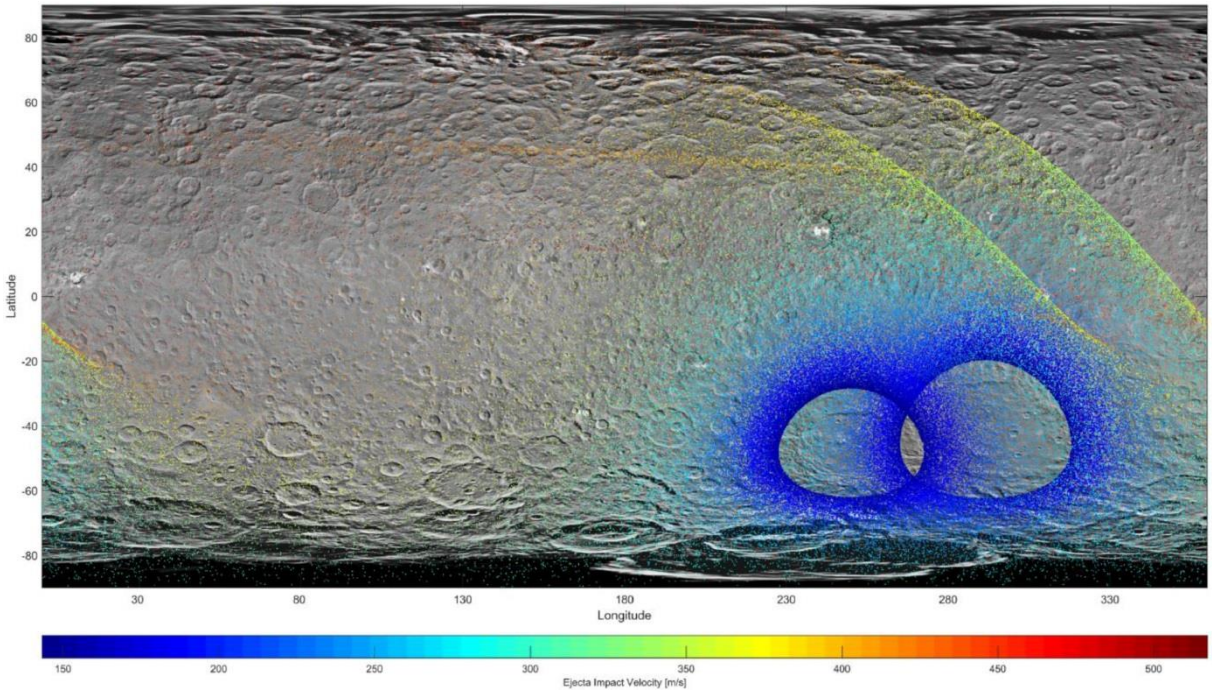

Fig. 4-17. Impact locations of ejecta tracer particles as a function of their impact velocity for the craters Urvara and Yalode from Crown et al. (2018). Particle densities should illustrate the possibility of secondary craters.

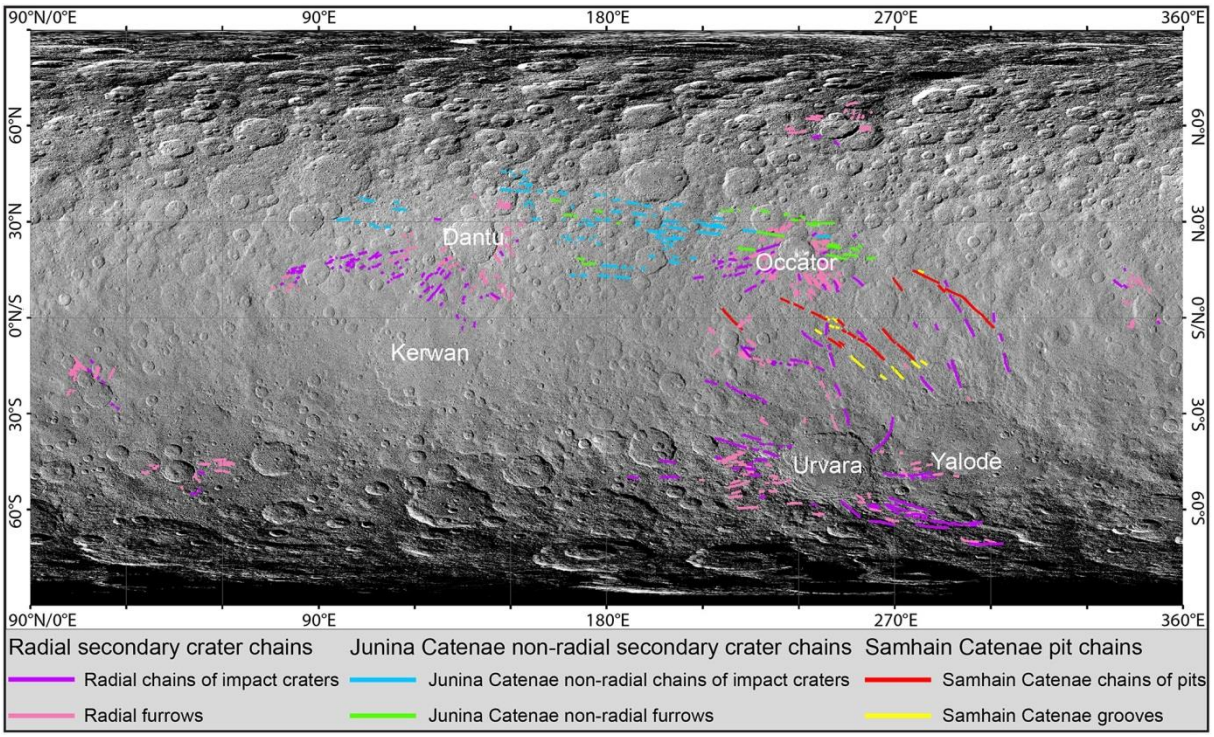

Fig. 4-18. Global map of linear features and their classes on Ceres from Scully et al. (2017)

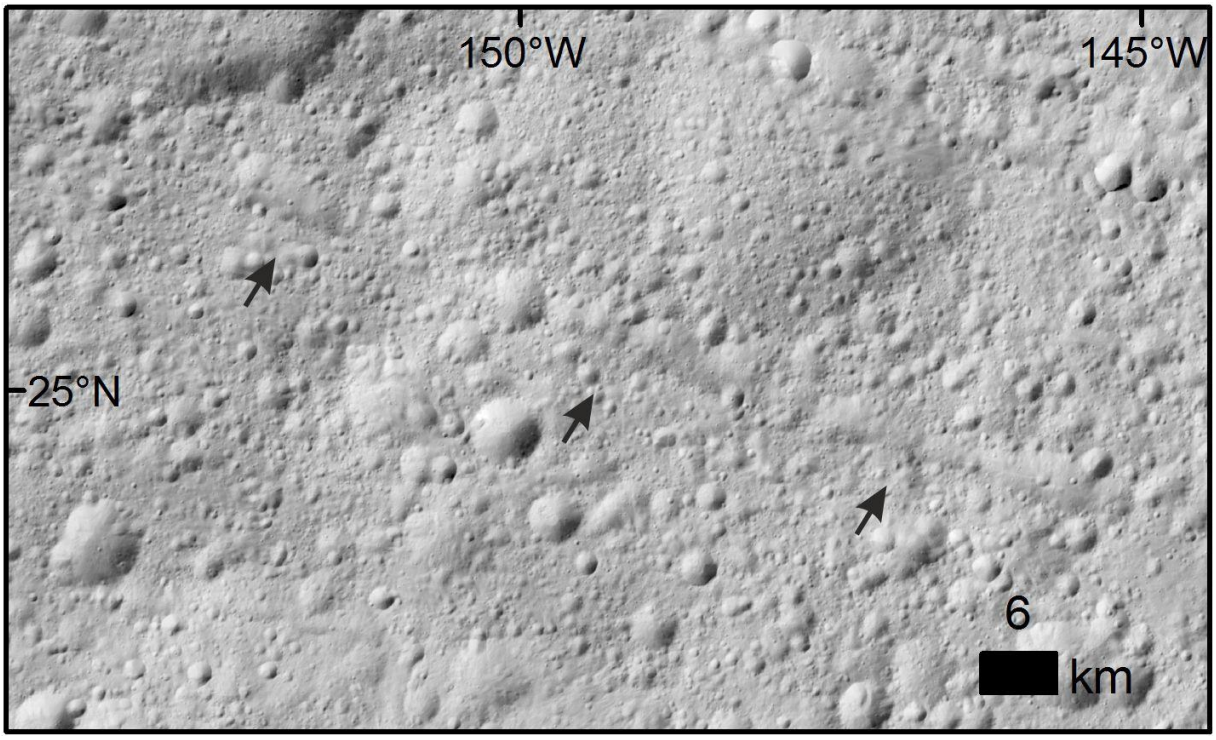

Fig. 4-19. Secondary crater chains of the formation Junina Catenae.

5 Global and Local Re-impact and Velocity Regime of Ballistic Ejecta of Boulder Craters on Ceres

This chapter has been published as the following peer-reviewed article:

F. Schulzeck, S.E. Schröder, N. Schmedemann, K. Stephan, R. Jaumann, C.A. Raymond, C.T. Russell, 2018. Global and local re-impact and velocity regime of ballistic ejecta of boulder craters on Ceres. Planetary and Space Science. 153, 142-156.

The article may be found using this link: https://doi.org/10.1016/j.pss.2018.02.004

A detailed description of the contribution of the thesis author can be found in section 1.3.

Abstract

Imaging by the Dawn-spacecraft reveals that fresh craters on Ceres below 40 km often exhibit numerous boulders. We investigate how the fast rotating, low-gravity regime on Ceres influences their deposition. We analyze size-frequency distributions of ejecta blocks of twelve boulder craters. Global and local landing sites of boulder crater ejecta and boulder velocities are determined by the analytical calculation of elliptic particle trajectories on a rotating body. The cumulative distributions of boulder diameters follow steep-sloped power-laws. We do not find a correlation between boulder size and the distance of a boulder to its primary crater. Due to Ceres' low gravitational acceleration and fast rotation, ejecta of analyzed boulder craters (8-31 km) can be deposited across the entire surface of the dwarf planet. The particle trajectories are strongly influenced by the Coriolis effect as well as the impact geometry. Fast ejecta of high-latitude craters accumulate close to the pole of the opposite hemisphere. Fast ejecta of low-latitude craters wraps around the equator. Rotational effects are also relevant for the low-velocity regime. Boulders are ejected at velocities up to 71 m/s.

5.1 Introduction

Boulders on planetary surfaces are widely studied, because they provide insight into impact processes and the composition of the upper layer of the planetary body. Ballistic models are widely used to describe ejecta emplacement across a planetary surface as well as the material exchange between planetary bodies.

Large ejecta blocks have been identified with imagery of NASA's Dawn spacecraft around morphologically fresh craters (Schröder et al., 2016). In 2015, NASA's Dawn spacecraft arrived at the dwarf planet Ceres to investigate its surface and interior. Onboard instruments include a Gamma Ray and Neutron Detector (GRaND), a Framing Camera (FC) and a visible and infrared

mapping spectrometer (VIR) (Russell and Raymond, 2011). In contrast to pre-Dawn models, mission data suggests that Ceres' heavily cratered crust consists of a ice-rock mixture with less than 40% ice (Bland et al., 2016). VIR data indicates a mixture of ammonia-bearing phyllosilicates, magnesium-bearing phyllosilicates and carbonates (De Sanctis et al., 2016). Ceres exhibits a wide morphologic variety of craters, but basins larger than 300 km are absent (Hiesinger et al., 2016). Furthermore, H_2O was detected, indicating water ice exposure (e.g. Combe et al., 2016). Floor fractured craters, large scale linear structures and domes are interpreted to be an indication for cryovolcanism (Buczkowski et al., 2016; Ruesch et al., 2016). There are various analytical and numerical studies about the ballistic emplacement of ejecta on bodies of the Solar System. Particle trajectory models provide insight into the correlation between ejecta and existing structures and formations, such as grooves on Phobos (e.g. Davis et al., 1981; Nayak and Asphaug, 2016; Wilson and Head, 2015) and the Moon (Wieczorek and Zuber, 2001), secondary craters (Bierhaus et al., 2012), magnetic anomalies on the Moon (Hood and Artemieva, 2008), tektites on Mars (Lorenz, 2000; Wrobel, 2004) and lunar rays (Giamboni, 1959). Furthermore, ejecta emplacement models provide explanations about observed ejecta geometries and hence the impact process itself, such as for Hale crater on Mars (Schultz and Wrobel, 2012) and Chicxulub crater on Earth (Alvarez, 1996). Studies on global trajectory regimes, the fate of ejected particles and the transfer of particles between planetary bodies, especially between planets and their satellites, have been conducted to examine the interaction between planetary bodies (e.g. Alvarellos et al., 2002; Gladman et al., 1995; Nayak et al., 2016).

Boulders have been investigated with various points of focus, depending on the planetary body and the available data. Size-frequency distributions and shapes of boulders have been studied on the Moon (e.g. Greenhagen et al., 2016; Krishna and Kumar, 2016), Mars (e.g. Di et al., 2016b; Golombek et al., 2003), satellites (e.g. Martens et al., 2015; Thomas et al., 2000), comets (e.g. Pajola et al., 2015), but especially on asteroids (e.g. Chapman et al., 2002; Jiang et al., 2015; Lee et al., 1996; Mazrouei et al., 2014; Michikami et al., 2008; Nakamura et al., 2008). Ejection velocities and in some cases ejection sites were estimated for the Moon (Bart and Melosh, 2010a; Bart and Melosh, 2010b; Vickery, 1986), Eros (Durda et al., 2012; Thomas et al., 2001), Lutetia (Küppers et al., 2012) and Ida (Geissler et al., 1996). On Ceres, trajectories of ejection particles have been calculated numerically to test the correlation between ejecta emplacement and linear structures on the surface (Schmedemann et al., 2017).

The purpose of this study is to provide an overview about the ballistic emplacement of ejecta on Ceres, especially for smaller boulder craters. The criteria for the selected twelve boulder craters are the number of boulders, boulder diameters and the crater location. Selected craters must have

enough identifiable boulders at a given resolution. Only six craters have enough large blocks that allow size measurements in a sufficient large diameter range. Additional craters were selected to cover all occurring boulder crater diameters and latitudes. At first, we mapped and, if possible, measured boulders of selected craters to analyze their distribution. Initially, we focused on the emplacement of all ejected particles. How do rotation and gravitational acceleration affect ejecta transport of craters in the diameter range of boulder craters? Subsequently, we wanted to know at which velocities boulders were ejected and how their trajectories were influenced by rotation. In addition, we investigate how the choice of impactor parameters alters resulting ejection velocities. We chose a fast and easy implemented analytical approach to calculate re-impact sites introduced by Dobrovolskis (1981).

5.2 METHODS

5.2.1 MEASUREMENT AND ANALYSIS OF BOULDER AND CRATER DIAMETERS

Boulder locations, boulder diameters and the diameters of unnamed craters were measured using the ArcGIS Add-In CraterTools (Kneissl et al., 2011), which allows the determination of diameters of circular features independent of image and data frame map projections. Measurements were conducted on mosaics based on data from Dawn's Low-Altitude-Mapping Orbit (LAMO) with a resolution of 35 m/pixel (Roatsch et al., 2016a). Because of the non-circular outline of boulder craters, several circles were fitted to each crater to find average values for diameter and location of unnamed craters. Like boulder craters, boulders are of irregular shape and therefore the longest observable elongation of a block was used to define its diameter. Boulders larger than ~100 m could be distinguished morphologically. Close to the resolution limit, positive and negative topographic features can only be identified by the direction of the shadows they cast. We estimate the error for size measurements to be up to one pixel, which correspondents to 35 m. The separation of single boulders was additionally complicated by dense clustered blocks. In consequence, we decided that only measurements above ~100 m object size are reliable and were therefore used for interpretation. In addition, we identify the largest boulders for 30 craters on Ceres to compare the relation between the maximum block size and the crater diameter.

To analyze the linear relation between block distances and block diameters, we calculated the correlation coefficient, using the Scipy statistics package (Oliphant, 2007). The correlating coefficient coeff is defined as $\text{coeff} = \sum xy / \sqrt{\sum x^2 \sum y^2}$, with $x = x_i - \bar{x}$ and $y = y_i - \bar{y}$, in which $\bar{x}$ and $\bar{y}$ are the mean values (e.g. Bewick et al., 2003). Coefficients close to ± 1 indicate a strong positive

or negative linear relationship. Coefficients close to 0 indicates no linear relationship (e.g. Vothihong et al., 2017). We decided not to derive p-values for a null hypothesis test that is used to test the significance of the correlation, because a larger number of data points is recommended.

5.2.2 SIZE-FREQUENCY DISTRIBUTIONS

Rock fragmentation has been shown to follow a power-law behavior (Hartmann, 1969). Power-law distributions are widely used to describe boulder distributions (e.g. DeSouza et al., 2015; Li et al., 2017; Michikami et al., 2008) and were therefore fitted to our diameter data sets. To fit the distribution, estimating uncertainties and plot results, we use a Matlab implementation of the statistical methods described in Clauset et al. (2009). Closely following their description, a data series follows a power-law distribution, if it satisfies the probability distribution $p(x) \propto x^{-\alpha}$, where α is the exponent or scaling factor. We have a continuous data set, whose complementary cumulative distribution function (CCDF) P(x) is defined by Eq. (5-1).

$$P(x) = \int_x^{\infty} p(x')dx' = \left(\frac{x}{x_{min}}\right)^{-1+\alpha} \tag{5-1}$$

The lower bound of the power-law behavior is described by x_{min}. Maximum likelihood estimators are used to fit the power-law distribution to the data set. The lower cutoff of the scaling region is estimated with the goodness-of-fit method, based on Kolmogorov-Smirnov statistics. Uncertainties for the constants x_{min} and α are calculated as well.

Goodness-of-fit tests provide so-called p-values (not the same p-value as in statistical hypothesis testing in section 5.2.1), which describe whether the hypothesis of a power-law distribution is suitable. For this purpose, the "distance" between the data and the model is calculated. That deviation is compared to distances of synthetic data sets. The p-value is the fraction of synthetic data sets that has a larger distance than the empirical ones. It takes values between 0 and 1. Values close to 1 indicate that the model is a good fit for the data. Discrepancies arise from statistical fluctuations. A rule-of-thumb threshold for a good fit is 0.1. Values below that threshold indicate that the power-law distribution is not a good fit for the data. If the number of samples is low, the test is not reliable. To rule out power-law behavior, a large number (~>100) of samples is needed for the p-value to fall off below the threshold.

Sometimes, rock fragmentation is also described by the Weibull distribution (stretched exponential) (Weibull, 1951). It is used, for instance, to describe the size distribution of volcanic

ashes (e.g. Gouhier and Donnadieu, 2008). Because of its characteristic rollover at smaller sizes it can be well suited to describe the size-frequency distribution of secondary craters (Ivanov, 2006; Werner et al., 2009) and can therefore be applicable for ejecta blocks as well. We focus on power-law fits because they are more commonly used to describe the size distribution of ejecta blocks and therefore make our results comparable. Nevertheless, we tested whether a stretched exponential distribution would be a better fit for our data with a likelihood ratio test (Clauset et al., 2009). We used the implementation by Alstott et al. (2014). If that ratio is sufficiently positive, the first distribution is considered to be the better fit, if negative the second one. Another p-value is introduced to describe the significance of such ratios. The chosen threshold for the second p-value is 0.1. For values above the threshold, no statement about a favored model can be made.

5.2.3 SCALING LAWS

Impact crater scaling laws defined by theory and laboratory experiments describe the relationship between impactor, target and the resulting impact crater (Werner and Ivanov, 2015). For a detailed derivation analysis, we refer to Ivanov (2001) and Werner and Ivanov (2015). The transient crater diameter is the diameter of the initial cavity before crater modification sets in (Melosh and Ivanov, 1999). The transient crater diameter for complex craters is defined as $D_t=D_{sc}^{0.15} D^{0.85}$ (Croft, 1985) and for simple craters as $D_t \approx D/1.25$ (Werner and Ivanov, 2015). D is the crater diameter and D_{sc} is the simple-to-complex transition diameter. On Ceres, Hiesinger et al. (2016) calculated a simple-to-complex transition diameter of 10.3 km. Holsapple (1993) distinguishes between strength and gravity regime. The choice of regime depends on the size of the impactor. The strength regime applies to smaller projectiles and is used if the crustal strength of the target is large compared to the lithostatic pressure. On the contrary, the surface gravity dominates in the gravity regime. Schmidt and Housen (1987) define a scaling law, which describes the relationship between projectile size and the transient crater diameter. The scaling law uses the π-theorem (Buckingham, 1914), which puts parameters in dimensionless groups ("pi-groups") (Dowling and Dowling, 2013). Schmidt and Housen (1987) distinguish between two target scenarios: nonporous, zero friction rocks and dry friction material, such as sand. The relation between projectile diameter D_p and crater size for nonporous, zero friction rocks in Eq. (5-2) incorporates the strength-to-gravity transition (Ivanov, 2008; Neukum and Ivanov, 1994; Schmidt and Housen, 1987).

$$D_p = D_t \cdot \frac{\left(g\, D_t + D_{sg}\right)^{0.282}}{\left\{1.16 \left(\frac{\delta}{\sigma}\right)^{\frac{1}{3}} (v_p \sin\alpha)^{0.44}\, g^{-0.22}\right\}^{\frac{1}{0.78}}} \tag{5-2}$$

Parameters that are incorporated in the projectile diameter equation are the strength-to-gravity transition diameter D_{sg}=1.75 km (Hiesinger et al., 2016), the density of the projectile δ, the density of the target σ, the projectile velocity v_p and the impact angle of the projectile α. Housen et al. (1983) introduced scaling laws for the ejection velocity of a particle v(x) as a function of its distance x to the crater center. Richardson et al. (2005) adapted that equation for a gravity-dominated regime by allowing the velocity to drop to zero at the crater rim (equation (5-3)).

$$v(x) = \frac{2\sqrt{gR_t}}{(1+e_x)} \left(\frac{x}{R_t}\right)^{-e_x} - \frac{2\sqrt{gR_t}}{(1+e_x)} \left(\frac{x}{R_t}\right)^{\lambda} \tag{5-3}$$

R_t is the transient crater radius and e_x and λ are constants. The constant e_x is a material parameter and π-scaling results range from 1.8 for competent rock and 2.6 for quartz sand (Melosh, 1989). Housen et al. (1983) found a value of 2.44 of e_x for impacts into Ottawa sand. The value of λ is to be chosen between 6 and 10 (Richardson et al., 2005). Based on experimental (e.g. Anderson et al., 2003; Anderson et al., 2004; Cintala et al., 1999; Schultz et al., 2005.) and numerical studies (Collins and Wünnemann, 2007), after Richardson et al. (2007) in first-order approximation, the ejection angle φ with respect to the local surface horizontal is decreasing linearly with distance x from the impact center: $\varphi = \varphi_0 - \varphi_d(\frac{x}{R_t})$. Following experimental results by Cintala et al. (1999), we use a starting angle φ_0=52° and a dropping angle φ_d=18°. An oblique impact, with an impact angle $\alpha < 90°$ with the respect to the surface horizontal, leads to decreasing ejection angles and increasing ejection velocities on the downrange side, which is defined as the opposite direction to the incoming projectile. The final ejection angle φ_L is given by Eq. (5-4).

$$\varphi_L = \varphi - [30° \, (\cos\alpha) \left(\frac{1 - \cos\theta}{2}\right) \left(1 - \frac{x}{R_t}\right)^2] \tag{5-4}$$

The particle's azimuth is θ. The resulting ejection velocity v_L is given in Eq. (5-5).

$$v_L = \left[(v \sin\varphi)^2 + \left(v \frac{\sin\varphi}{\tan\varphi_L} \right)^2 \right]^{\frac{1}{2}} \quad (5\text{-}5)$$

Oblique impacts are common; 45° is the most likely impact angle (Shoemaker, 1962), and is therefore used as a default value. Other default values (Table 5-1) are an impact velocity of 4.79 km/s, which is the average impact velocity for Ceres (O'Brien and Sykes, 2011), a target density of 1815 km/m^3, which is in the range reported in Park et al. (2016) and an impactor density of dense rock (3000 kg/m^3) (Collins et al., 2005). North (azimuth $\theta = 0°$) was chosen as the default incoming direction of the impact. We use the value e_x=2.44 derived for impacts into Ottawa sand by Housen et al. (1983), and the material constant λ=10 according to Bart and Melosh (2010b) for a lunar setting, in the absence of better constrained material constants for Ceres.

We vary not well-constrained input parameters, such as the incoming direction, impacting angle and velocity of the projectile, the material constants e_x and λ and the densities of target and projectile to test their effect on resulting re-impact sites and velocities. In addition to the default incoming direction, projectiles impacting from south and west are tested as well as a low impact angle of 10° and a vertical impact of 90°. The average impact velocity is 4.79 km/s, but a majority of impacts have velocities below or above and only a small fraction of all impacts in the main belt and on Ceres show velocities above 8 km/s (O'Brien and Sykes, 2011). We test a low (2 km/s) and a high (8 km/s) impact velocity, related to impact probabilities on Ceres. We test different projectile materials, such as ice (1000 kg/m^3), porous rock (1500 kg/m^3) and iron (8000 kg/m^3) (Collins et al., 2005). In addition, we vary the target density by applying the lower (1680 kg/m^3) and upper bounds (1950 kg/m^3) for the density of Ceres' outer shell (Park et al., 2016).

5.2.4 Elliptical Trajectories

We calculated elliptical orbits using fundamental equations for ballistic trajectories described in detail in Morris (1964). The ejection velocity of an elliptical orbit is based on three equations: the conservation of angular momentum $rv\cos(\vartheta) = \sqrt{\mu p}$ = const., where r is the magnitude of the radius vector from the center of the planetary body, v the velocity, ϑ the flight-path angle, μ the product of the gravitational acceleration, and square of the body's radius and p the semilatus rectum. Secondly, the conservation of energy in terms of the vis-viva equation $v^2 = \mu \left(2/r - 1/a\right)$, with a as the semimajor axis of the elliptical orbit. Thirdly, the equation of the ellipse $1/r = (1 + \varepsilon \cos(\upsilon))/p$, where ε is the eccentricity and ν the true anomaly. The final range as a function of the ejection velocity is described in Eq. (5-6). It is the result of subtracting the

true anomaly at the launch from the true anomaly at the terminal, where φ_L is the launch angle, v_L the launch velocity, and $\Delta\phi = f/R_P$ the ratio between the projected range on the surface of the body f and the planet radius R_P.

$$\Delta\phi = 2\text{acos}\left(\frac{1-v_L^2\cos^2(\varphi_L)}{\varepsilon}\right) = 2\,\text{atan}\left(\frac{v_L^2\sin(\varphi_L)\cos(\varphi_L)}{1-v_L^2\cos^2(\varphi_L)}\right) \quad (5\text{-}6)$$

5.2.5 Global and Local Re-impact Regime on a Rotating Body

The Coriolis effect acts on particles that move relative to the rotating planetary body. It has a horizontal and a vertical component with respect to the planetary surface. The vertical component leads to a westward deflection of particles ejected upward. That westward deflection is at its maximum at the equator and zero at the poles. Horizontal moving particles in the northern hemisphere are deflected to the right of their original direction of motion. Due to the clockwise rotation, eastward moving particles are deflected towards the equator and westward moving particles to the poles. In the southern hemisphere, the effect of the horizontal component deflects particles to the left of their path. This effect also is latitude-dependent, finds its maximum at the poles and is not existent at the equator (e.g. Chow, 2013). We determine global re-impact sites of ejecta particles according to their ejection velocity on a rotating sphere by following an analytical approach described in Dobrovolskis (1981). For a detailed description of all calculations, we refer to the original publication. Calculations are based on the assumption of a spherical symmetric rigid body. The assumption is feasible for Ceres, since its shape is nearly spheroidal (Park et al., 2016). Atmospheric influences are neglected. Dimensionless units are used to simplify calculations. To describe the ballistic emplacement of a point mass relative to the rotating system, the eastward rotational velocity of Ceres is added to the particle's launch velocity. Ceres' dimensionless eastward angular velocity $\omega = 0.247$ at the time of the launch given by $\omega = 3.3\ \text{hr}/\sqrt{\varrho}\text{P}$, with an orbital period of P=9.074 h (Thomas et al., 2005) a bulk density of $\varrho = 2.162\ \text{kg/m}^3$ (Park et al., 2016). In addition, we use a mean radius R=476 km and a gravitational acceleration of $g = 0.28\ \text{m/s}^2$ (Thomas et al., 2005). The rotational component that is added to the eastward component of the particle's inertial velocity is then a product of the angular velocity and the sine of the start colatitude of the particle. We distributed ejection sites of test particles in a ring on a sphere. The ring resembles the area between the test crater's projectile radius and the transient crater radius.

Table 5-1. Default input parameters

Parameter	Value
Impact angle α	45°
Incoming impact direction θ	0° N
Ejecion angle φ_L	45°
Projectile density δ	3000 kg/m^3
Projectile Velocity v_P	4.79 km/s
Target density σ	1815 kg/m^3
e_x	2.44
λ	10

To relate ejection velocities to specific boulder locations, incorporating the planet's rapid rotation, we used the Octave (Eaton et al., 2015) implementation of the Delaunay triangulation (Barber et al., 1996) to find the analytically calculated particle landing sites that are closest to the mapped boulder locations.

We think that due to the craters' richness in mass wasting features, it is unlikely that boulders inside the craters today are located where they were first deposited. Instead, the majority probably was moved by landslides and other processes of crater collapse. Therefore, we only use boulders outside the crater rim for velocity analyses.

5.3 RESULTS

5.3.1 CRATER MORPHOLOGY AND BOULDER DISTRIBUTION

We morphologically analyze twelve selected craters between 7.8 and 31 km with large ejecta blocks, which provide a selection of boulder crater latitudes and crater diameters (Fig. 5-1). Coordinates and diameters are listed in Table 5-2. The projectile sizes calculated with Eq. (5-2) are listed in Table 5-3. Size measurements are performed for six craters that have enough large ejecta blocks.

Most of the analyzed craters are located on Ceres' southern hemisphere. All craters feature a continuous ejecta layer and display multiple mass wasting features. Some craters exhibit shadowed areas due to poor illumination conditions during data acquisition, while others have permanently shadowed regions (Schorghofer et al., 2016); hence, not all interior structures are visible. Most of the investigated craters do not fit easily in the simple or complex crater scheme. Platz et al. (2016a) distinguish between simple, modified simple, transitional complex and complex craters on Ceres. Thrud (7.8 km) is a perfectly simple bowl-shaped crater with a circular rim and steep crater walls. The rim of Crater B (9.6 km) is also nearly circular, but the crater floor is flatter than the crater floor of Thrud. The craters Oxo, Braciaca, Juling, Cacaguat, Crater A, Crater C and Crater D are characterized as transitional complex craters. They have scalloped rims and flat floors. Those craters are also characterized by lobate deposits in their interior. Such deposits can cover possible interior features. Oxo crater (10 km) has only one large terrace. Crater D is shallow with a flat floor and a central ridge, which might not be due to central uplift but to the encounter of two landslides that piled up in the middle of the crater. Nunghui (22 km) shows all characteristics of a complex crater, such as a central peak, a scalloped rim, a flat floor and multiple terraces. Other complex craters are Ratumaibulu and Jacheongbi. They exhibit flat floors with central mounds and scalloped crater rims.

We observe boulders inside and outside of nearly 60 craters. Some display hundreds, whereas others have only a few ejecta blocks. Boulders outside craters are usually distributed in all directions within two crater radii. Particularly asymmetrical boulder distributions are found around Crater A, Juling and Oxo. The deposition of large ejecta blocks often occurs in clusters and linear arranged groups. In total, we map between 9 boulders outside the crater rim of Oxo and 389 at Jacheongbi, which also has the largest block with 394 ± 35 m. Fig. 5-2 illustrates some examples of large ejecta blocks.

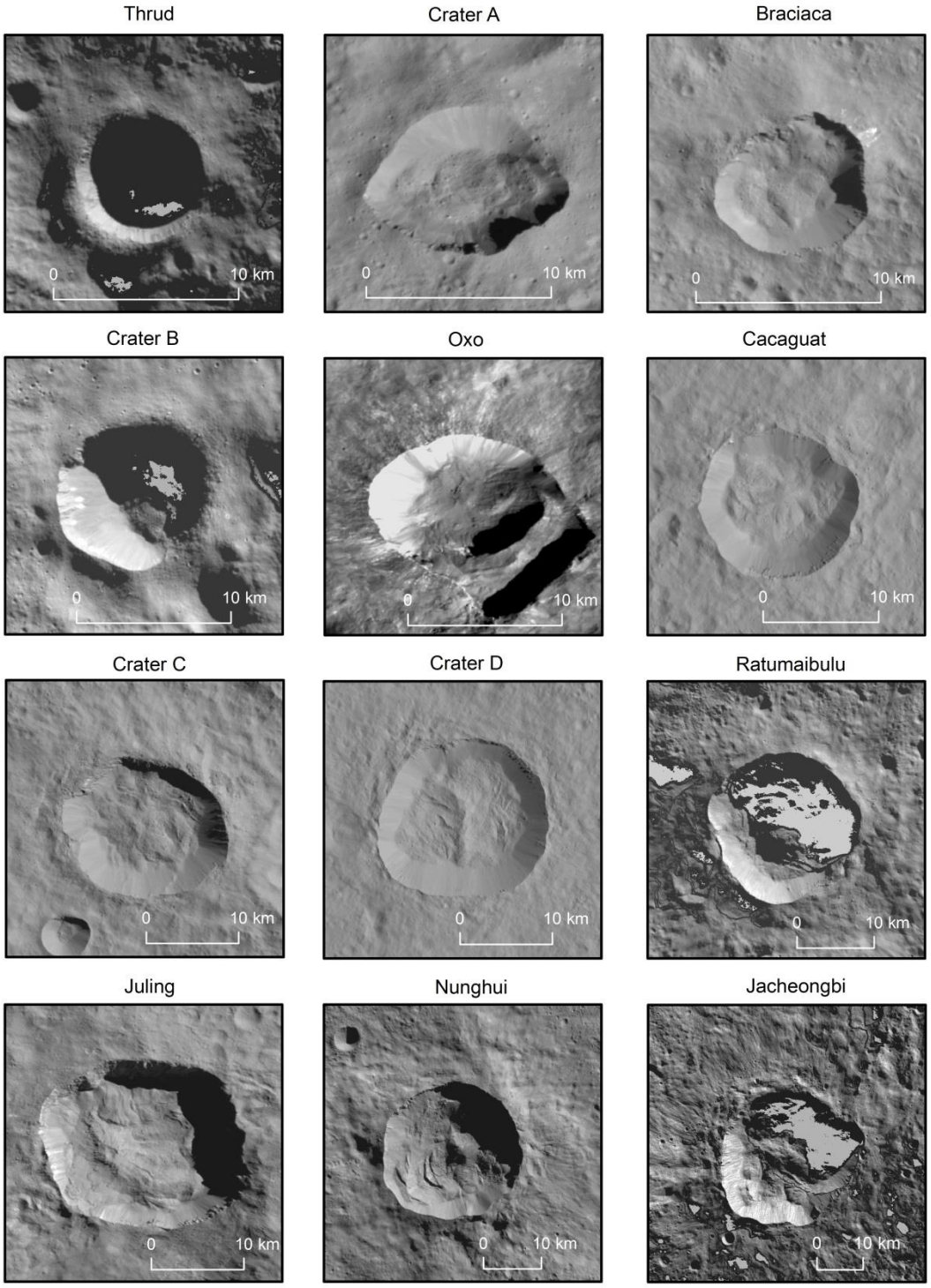

Fig. 5-1. Twelve boulder craters on Ceres, ordered by size displayed as LAMO clear-filter mosaics (35 m/pixel) in equidistant (Crater A, Braciaca, Oxo, Cacaguat, Crater C, Crater D and Juling) and stereographic projection (Thrud, Crater B, Ratumaibulu, Nunghui, Jacheongbi). No data values are displayed in a 30% gray. Coordinates and diameters are listed in Table 5-2.

Table 5-2. Coordinates and crater diameters of investigated boulder craters

Crater	Longitude [°]	Latitude [°]	Diameter [km]
Thrud	31	-71.3	7.8
Crater A	-4.3	33.9	7.8
Braciaca	84.4	-22.8	8
Crater B	-115.2	-67.2	9.6
Oxo	-0.4	42.2	10
Cacaguat	143.6	-1.2	13.6
Crater C	-80.9	-23	15.6
Crater D	21.1	-10	18.1
Ratumaibulu	77.5	-67.3	20
Juling	168.5	-35.9	20
Nunghui	-87.7	-54	22
Jacheongbi	2.3	-69.2	31

Table 5-3. Projectile diameters of investigated boulder craters

Crater	Projectile Diameter [km]
Thrud	0.4
Crater A	0.4
Braciaca	0.4
Crater B	0.5
Oxo	0.5
Cacaguat	0.9
Crater C	1.1
Crater D	1.3
Ratumaibulu	1.4
Juling	1.4
Nunghui	1.6
Jacheongbi	2.2

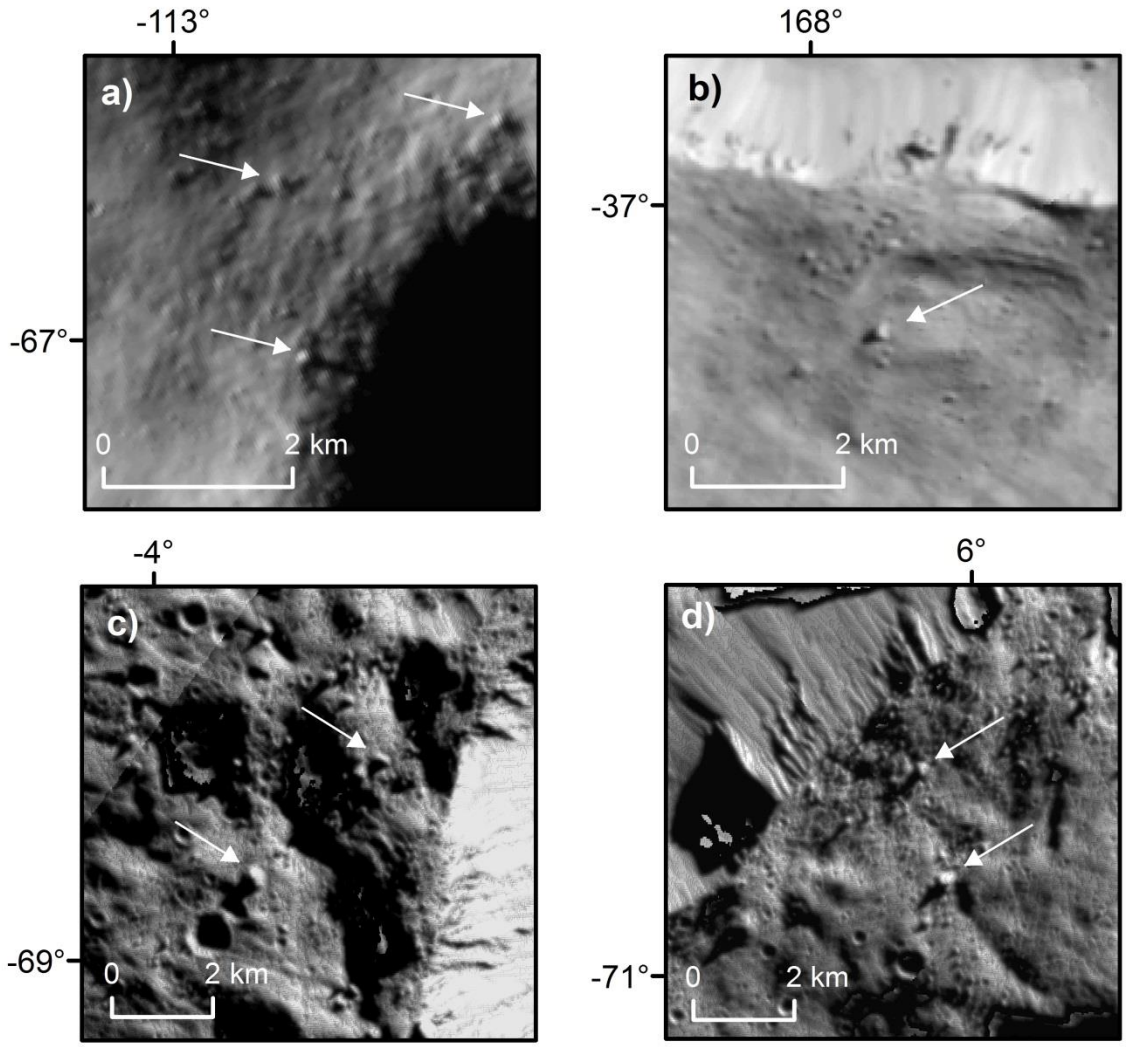

Fig. 5-2. Close-up view of boulders outside the crater rim of Crater B (a), Juling (b), and Jacheongbi (c, d). Note that there are some image artifacts close to the crater rim. White arrows mark selected example blocks.

In Fig. 5-3 and Fig. 5-4, we analyzed the relation between a boulder's diameter and its distance from the crater rim. Correlation coefficients for both single crater's diameters and boulder sizes outside the crater rim and for diameters and sizes of all measurements combined are below $< \pm 0.3$ (Table 5-4), which means that there is no, or just a very weak, linear relationship. Boulders with diameters below 200 m can be found at any range from the crater center. A few large examples, especially for Jacheongbi, seem to be restricted to the area close to the crater rim. The gap between ~0.7 and 0.9 crater radii for all craters is explained by the crater walls that lie within this range. Those crater walls are characterized by steep slopes and there are not many boulders deposited directly on them. There are, however, boulders sliding down the walls. Their tracks are clearly visible. Those blocks are not included in our analysis, because their location

clearly changed after their first deposition. A comparison of crater diameters and the diameter of their largest (Fig. 5-5), with a correlation coefficient of 0.68 suggests a strong (Evans, 1996) positive linear correlation between these two observations.

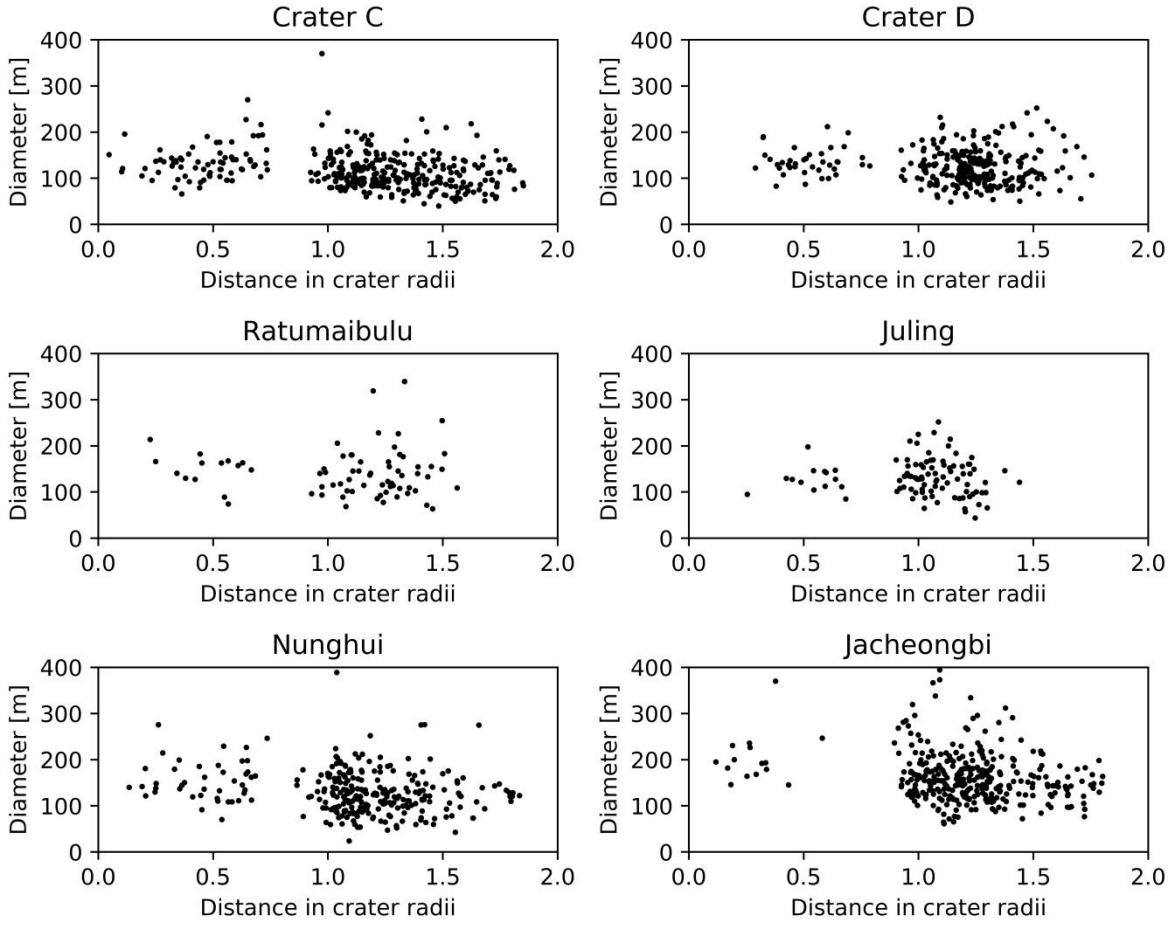

Fig. 5-3. Diameter measurements of ejecta blocks inside and outside six craters as a function of their distances to the crater center in radii of their parent crater

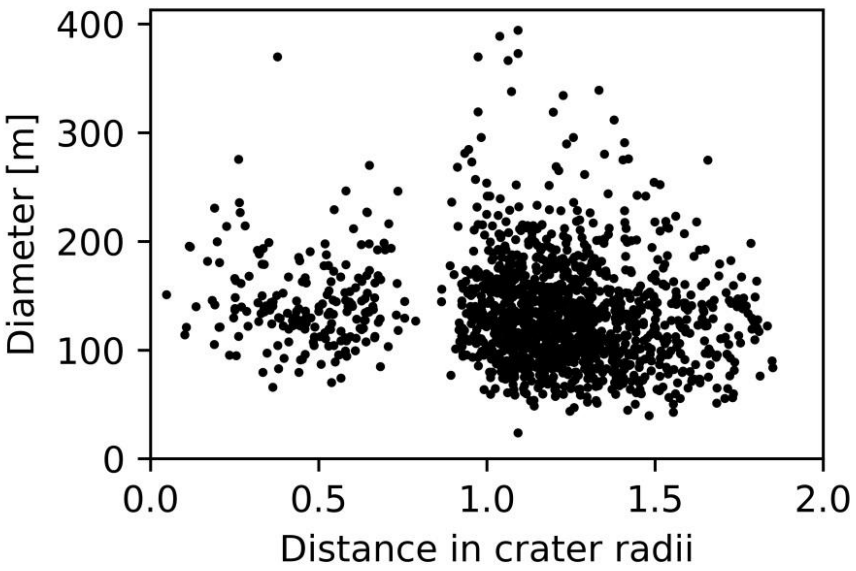

Fig. 5-4. Boulder diameters as a function of their distances to the crater center in radii of their parent crater of ejecta blocks inside and outside of six craters combined

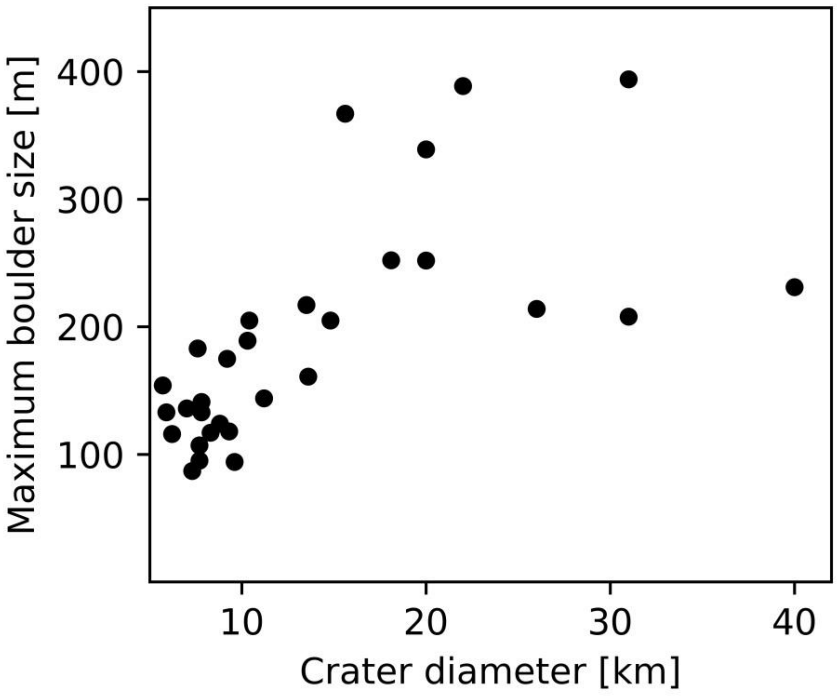

Fig. 5-5. Diameters of the largest boulders of 30 craters as a function of the crater diameter

Table 5-4. Correlation coefficients evaluate the linear correlation between boulder size and its distance to the crater rim.

Crater	Correlation Coefficient
Crater C	-0.21
Crater D	0.01
Ratumaibulu	0.11
Juling	-0.21
Nunghui	-0.06
Jacheongbi	-0.19
All	0.23

5.3.2 BOULDER SIZE DISTRIBUTION

We fit and evaluate power-laws of six cumulative boulder diameter distributions. The goodness-of-fit results, described by the p-value, are presented in Table 5-5. The smallest diameter that is used for the fit is represented by the value of x_{min}. Those diameters lie between 127 and 167 m. Those values agree with our observation that small diameter ranges suffer from greater measurement errors and are more incomplete than larger diameter ranges. By excluding small diameters, the total amount of blocks that are used for fitting is reduced. Only Crater C, Crater D and Jacheongbi have more than 100 used boulders. The p-values for Crater C and Crater D fall under the threshold of 0.1; hence, the power-law does not sufficiently describe their cumulative diameter distribution. Four craters: Ratumaibulu, Juling, Nunghui and Jacheongbi have p-values that are larger than the threshold of 0.1. However, for the analysis of the first three craters, the number of data points is very small. Therefore, the goodness-of-fit test is not reliable, since the p-value might fall off if more measurements were available. We report the results of power-law fitting for those examples, with the chance that power-law fits are not best suited. The slopes of the power-law fits, as shown in Fig. 5-6, lie between -4.4 ± 0.7 and -6.2 ± 1.5.

The likelihood ratio tests (Table 5-6) that compare the power-law fit with a stretched exponential fit show that neither distribution is the significantly better fit because the p-values are always above the threshold for all six craters. That is why we cannot rule out either of the proposed fragmentation process behaviors. Note that this might only be true for the present data set where small diameters are missing because of the limit of resolution.

Table 5-5. Parameters for power-law fits of six craters. The goodness-of-fit test is described by the p-value with a threshold of at least 0.1 for a fit of sufficient quality. The test depends on a sample size that is large enough (~>100). The boldface marks the p-value that is above the threshold while using a large sample size. Ratumaibulu, Juling and Nunghui also have p-values above the threshold, but the number of data points is too low to evaluate the fit (in brackets). The minimum diameter that follows such a distribution is x_{min} and α the exponent of the power-law decay. The slope of the power-law fit is listed along with the number of used data points.

Crater	P-value	Alpha	Slope/Exponent (1 – alpha)	x_{min}	Blocks Mapped	Blocks used for Fitting
Crater C	0.008	6.1 ± 0.8	-5.1 ± 0.8	127.0 ± 13	353	120
Crater D	0.097	6.5 ± 1.4	- 5.5 ± 1.4	134.8 ± 11.7	284	104
Ratumaibulu	(0.316)	5.6 ± 1.4	-4.6 ± 1.4	139.9 ± 14.6	71	36
Juling	(0.363)	6.7 ± 1.8	-5.7 ± 1.8	144.3 ± 14.5	96	34
Nunghui	(0.893)	7.2 ± 1.5	-6.2 ± 1.5	166.8 ± 21.9	282	58
Jacheongbi	**0.35**	5.4 ± 0.7	-4.4 ± 0.7	162.6 ± 16.7	336	147

Table 5-6. The power-law distribution is compared to a stretched exponential distribution. A sufficient positive or negative likelihood-ratio (LR) would make one or the other distribution a better fit. A p-value in the column next to the LR describes the significance of the latter. The threshold is chosen to be 0.1. Larger values indicate that no model is favored.

Crater	LR	P-value
Crater C	-0.62	0.55
Crater D	-2.66	0.14
Ratumaibulu	0.10	0.65
Juling	-0.53	0.49
Nunghui	0.16	0.65
Jacheongbi	-1.22	0.30

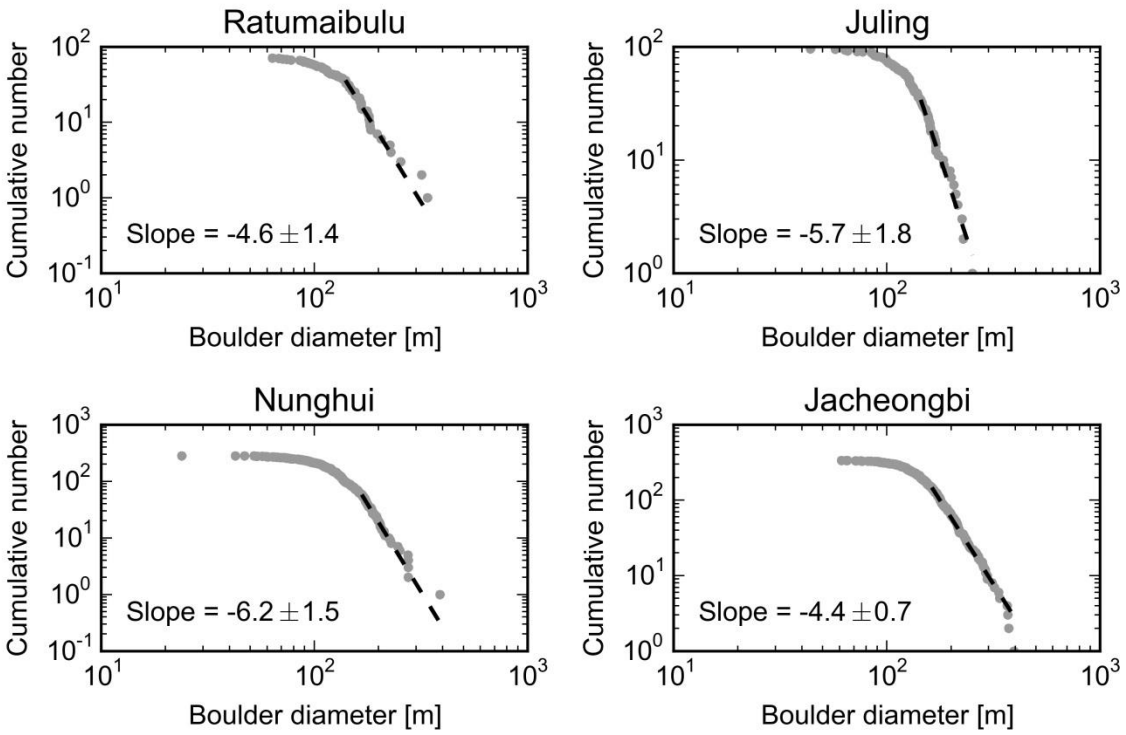

Fig. 5-6. Cumulative distribution of boulder diameters and slopes/exponents of power-law fits for four craters

5.3.3 GLOBAL VELOCITY AND RE-IMPACT SCHEME

Figure 5-7 and Figure 5-8 illustrate particle landing sites as a function of ejection velocities in different projections. Our analytical model predicts that high-speed ejecta can travel large distances while it is highly influenced by the rotation of Ceres. The particle distraction due to rotation effect is strongly latitude-dependent. High-velocity particles string out along nearly latitude parallel lines (Fig. 5-7). Figure 5-8 illustrates landing locations as a function of particle ejection velocity on maps that are centered on the pole of the crater's opposite hemisphere.We see that for craters at higher latitudes, such as Thrud (-71°), Crater B (-67.2°), Ratumaibulu (-67.3°), Nunghui (-54) and Jacheogbi (-69.2), fast particles accumulate near the pole of the opposite hemisphere. On the other hand, craters closer to the equator, such as Cacaguat (-1.2°) and Crater D (-10°) have high-velocity particles that accumulate around the equator (Fig. 5-7). Furthermore, large fractions of the ejecta of craters in the equatorial region, such as Cacaguat, are deposited more or less symmetrically to the equator. Impact locations of particles with different ejection velocities overlap. In a non-rotating setting, particles are deposited radially in a range that correlates with their velocities, so, close to the crater there is a circle of low-velocity particles and so forth. In a rotating setting however, particles with different ejection velocities can re-impact within the same distance to their primary crater. Figure 5-7 shows that particles approximately up

to 0.3 km/s are still deposited radially to the crater. Then we observe areas where trajectories are bent, so that the particles change their direction of motion. In consequence, re-impact locations of high-velocity particles interact with re-impact locations of particles with lower ejection velocities.

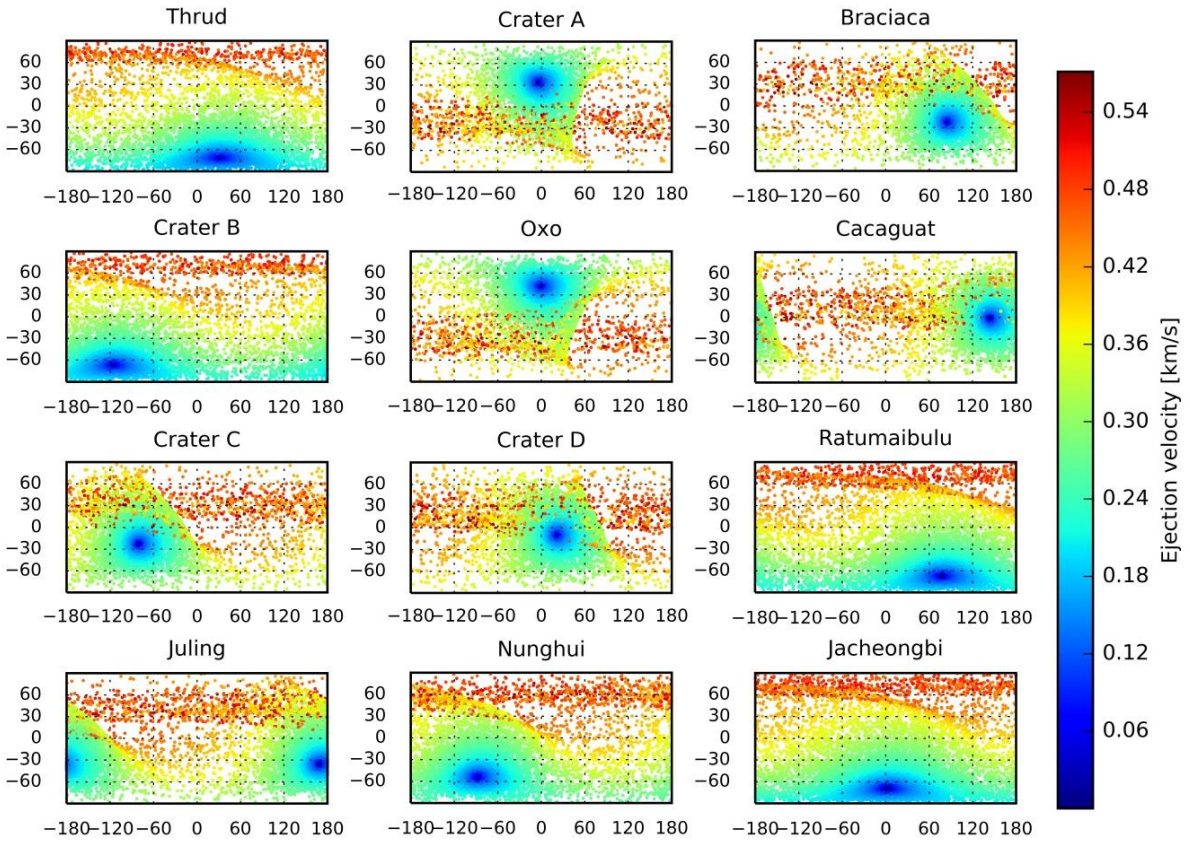

Fig. 5-7. Particle re-impact sites as a function of their ejection velocity. Maps are displayed in equirectangular projection. Note that particles might be faster than the escape velocity because the shown velocity is the velocity relative to the rotating body.

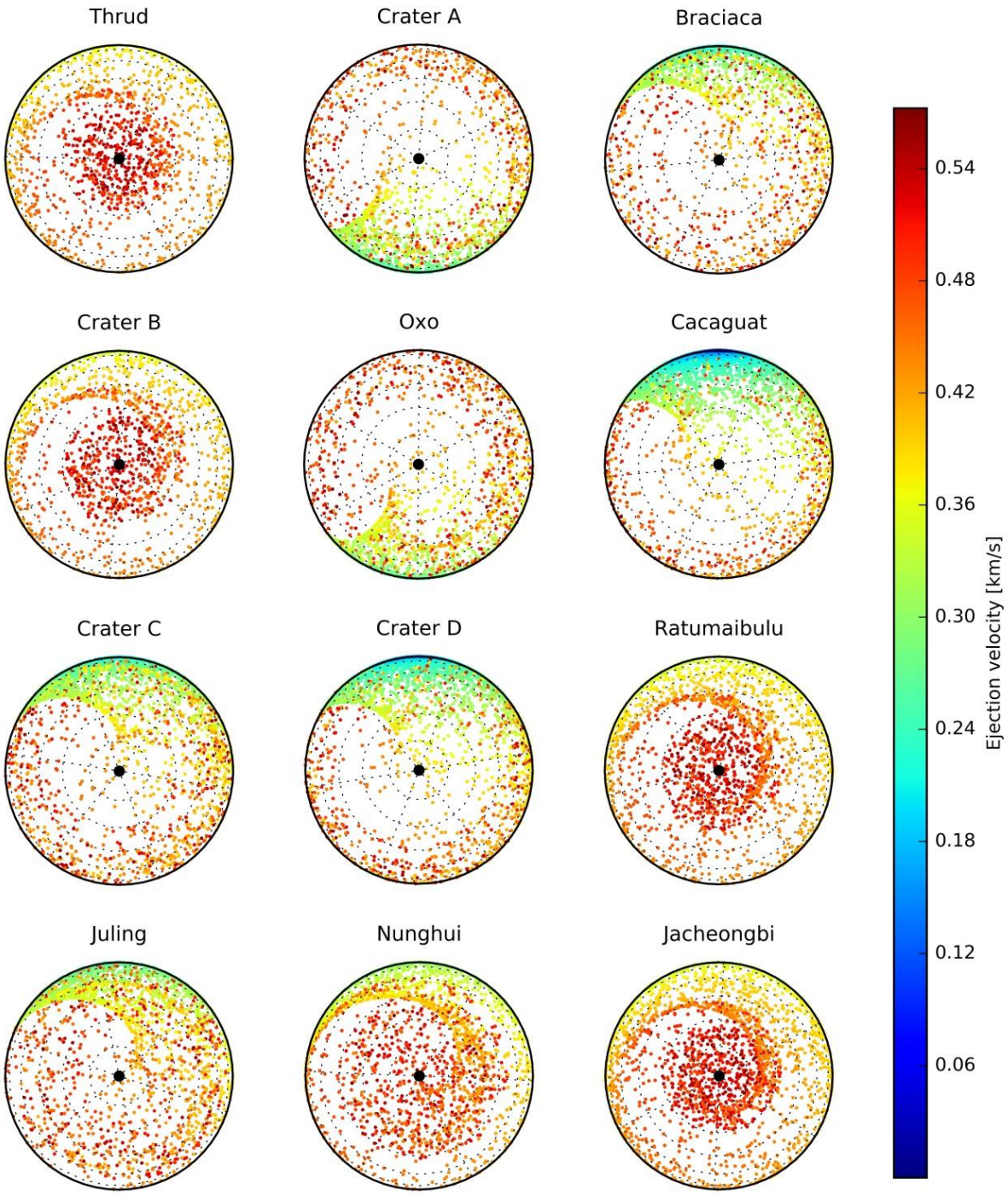

Fig. 5-8. Global re-impact pattern as a function of the particles' ejection velocity. The maps are in orthographic projection, centered at the pole of the crater's opposite hemisphere. The pole is marked by a black dot. Note that particles might be faster than the escape velocity because the shown velocity is the velocity relative to the rotating body.

5.3.4 The Effect of Input Parameters on the Global Velocity and Re-impact Scheme

Impact conditions are, to some extent, unknown and cannot be specified by the crater's morphology. We tested the effect of input parameters on the resulting velocities and patterns as illustrated in Fig. 5-9. For the variation of parameters, we chose Crater D, because parameter variation can be illustrated best at an equatorial crater. For studying the local velocity regime, it is well-suited because of its fairly large size and the many identified boulder locations.

The largest visible alteration of re-impact sites is produced by both the direction and the impact angle of the projectile. A change in the projectile's incoming direction causes large alterations in the re-impact regime (Fig. 5-9a-c). The impact angle changes the turnover point where particles start moving from east to west (Fig. 5-9d, e). Figure 5-9a-d also illustrates the asymmetry in deposition that is caused by an oblique impact. In comparison with a vertical impact, as illustrated in Fig. 5-9e, high-velocity particles of an oblique impact (Fig. 5-9a-d) are distributed less symmetrically around the equator. For a 10° impact (Fig. 5-9d), for instance, particles change their direction of motion from east to west at different longitudes north and south of the equator. The calculation of the projectile radius and consequently start locations and velocities depend on the impactor velocity, target and projectile density. Compared to the impact geometry, the effect of material parameters and velocities on ejecta trajectories is less significant (Fig. 5-9f-l). On account of this, varying input parameters always influences the particles' trajectories, but the only major effects are caused by impact angle and direction.

Eq. (5-3) describes the ejection velocity as a function of the distance to the crater center. The constants e_x and λ resemble material properties, but literature provides only a limited number of material possibilities and constraints for planetary bodies. We calculated ejection velocities of Crater D with varying constants. Particles are ejected between projectile radius and transient crater radius. By varying the constant e_x by $\pm$ 10%, based on our default value of sand (Housen et al., 1983), we find that velocities increase with increasing e_x (Fig. 5-10). The effect is smaller below the escape velocity (Fig. 5-10 inset) and negligible for velocities below 100 m/s. We also varied λ between 6 and 10, but that choice does not affect the resulting velocities in any significant way.

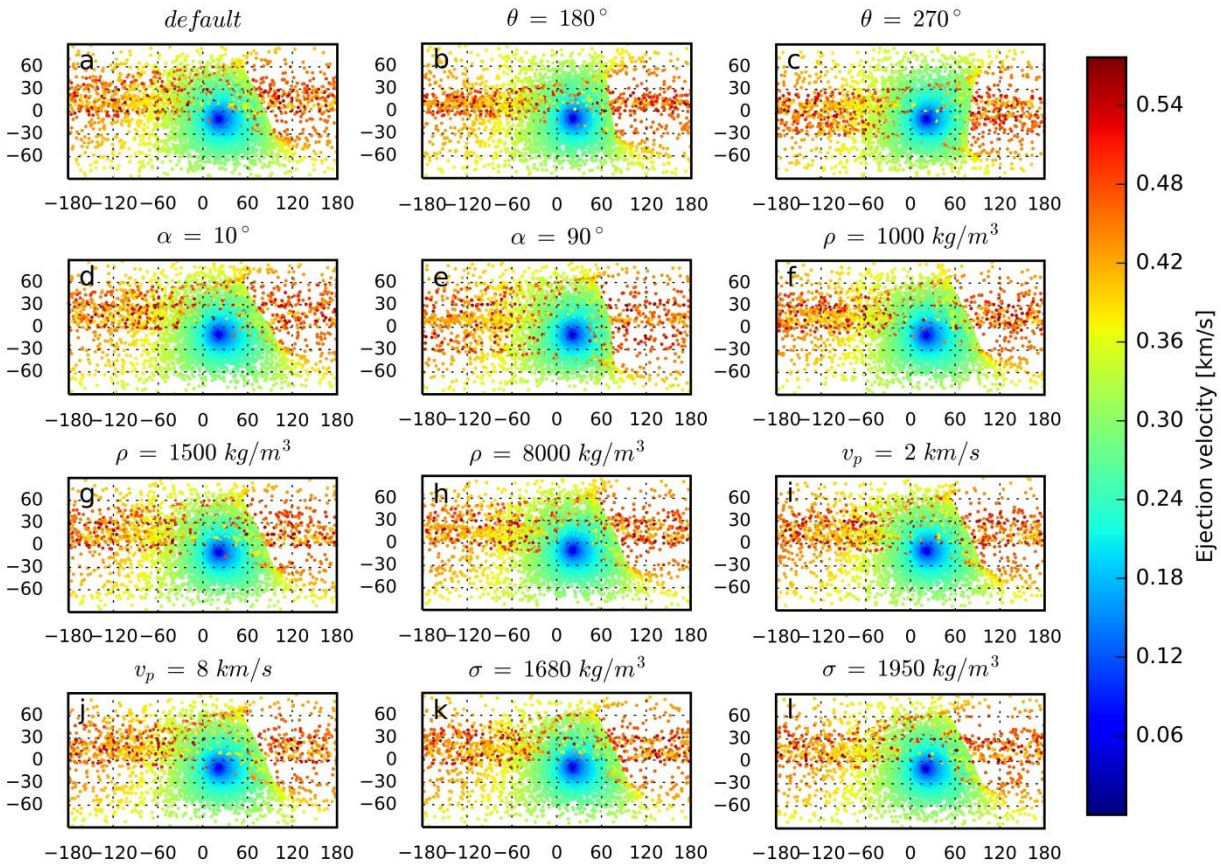

Fig. 5-9. Testing the effect of different input parameters on Crater D. a) An impact with the default values of a 45° impact angle with a projectile from the north (0° azimuth), an impact velocity of 4.79 km/s, a target density of 1815 kg/m3 and an impactor density of dense rock (3000 kg/m3). b) An impact with the incoming azimuth of 180° (south). c) An impact with the incoming azimuth of 270° (west). d) The projectile impacts with an angle of 10° with respect to the surface. e) The projectile impacts with an angle of 90° (vertical impact). f), g) and h) Different impactor materials: ice (1000 kg/m3), porous rock (1500 kg/m3) and iron (8000 kg/m3). i) and j) Projectile velocities of 2 km/s and 8 km/s. k) and l) Lowest and highest densities of Ceres outer layer (Park et al., 2016). Note that particles might be faster than the escape velocity because the shown velocity is the velocity relative to the rotating body.

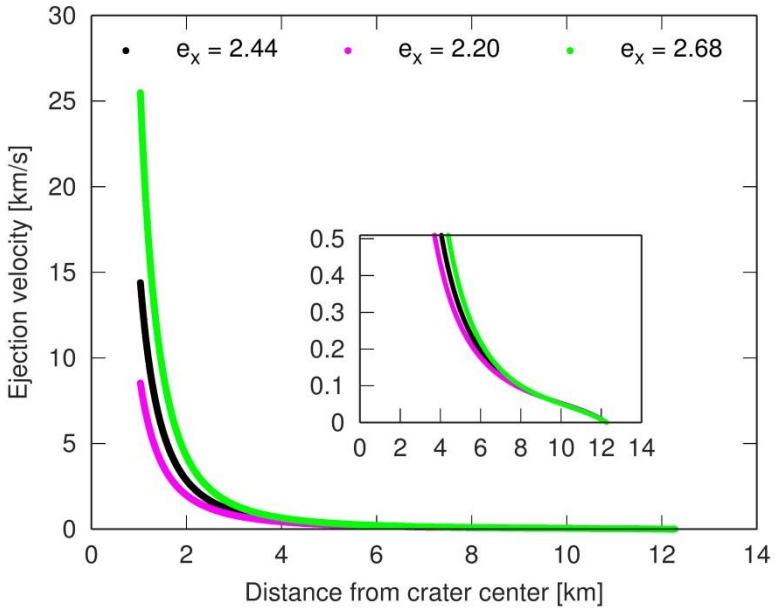

Fig. 5-10. We test the effect of the material parameter e_x on ejection velocities as a function of the particle's distance from the crater center. Our first choice of e_x is 2.44. The variable is varied ± 10% to test its effect on resulting ejection velocities of Crater D. The other parameter λ is kept at 10. The inset shows velocities below Ceres' escape velocity of 0.51 km/s.

5.3.5 Boulder Ejection Velocities

Our calculations show that boulders are ejected at comparably low velocities between 0.3 m/s (Juling) and 71 m/s (Jacheongbi), whereas the total range of velocities for particles that re-impact onto the surface is restricted by the escape velocity of 510 m/s. Figure 5-11 illustrates ejection velocities as a function of the boulders' distances to the crater rim in crater radii. Ejection velocities decrease from the crater center to the crater rim. The flight paths of particles with higher ejection velocities are longer than those for low-velocity particles, which are deposited close to the outside of the crater rim. In addition, we observe that larger craters provide particles with higher velocities than smaller craters. The maximum ejection velocity for the smallest crater Thrud is 34 m/s, and the maximum velocity for the largest crater Jacheongbi is 71 m/s. Most boulders were mapped within a distance of 2 crater radii. Two exceptions are Oxo and Crater C, where ejecta blocks were found beyond. Just like for the global ejecta pattern, we tested the effect of different input variables on the resulting boulder velocities. In comparison with global ejection velocities, variations of projectile and target density, projectile velocity incoming direction and the incoming angle have almost no effect as illustrated for the impact angle and impact direction in Fig. 5-12. However, the vertical scenario (Fig. 5-12b) illustrates the rotational effect on low-velocity ejecta. A vertical impact in a rotating system results in velocity values that are slightly

scattered around that curve due to rotation, because the particles are not any more symmetrically distributed around the crater.

Furthermore, we calculate the location of the corresponding launch sites to the ejecta blocks. Launch and landing sites of all twelve craters are illustrated in Fig. 5-13. The ejection sites of the ejecta blocks are mostly found at the outer edge of the crater floor, where low-velocity particles are ejected. The higher the initial velocity, the closer the launch location is to the crater center.

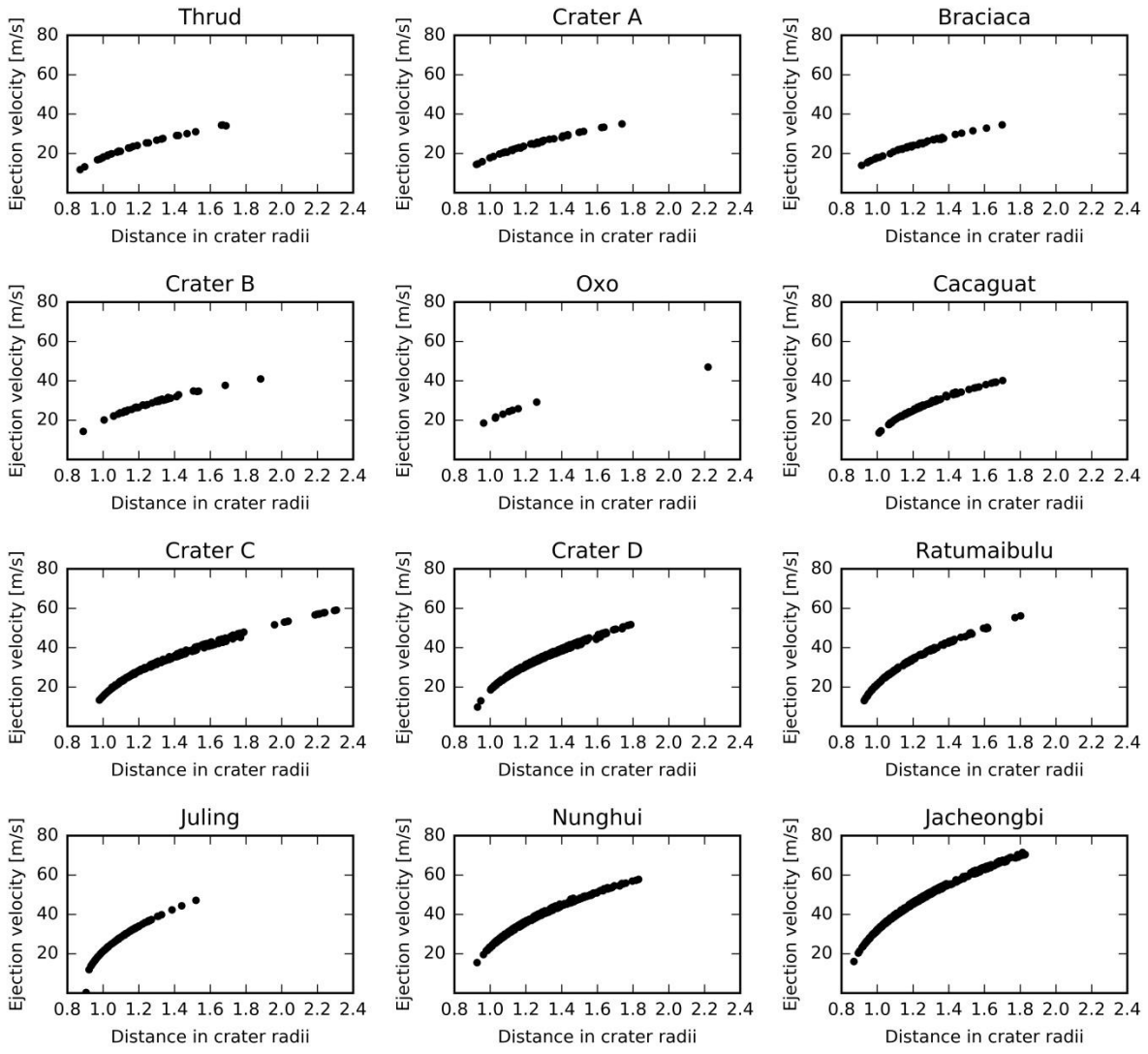

Fig. 5-11. Ejection velocities as a function of the radius of the parent crater, displayed for the boulders of twelve craters

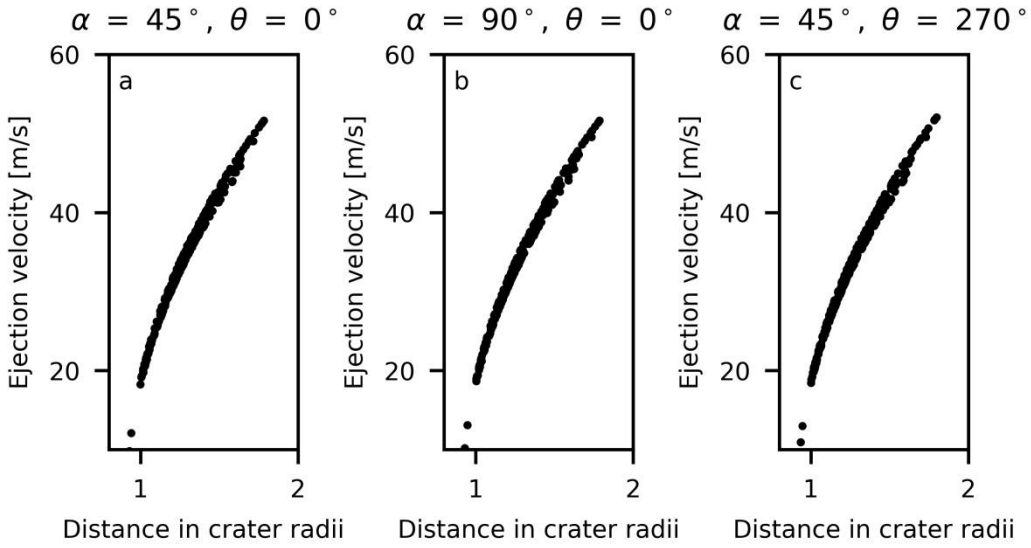

Fig. 5-12. The effect of the impacting angle and impact direction of the projectile on ejection velocities of boulders using the example of Crater D. a) The projectile hits the target with an angle of 45° with respect to the surface with an azimuth of 0°. b) The projectile hits the target with an angle of 90° with an azimuth of 0°. c) The projectile hits the target with an angle of 45° with an azimuth of 270°.

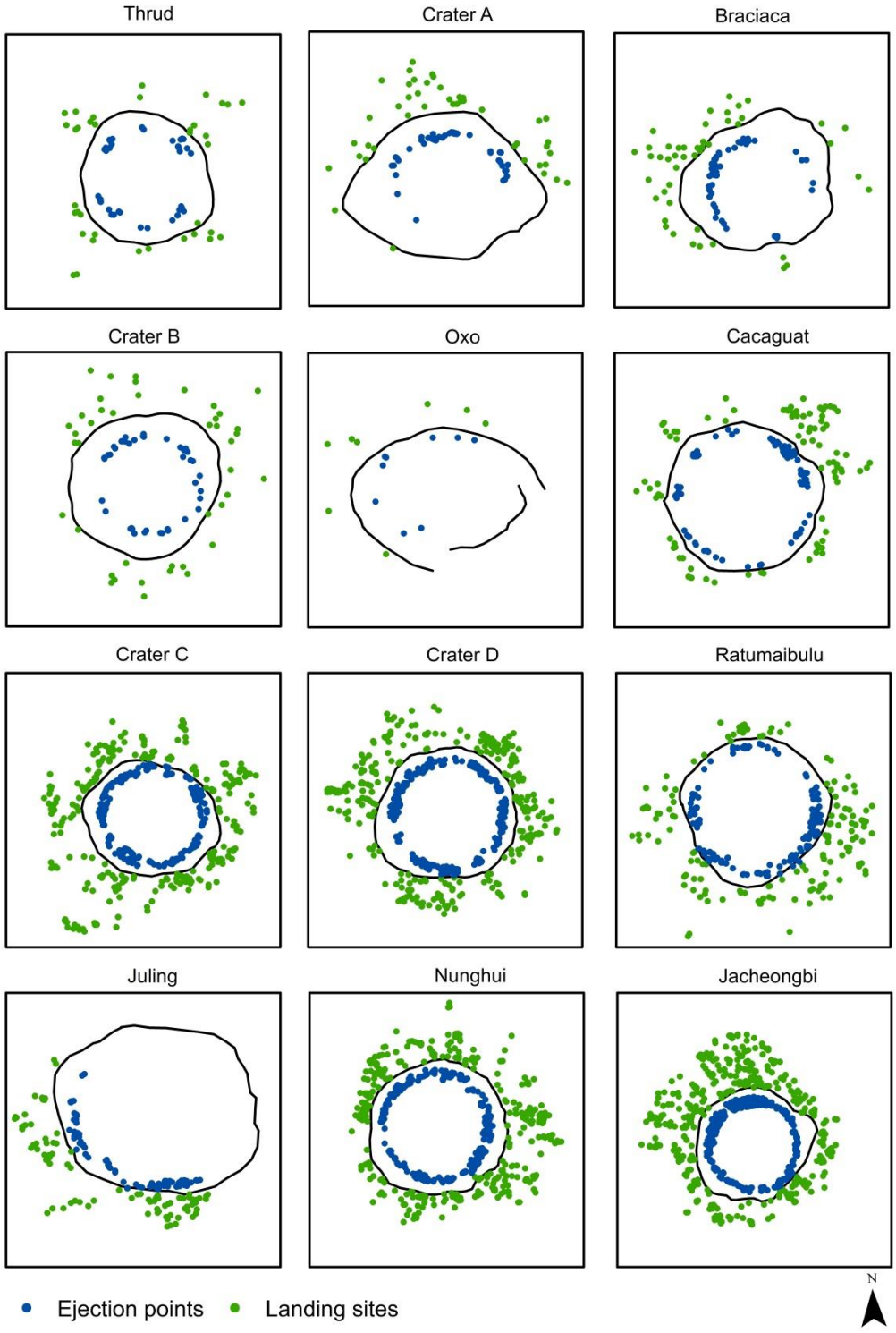

Fig. 5-13. Launch and landing sites of the boulders of twelve craters. Mapped boulder locations are displayed in green and corresponding ejection sites in blue.

5.4 Discussion and Conclusion

We study the influence of the fast rotation and low gravitational acceleration of the dwarf planet Ceres on the global and local (boulder) ejecta deposition pattern as a function of ejection velocity using an analytical approach.

Power-law size-frequency distributions of boulders on Ceres show steep slopes between -4.4 and -6.2. Not all craters' diameter distributions could be approximated by a power-law, because of their shape or too few data points. Using a variety of fitting techniques, steep power-law slopes of boulder diameter distributions are reported, for instance, for the Moon (e.g. Bart and Melosh, 2010b) and the asteroids Lutetia (Küppers et al., 2012), Eros (Chapman et al., 2002) and Toutatis (Jiang et al., 2015). Cumulative distributions of ejecta blocks and also of resulting secondary craters usually have a steeper slopes than cumulative distributions of primary craters because of rock fragmentation (e.g. McEwen and Bierhaus, 2006; Shoemaker, 1965; Wilhelms et al., 1978).

Our model shows that ejected particles from small craters can travel over the entire surface of Ceres. The trajectories of high-velocity particles are bent to a great extent by the Coriolis effect. Particles that will reach such high velocities probably have a very low mass, and not all ejecta will fall back in form of secondary impacts, continuous ejecta and boulders. However, our results are important for the analysis of secondary craters, because they imply that those might be found far away from their primary crater and their line of sight will probably be not straight at all.

Furthermore, we also show that the deposition of low-velocity fragments is influenced by rotation. In addition, as postulated by crater scaling laws, we observe a relationship between boulder velocity and its distance to the crater rim. Ejection velocities are proportional to the impactor's energy; hence, ejecta blocks of large craters reach higher velocities and are transported farther away from the crater rim. As a result, we provide a velocity range in which intact ejecta fragments can be expected.

Our observations of the rotational effect on ejecta deposition on Ceres are in good agreement with studies on other planetary bodies. For Mercury, Dobrovolskis (1981) reported that high-velocity particles string out along a circle of fixed latitude and that ejecta of impacts near the equator deposits symmetrically to the latter. High-velocity (distal) ejecta of high-latitude craters (>45°) on Mars tends to wrap poleward in the opposite hemisphere and equatorially for low-latitude craters (<45°) (Wrobel, 2004).

On the moon, boulder sizes decrease with increasing distance from the crater rim (Bart and Melosh, 2010b; Krishna and Kumar, 2016; Vickery, 1986). Based on that correlation, there is also

a relation between ejection velocity and fragment size (Bart and Melosh, 2010b; Vickery, 1986). In addition, large fragments of large craters on the Moon are ejected at low velocities, whereas small craters do not show such correlation. However, we do not observe such trends in our data, only single observations agree with reported relations. The largest crater in our study is Jacheongbi, with a diameter of 31 km. Its largest boulders are indeed located close to the crater rim and would therefore have been ejected at lower velocities. Reasons for the absence of a relationship between boulder diameter and distance to the crater rim can be material properties in the upper layer, impact conditions and boulder transport mechanisms that might be different for Ceres. A more likely explanation is that the number and quality of data points is not sufficient. Boulder diameter measurements could only be performed for a few craters. We chose those craters that have many large boulders. Even then, some measurements are performed close to the limit of resolution and are not complete for any diameter range, because boulders can be covered by shadows and other boulders. A resolution of 35 m/pixel does not allow the exact measurement of meter-sized fragments. As a result, we think that such a correlation might exist, but can only be seen at higher resolution. By comparing the largest boulders of 30 craters, we find a positive linear correlation between crater size and the largest boulder. For craters below 20 km on the Moon, Phobos, Deimos and Ida, Lee et al. (1996) reported a power-law relationship between those two observations.

The input parameters that have a crucial effect on the distribution of re-impact sites are impact direction and impact angle, because they influence ejection angles and ejection velocities. We choose 45° as the most probable impact angle. The morphologies of the craters do not reveal the exact impact conditions, because only very oblique impacts (<5°) produce the characteristic "butterfly wing" pattern (Pierazzo and Melosh, 2000). A variation of the other input parameters velocity, projectile and target density do not change the final pattern much. However, the influence on single particle trajectories can be much larger. Parameters beside the impact angle and direction are direct inputs in the calculation of the projectile size. While the effect of those parameters on the projectile size is major, the resulting change in velocities and landing sites is small.

Scaling laws were derived from low-velocity laboratory experiments (Werner and Ivanov, 2015), and the materials used do not necessarily resemble the complex mineralogy of Ceres. Ceres' shallow subsurface consists of a mixture of ice (30-40%), rock, salts and/or clathrates (Bland et al., 2016). Prettyman et al. (2017) report surface materials that are rich in hydrogen, especially at mid-to-high latitudes, and have undergone aqueous alteration as seen in neutron and gamma-ray spectroscopy of the Dawn spacecraft that addresses decimeter scales of the shallow subsurface.

They report about 10 wt % water ice in Ceres' ice table and a regolith porosity of 0.2. The thickness and exact composition of the regolith layer on Ceres is not well determined. If craters below < 10 km in this study would have impacted into a thick silicate-rich regolith layer, a porous crater scaling might also be as realistic as a nonporous crater scaling.

Most of the examined craters are morphologically somewhat in between simple and complex, as discussed in section 5.3.1. Because the equations we used are based on the crater morphology, transient diameters sometimes can be under- or overestimated. The start locations of the identified boulders are highly dependent on the location of the crater center, the average crater diameter and the calculated transient crater diameter. Since most of the crater rims deviate considerably from a circular shape, the identification of the location of the center is difficult. As a result, some ejection sites are located at the crater wall, which is unrealistic.

The interpretation of our results will benefit from an overall study of secondary craters on Ceres and studies about the regolith thickness and boulder lifetimes. Size-frequency distributions of secondary craters can then be compared to the distribution of large ejecta blocks. Then again, we have shown that due to long-range particles, secondary craters might be a dominant feature on the surface, and their assignment to primary craters is challenging. Head et al. (2002) found that a regolith cover on Mars reduces ejection speeds. A similar relationship is reported for the Moon (Bart and Melosh, 2010a). However, the determination of regolith thickness by analyzing the morphological shape of small impact craters after an approach by Quaide and Oberbeck (1968) or by measuring regolith thickness directly from high-resolution DEM data (Di et al., 2016a) requires higher resolution.

For the first time, we analytically modeled re-impact sites of boulder crater ejecta and report ejection velocities for boulders on Ceres, taking into account its rapid rotation. Our results provide velocity limits in which intact ejecta fragments can be expected. We show that ejecta of small craters can travel long distances, and trajectories of high-velocity particles are bent to a great extent due to the Coriolis effect. Our results imply that Ceres' surface is largely contaminated with secondaries and that their assignment to specific craters is nearly impossible. Ceres' rotation even influences the trajectories of low-velocity fragments. Ejecta blocks are therefore not necessarily ejected radially.

6 SUMMARY

This thesis describes two methods: the geologic mapping and the ejecta modeling that were used to investigate the surface composition, evolution and material dynamics of the dwarf planet Ceres.

The geologic mapping investigated what geologic units and what materials can be expected on Ceres. It used clear filter images with a resolution of 35 m/pixel supported by color filters and a digital elevation model with a resolution of ~140 m/pixel. Geologic mapping of the southern quadrangle Sintana (0-90°E, 21-66°S) reveals a large variety of impact crater morphologies. Complex craters show terraces, peaks, central ridges and landslides. Moreover, mass wasting features support the assumption of an ice-rich subsurface. Age estimates suggest that the mapping area was resurfaced by the Kerwan impact, about 1 Ga ago. Long-range secondary crater chains that are oriented E-W cross the quadrangle.

Additionally, the thesis investigated how geologic units are deposited. Ballistic calculations take on findings in the quadrangle, but also on global observations. Irregular units, especially in color data and numerous secondary crater chains are indicators for an irregular ejecta deposition. With an analytical approach, the landing sites of test particles were calculated by investigating their elliptical orbits over a rotating sphere. Ballistic calculations confirm that the Coriolis effect can bend particle trajectories and produce asymmetric ejecta deposits. Especially the flight paths of high-velocity particles are deflected and the re-impact sites deviate largely from a radial deposition. The effect is latitude-dependent and highly influenced by the impact geometry. Ejecta deposits can be deposited far away from the primary craters as distal ejecta can range planet-wide. Fragments of larger craters, such as Yalode and Kerwan, are large enough to produce distant non-radial secondary crater chains on Ceres, such as the crater chains Junina Catenae. Thus, the Coriolis effect can produces asymmetric ejecta patterns on Ceres.

At the given resolution, boulders are a rare feature on Ceres and the specifics of boulder craters were investigated by analyzing the boulders itself and their ejection velocities and ejection and landing sites. Mapped boulders show steep power-law slopes in their diameter distribution and reach ejection velocities up to 71 m/s. The steep slopes indicate that they are related to secondary craters. Because of their slow velocities, ejection sites are located close to the crater rim. An investigation of the deposition of ejecta in that velocity range illustrates that the deposition of low-velocity ejecta blocks is influenced by rotational effects as well.

The results of the ballistic calculations are relevant for age estimations. A high contamination with secondary craters is very likely. Those craters tend to make surfaces older if they cannot be distinguished from primary craters. Absolute age measurements can only look for crater clustering as a hint for a contamination with secondaries. Therefore, age dating should be handled with care, especially when small craters are used. The assignment of specific geologic ejecta units to their source impacts is highly complicated by the expected long and more important non-radial range of ejecta. Modeling shows that ejecta of large craters can be deposited far away from the actual impact location.

Further studies would benefit from images with a higher resolution, sample-return missions, numerical studies about ejecta deposition on Ceres and Vesta and more detailed studies about the distribution of secondary craters on Ceres.

To conclude, this thesis confirms that Ceres probably has an ice-rich crust. Furthermore, the thesis illustrates for the first time how the rotational dynamics of Ceres influence its ejecta deposition. Ejecta material experiences a rotational trajectory bending. Asymmetric proximal and distal ejecta deposits and non-radial secondary crater chains can be the results.

To summarize the achievement of this work: Ceres' geology is a result of geometrically irregular impact resurfacing and overprinting due to Ceres' ejection dynamics.

APPENDIX: CODE FOR LANDING SITE CALCULATION

The following code was written in Octave (Eaton et al., 2015). The same structure is used for all landing site calculations. The inputs files for the boulder code include coordinates of boulders and the coordinates and diameters of boulder craters.

```
pkg load symbolic
pkg load io
```

```
%%%%%%%%%%%%%%%%%%%%%%%%%%%%%%%%%%%%%%%%%%%%%%%%%%%%%%%%%%%%%%%%%%%%%%%%%%%%%%%
%%%%%%%%%% GENERATE TEST PARTICLES, EJECTION VELOCITIES AND ANGLES %%%%%%%%
%%%%%%%%%%%%%%%%%%%%%%%%%%%%%%%%%%%%%%%%%%%%%%%%%%%%%%%%%%%%%%%%%%%%%%%%%%%%%%%
```

```
%%%%%%%----------PARAMETER CERES ------------------------------------%%%
```

```
g                 =   0.00028; %% in km/s^2
densityTarget     =   1815;
Dsg               =   1.75;
Dsc               =   10.3;
RCereskm          =   476;
RCeresnorm        =   1;
r                 =   RCeresnorm;

nn                = 1 00000;
```

```
%%%--------------- READ FILES WITH BOULDER COORDINATES ----------------%%%
```

```
dirname = "E:/Boulders/Locations/FinalInputFiles2/*.txt";
liste=dir(dirname);
files = {liste.name};

finalLatsAll = {};
finalLonsAll = {};
velAll = {};
distancesAll = {};

names = {"A_Thrud", "B_CraterA", "C_Braciaca", "D_CraterB", "E_Oxo",...
 "F_Cacaguat", "G_CraterC", "H_CraterD", "I_Ratumaibulu", "J_Juling", ...
 "K_Nunghui", "L_Jacheongbi"};
```

```
%%%----------------GENERATION OF TEST PARTICLES---------------------%%%%
```

```
for k= 1:numel(files)

  filename = ["E:/Boulders/Locations/FinalInputFiles2/",files{k}

];
  data = dlmread(filename, SEP = ";");

  %%% first line is header
  %%% second line contains diameter and location of boulder crater

  Dcrater = data(2,2);
  craterRadius      =   Dcrater / 2;
  craterLon = data(2,3);
```

```
craterLat = data(2,4);

%% Rest are boulder locations
data(1:2,:) = []; %% deleate header and crater infos

bouldersLon = data(:,3);
bouldersLat = data(:,4);


%%% CALCULATE TRANSIENT CRATER DIAMETER

if Dcrater < Dsc
  Dtransient = Dcrater / 1.25;
else
  Dtransient        = Dsc^0.15 * Dcrater^0.85;
end
Rtransient = Dtransient / 2;

Rcalc = Rtransient;
Dcalc = Dtransient;

%%% PARAMETER PROJECTILE
Vprojectile       = 4.79;
%%% km/s mean for Ceres

angleProjectile   = 45;

densityProjectile = 3000;
%%% kg/m^3

%%%  CALCULATE PROJECTILE SIZE

Cd           = (1.16 * (densityProjectile / densityTarget)^(1/3) * ...
                (Vprojectile * sind(angleProjectile))^0.44) ^(1 / 0.78);

Dprojectile2 = (Dcalc * (g * (Dsg + Dcalc))^0.282) / Cd

projectileRadius = Dprojectile2/2;

%%% DISTRIBUTE PARTICLES INSIDE CRATER/CIRCLE ON SPHERE

%%% normalized transient crater radius, max start radius
r1 = (Rcalc) / RCereskm;

%%% normalized projectile radius, min start radius
r2 = projectileRadius / RCereskm;

z1 = []; z2 = []; zRing = []; phiCrater = []; xCrater= []; yCrater= [];
azimuths = []; xnew = []; znew = []; xnew2 = []; ynew = []; lon = [];
lat = []; r3 = []; distance = []; vel = [];

z1 = rand(nn,1) * (cos(r1) - r) - cos(r1);
z2 = rand(nn,1) * (cos(r2) - r) - cos(r2);
zRing = z1(z1> max(z2));

lring = length(zRing);
nn = lring;
phiCrater = rand(lring,1)*2*pi;

xCrater   = sqrt(r - zRing.*zRing).*cos(phiCrater);
yCrater   = sqrt(r - zRing.*zRing).*sin(phiCrater);
```

```
%%% ROTATION OF CRATER ON SPHERE FROM POLE

%%% ROTATION PART 1 (LATITUDE)
beta            =   (90 + craterLat) * pi / 180;
gamma           =   (craterLon - 180 ) * pi / 180;
xnew            =   xCrater * cos(beta) + zRing * sin(beta);
znew            =   - xCrater * sin(beta) + zRing * cos(beta);

%%% ROTATION PART 2 (LONGITUDE)
xnew2           =   xnew * cos(gamma) - yCrater * sin(gamma);
ynew            =   xnew * sin(gamma) + yCrater * cos(gamma);

%%% TRANSFORMATION CARTESIAN TO SPHERICAL COORDINATES
[lon, lat, r3]  = cart2sph(xnew2, ynew, znew);
```

```
%%%---------------- CALCULATION OF EJECTION VELOCITIES----------------%%%
```

```
%%% CALCULATE LAUNCH DISTANCE FROM CRATER CENTER

distance = [];

for i = 1: nn
  dlat          =   craterLat * pi / 180 - lat(i);
  dlon          =   craterLon * pi / 180 - lon(i);
  haversine(i)  =   sin(dlat / 2)^2 + cos(lat(i)) * ...
                    cos(craterLat * pi / 180) * sin(dlon / 2)^2;
  c(i)          =   2 * atan2(sqrt(haversine(i)), ...
                    sqrt(1 -  haversine(i)));
  distance(i)   =   c(i) * RCereskm ;
end

%%% CALCULATE AZIMUTHS
craterLatRad = craterLat * pi / 180;
craterLonRad = craterLon * pi / 180;

for i = 1: nn
  difflon = lon(i) - craterLonRad;
  azimuths(i) = atan2(sin(difflon) * cos(lat(i)), ...
                cos(craterLatRad) * sin(lat(i)) - ...
                sin(craterLatRad) * cos(lat(i)) * cos(difflon));
end

alpha = -2.44;
lambda = 10;
vel = 2 * sqrt(Rcalc * g) * (distance / Rcalc).^(alpha) / ...
      (-alpha + 1)- 2 * sqrt(Rcalc * g) * ...
      (distance / Rcalc).^(lambda) / (-alpha + 1);
```

```
%%% ------------ CALCULATION OF EJECTION ANGLES ---------------------%%%
```

```
psi0 = 52;
psid = 18;

if (angleProjectile == 90)
  psin          =   psi0 - psid * (distance / Rcalc);
  ejectionAngle =   psin;
elseif (angleProjectile != 90)
  psif          =   [];
  velo          = [];
  psin          =   psi0 - psid * (distance / Rcalc);
```

```
    for i = 1: length(phiCrater)
        psif(i)    =    psin(i) - (30 * cosd(angleProjectile) * ...
                       ((1 - cosd(azimuths(i) * 180 / pi) )/ 2)* ...
                       (1 - distance(i) / Rcalc)^2);
        velo(i)    =    ((vel(i) * sind(psin(i)))^2 + (vel(i) * ...
                        sind(psin(i)) / tand(psif(i)))^2)^(1/2);
    end
    ejectionAngle  = psif;
    vel = velo;
  end
```

```
%%%%%%%%%%%%%%%%%%%%%%%%%%%%%%%%%%%%%%%%%%%%%%%%%%%%%%%%%%%%%%%%%%%%%%%%%%%%%%%
%%%%%%%%%%%%% CALCULATE TRAJECTORIES AFTER DOBROVOLSKIS ('81) %%%%%%%%%%%%%%%
%%%%%%%%%%%%%%%%%%%%%%%%%%%%%%%%%%%%%%%%%%%%%%%%%%%%%%%%%%%%%%%%%%%%%%%%%%%%%%%
```

```
  particleStartLon = lon * 180 / pi;
  particleStartLat = lat * 180 / pi;
  particleStartColat = ((90 - particleStartLat)* pi/180);
  particleStartAzinuth = azimuths;

  %%% DIMENSIONLESS ANALYSIS

  %%% ESCAPE VELOCITY SQRT(2) --> OTHER EQUIVALENT

  particleStartVel = vel;
  escapeVel = 0.51  % km/s
  particleInitVel = particleStartVel * sqrt(2) / escapeVel;

  %%% ANGLE TO THE PERPENDICULAR

  launch_angle = 90 * pi/180 - ejectionAngle * pi/180;
  rotPeriod = 9.074;  % in hr
  bulkDensity = 2.162; %g/cm^3
  radius = 1;
  G = 1;
  mass = 1;
  RCeres = 476000; % m
  gCeres = 0.28; % m/s^2
  t = sqrt(RCeres / gCeres);

  %%% DIMENSIONLESS ANGULAR SPEED
  omega = 3.3 / ( sqrt(bulkDensity) * rotPeriod);


  %%% TRAJECTORIES OVER ROTATING BODY OVER SPHERE

  finalLats = zeros(nn,1); finalLons = zeros(nn,1);
  planetocentricDistances = zeros(nn,1);
  azimuthFinals = zeros(nn,1);Ts = zeros(nn,1);as = zeros(nn,1);
  deltas = zeros(nn,1);lat_secondaries = zeros(nn,1);
  lon_reimpacts = zeros(nn,1); deltas = zeros(nn,1);

  for p = 1:nn
      b             = []; vx            = []; init_vel0     = [];
      launch_angle0 = []; azimuths0     = []; delta         = [];
      lat_secondary = []; lon_reimpact  = []; vel_h         = [];
      e             = []; a             = []; E             = [];
      n             = []; T             = []; lon_final     = [];
      planetocentricDistance            = []; azimuthFinal  = [];
      finalLonDeg   = []; finalLatDeg   = [];
```

```
b         = omega * radius *sin(particleStartColat(p));

vx        = particleInitVel(p) * sin(launch_angle(p)) *...
            sin(particleStartAzinuth(p)) + b;

init_vel0 = sqrt(particleInitVel(p)^2 + b^2 + 2 * ...
            particleInitVel(p) * ...
            sin(launch_angle(p))* b * sin(particleStartAzinuth(p)));

if init_vel0 >= sqrt(2)

finalLats(p)        = nan;    finalLons(p)                 = nan;
particleStartLat(p) = nan;    particleStartLon(p)          = nan;
azimuthFinals(p)    = nan;    planetocentricDistances(p)   = nan;
vel(p)              = nan;    distance(p)                  = nan;
deltas(p)           = nan;    as(p)                        = nan;
Ts(p)                       = nan;
particleStartAzinuth(p)     = nan;
launch_angle(p)             = nan;

elseif init_vel0 < sqrt(2)

launch_angle0 = acos( particleInitVel(p) / (init_vel0)  * ...
                cos(launch_angle(p)));

%%% NEGATIVE VELOCITY VX --> AZIMUTH BETWEEN PI and 2PI %%%

if (vx >= 0)
  azimuths0 = acos(tan(launch_angle(p))/tan(launch_angle0) * ...
              cos(particleStartAzinuth(p)));
else
  azimuths0 = 2 * pi - acos(tan(launch_angle(p))/ ...
              tan(launch_angle0) * ...
              cos(particleStartAzinuth(p)));
end

%%% PARAMETERS OF ELLIPTICAL TRAJECTORY

 vel_h  = init_vel0 * sin(launch_angle0);

 e      =   sqrt(1 - vel_h^2 *(2 - init_vel0^2));
 a      =   1 / (2 - init_vel0^2);
 E      =   acos(init_vel0^2 / e - 1 / e);
 n      =   sqrt(G * mass / a^3);
 T      =   2 * (pi - E + e * sin(E)) * a^(3/2);
 delta  =   2 * acos(1 / e - vel_h^2 / e);

 %%% CALCULATION OF LANDING SITES

 lat_secondary  = acos(cos(particleStartColat(p)) * cos(delta) ...
                  + sin(particleStartColat(p)) * sin(delta) * ...
                  cos(azimuths0));

 %%% AZIMUTHS BETWEEN PI AND 2PI --> NEGATIVE LONGITUDE %%%

 if (pi < azimuths0) && (azimuths0 < 2 * pi)
   lon_reimpact =  -1 * acos((cos(delta) ...
                  - cos(particleStartColat(p)) * ...
                   cos(lat_secondary)) / ...
                  (sin(particleStartColat(p)) * ...
                   sin(lat_secondary)));
```

```
      else
        lon_reimpact = acos((cos(delta) - cos(particleStartColat(p)) ...
                       * cos(lat_secondary)) / ...
                       (sin(particleStartColat(p)) * ...
                       sin(lat_secondary)));
      end


      %%% LANDING SITES WITH RESPECT TO SPINNING SURFACE

      lat_secondaries(p) =   90 - lat_secondary * 180/pi;
      lon_reimpacts(p)   =   lon_reimpact * 180/pi  ;

      lon_final          =   lon_reimpact - omega * T;

      planetocentricDistance = acos(cos(particleStartColat(p)) * ...
                               cos(lat_secondary) + ...
                               sin(particleStartColat(p))...
                               * sin(lat_secondary) * cos(lon_final));

      if lon_final >= 0
       azimuthFinal = acos(( cos(lat_secondary) - ...
                      cos(particleStartColat(p)) * ...
                      cos(planetocentricDistance)) ...
                      / (sin(particleStartColat(p))...
                     * sin(planetocentricDistance)));
      else
       azimuthFinal = 2 * pi - acos(( cos(lat_secondary) - ...
                     cos(particleStartColat(p)) ...
                     * cos(planetocentricDistance)) / ...
                     (sin(particleStartColat(p))...
                      * sin(planetocentricDistance)));
      end

      %%% IN DEG
            finalLat = 90 - lat_secondary * 180/pi;
      finalLon = lon_final * 180/pi + particleStartLon(p) ;

      %% PARTICLES THAT ORBIT CERES, LONGITUDES < 180 and > 180

      while finalLon < -180
            finalLon = 360 + finalLon;
      end
      while finalLon > 180
            ps(p)    = p;
           finalLon  = - 360 + finalLon;
      end


      finalLats(p)               = finalLat;
      finalLons(p)               = finalLon;
      azimuthFinals(p)           = azimuthFinal;
      planetocentricDistances(p) = planetocentricDistance;
      deltas(p)                  = delta;
      as(p)                      = a;
      Ts(p)                      = T;
     end
  end

  %%% DELETE NANS %%%
  finalLons(isnan(finalLons))               = [];
  finalLats(isnan(finalLats))               = [];
```

```
particleStartLat(isnan(particleStartLat)) = [];
particleStartLon(isnan(particleStartLon)) = [];
vel(isnan(vel))                           = [];


finalLatsAll = finalLats;  finalLonsAll = finalLons;
velAll       = vel;        distancesAll{k} = distance;

%%% SAVE RESULTS TO FILE

dataPrint2    = [real(vel)', real(finalLons), real(finalLats), ...
                  real(particleStartLon), real(particleStartLat)];
savefilename2 = ["E:/Boulders/Velcalc/Start/DobNewRevise/",...
                names{k}, ".txt"]
dlmwrite(savefilename2, dataPrint2, "delimiter", ",");

end
```

REFERENCES

Ai, H.-A., Ahrens, T. J., 2004. Dynamic tensile strength of terrestrial rocks and application to impact cratering. Meteoritics & Planetary Science. 39**,** pp. 233-246.

Alstott, J., et al., 2014. powerlaw: A Python Package for Analysis of Heavy-Tailed Distributions. PLOS ONE. 9**,** p. e85777.

Alvarellos, J. L., et al., 2002. Orbital evolution of impact ejecta from Ganymede. Icarus. 160**,** pp. 108-123.

Alvarellos, J. L., et al., 2005. Fates of satellite ejecta in the Saturn system. Icarus. 178**,** pp. 104-123.

Alvarellos, J. L., et al., 2017. Fates of satellite ejecta in the Saturn system, II. Icarus. 284**,** pp. 70-89.

Alvarez, W., 1996. Trajectories of ballistic ejecta from the Chicxulub Crater. In: G. Ryder, D. E. Fastovsky, S. Gartner, (Eds.), The Cretaceous-Tertiary Event and Other Catastrophes in Earth History. Geological Society of America, pp. 141-150.

Anderson, J. L., et al., 2003. Asymmetry of ejecta flow during oblique impacts using three-dimensional particle image velocimetry. Journal of Geophysical Research: Planets. 108**,** p. 5094.

Anderson, J. L., et al., 2004. Experimental ejection angles for oblique impacts: Implications for the subsurface flow-field. Meteoritics & Planetary Science. 39**,** pp. 303-320.

Arora, C. L., 1981. Refresher Course in B.Sc. Physics (Vol. I). Chand, p. 125ff.

Artemieva, N., Ivanov, B., 2004. Launch of martian meteorites in oblique impacts. Icarus. 171**,** pp. 84-101.

Baker, D. M. H., et al., 2011. The transition from complex crater to peak-ring basin on Mercury: New observations from MESSENGER flyby data and constraints on basin formation models. Planetary and Space Science. 59**,** pp. 1932-1948.

Barber, C. B., et al., 1996. The quickhull algorithm for convex hulls. ACM Transactions on Mathematical Software (TOMS). 22**,** pp. 469-483.

Bart, G. D., Melosh, H. J., 2007. Using lunar boulders to distinguish primary from distant secondary impact craters. Geophysical Research Letters. 34**,** p. L07203.

Bart, G. D., Melosh, H. J., 2010a. Impact into lunar regolith inhibits high-velocity ejection of large blocks. J. Geophys. Res.: Planets. 115**,** p. E08004.

Bart, G. D., Melosh, H. J., 2010b. Distributions of boulders ejected from lunar craters. Icarus. 209**,** pp. 337-357.

Basilevsky, A. T., et al., 2013. Survival times of meter-sized boulders on the surface of the Moon. Planetary and Space Science. 89**,** pp. 118-126.

Basilevsky, A. T., et al., 2015. Survival times of meter-sized rock boulders on the surface of airless bodies. Planetary and Space Science. 117**,** pp. 312-328.

Batson, R., et al., 1990. History of planetary cartography. Planetary Mapping. p. 12.

Bewick, V., et al., 2003. Statistics review 7: Correlation and regression. Critical Care. 7**,** p. 451.

Bierhaus, E. B., et al., 2012. The role of ejecta in the small crater populations on the mid-sized saturnian satellites. Icarus. 218**,** pp. 602-621.

Binzel, R. P., Xu, S., 1993. Chips off of Asteroid 4 Vesta: Evidence for the Parent Body of Basaltic Achondrite Meteorites. Science. 260**,** pp. 186-191.

Blair, E. C., 2002. Asteroids: Overview, Abstracts, and Bibliography. Nova Science Publishers, p. 2.

Bland, M. T., 2013. Predicted crater morphologies on Ceres: Probing internal structure and evolution. Icarus. 226**,** pp. 510–521.

Bland, M. T., et al., 2016. Composition and structure of the shallow subsurface of Ceres revealed by crater morphology. Nature Geosci. 9**,** pp. 538-542.

Bu, C., et al., 2017. Search for sulfates on the surface of Ceres. Meteoritics & Planetary Science. in press.

Buckingham, E., 1914. On Physically Similar Systems; Illustrations of the Use of Dimensional Equations. Physical Review. 4**,** pp. 345-376.

Buczkowski, D. L., et al., 2016. The geomorphology of Ceres. Science. 353**,** p. aaf4332.

Buczkowski, D. L., et al., 2018. The geology of the occator quadrangle of dwarf planet Ceres: Floor-fractured craters and other geomorphic evidence of cryomagmatism. Icarus. 316**,** pp. 128-139.

Castillo-Rogez, J. C., McCord, T. B., 2010. Ceres' evolution and present state constrained by shape data. Icarus. 205**,** pp. 443–459.

Chandrasekar, A., 2010. Basics Of Atmospheric Science. PHI Learning Pvt. Ltd, p. 159.

Chapman, C. R., et al., 2002. Impact history of Eros: Craters and boulders. Icarus. 155**,** pp. 104-118.

Chow, T. L., 2013. Classical Mechanics, Second Edition. CRC Press, p. 350.
Cintala, M. J., et al., 1999. Ejection-velocity distributions from impacts into coarse-grained sand. Meteoritics & Planetary Science. 34**,** pp. 605-623.
Clauset, A., et al., 2009. Power-law distributions in empirical data. SIAM Review. 51**,** pp. 661-703.
Collins, G., Wünnemann, K., 2007. Numerical modeling of impact ejection processes in porous targets. Lunar and Planetary Science Conference, Vol. 38, p. 1789.
Collins, G. S., et al., 2002. Hydrocode Simulations of Chicxulub Crater Collapse and Peak-Ring Formation. Icarus. 157**,** pp. 24-33.
Collins, G. S., et al., 2005. Earth Impact Effects Program: A Web-based computer program for calculating the regional environmental consequences of a meteoroid impact on Earth. Meteoritics & Planetary Science. 40**,** pp. 817-840.
Combe, J. P., et al., 2016. Detection of local H2O exposed at the surface of Ceres. Science. 353**,** p. aaf3010.
Coradini, A., et al., 2011. Vesta and Ceres: Crossing the History of the Solar System. Space Science Reviews. 163**,** pp. 25-40.
Croft, S. K., 1985. The scaling of complex craters. Journal of Geophysical Research: Solid Earth. 90**,** pp. C828-C842.
Crown, D. A., et al., 2018. Geologic mapping of the Urvara and Yalode Quadrangles of Ceres. Icarus. 316**,** pp. 167-190.
Davis, D. R., et al., 1981. The unusual dynamical environment of Phobos and Deimos. Icarus. 47**,** pp. 220-233.
de Elía, G. C., Di Sisto, R. P., 2011. Impactor flux and cratering on Ceres and Vesta: implications for the early solar system. A&A. 534**,** p. A129.
De Sanctis, M. C., et al., 2011. The VIR Spectrometer. Space Sci. Rev. 163**,** pp. 329–369.
De Sanctis, M. C., et al., 2012. Spectroscopic Characterization of Mineralogy and Its Diversity Across Vesta. Science. 336**,** p. 697.
De Sanctis, M. C., et al., 2016. Bright carbonate deposits as evidence of aqueous alteration on (1) Ceres. Nature. 536**,** pp. 54-57.
De Sanctis, M. C., et al., 2017a. Localized aliphatic organic material on the surface of Ceres. Science. 355**,** pp. 719-722.
De Sanctis, M. C., et al., 2017b. Ac-H-11 Sintana and Ac-H-12 Toharu quadrangles: Assessing the large and small scale heterogeneities of Ceres' surface. Icarus. in press.
DeSouza, I., et al., 2015. Improved techniques for size–frequency distribution analysis in the planetary sciences: Application to blocks on 25143 Itokawa. Icarus. 247**,** pp. 77-80.
Di, K., et al., 2016a. Lunar regolith thickness determination from 3D morphology of small fresh craters. Icarus. 267**,** pp. 12-23.
Di, K., et al., 2016b. Rock size-frequency distribution analysis at the Chang'E-3 landing site. Planetary and Space Science. 120**,** pp. 103-112.
Dobrovolskis, A., 1981. Ejecta patterns diagnostic of planetary rotation. Icarus. 47**,** pp. 203-219.
Dobrovolskis, A. R., et al., 2010. Exchange of ejecta between Telesto and Calypso: Tadpoles, horseshoes, and passing orbits. Icarus. 210**,** pp. 436-445.
Dowling, D. R., Dowling, T. R., 2013. Scaling of impact craters in unconsolidated granular materials. American Journal of Physics. 81**,** pp. 875-878.
Durda, D. D., et al., 2012. Detecting crater ejecta-blanket boundaries and constraining source crater regions for boulder tracks and elongated secondary craters on Eros. Meteoritics & Planetary Science. 47**,** pp. 1087-1097.
Eaton, J. W., et al., 2015. GNU Octave version 4.0.0 manual: a high-level interactive language for numerical computations.
Elbeshausen, D., et al., 2012. Landslides triggered by impacts on asteroid (21) Lutetia? , EPSC 2012, 673 (abstract).
Ermakov, A. I., et al., 2017. Constraints on Ceres' Internal Structure and Evolution From Its Shape and Gravity Measured by the Dawn Spacecraft. Journal of Geophysical Research: Planets. 122**,** pp. 2267-2293.
Evans, J. D., 1996. Straightforward statistics for the behavioral sciences. Brooks/Cole.
Fagents, S. A., 2003. Considerations for effusive cryovolcanism on Europa: The post-Galileo perspective. J. Geophys. Res.: Planets. 108**,** pp. 0148-0227.

Fassett, C. I., 2016. Analysis of impact crater populations and the geochronology of planetary surfaces in the inner solar system. Journal of Geophysical Research: Planets. 121**,** pp. 1900-1926.
Fu, R. R., et al., 2017. The interior structure of Ceres as revealed by surface topography. Earth and Planetary Science Letters. 476**,** pp. 153-164.
Gabler, R. E., et al., 2008. Physical Geography. Cengage Learning, pp. 118-119.
Garry, W. B., et al., 2014. Geologic mapping of ejecta deposits in Oppia Quadrangle, Asteroid (4) Vesta. Icarus. 244**,** pp. 104-119.
Garvin, J., et al., 2000. Global geometric properties of Martian impact craters: An assessment from Mars Orbiter Laser Altimeter (MOLA) digital elevation models. Lunar Planet. Sci. XXX, p. 1619 (abstract).
Gault, E. D., et al., 1968. Impact cratering mechanics and structures. In: R. Greeley, P. H. Schultz, (Eds.), A Primer in Lunar Geology, pp. 177-189.
Geissler, P., et al., 1996. Erosion and ejecta reaccretion on 243 Ida and its moon. Icarus. 120**,** pp. 140-157.
Giamboni, L. A., 1959. Lunar Rays: Their Formation and Age. The Astrophysical Journal. 130**,** p. 324.
Gladman, B. J., et al., 1995. The dynamical evolution of lunar impact ejecta. Icarus. 118**,** pp. 302-321.
Goel, V. K., 2007. Fundamentals Of Physics Xi. McGraw-Hill Education (India) Pvt Limited, p. 10.25.
Golombek, M. P., et al., 2003. Rock size-frequency distributions on Mars and implications for Mars Exploration Rover landing safety and operations. Journal of Geophysical Research: Planets. 108**,** p. 8086.
Gomes, R., et al., 2005. Origin of the cataclysmic Late Heavy Bombardment period of the terrestrial planets. Nature. 435**,** p. 466.
Goossens, S., et al., 2017. Evidence for a low bulk crustal density for Mars from gravity and topography. Geophysical Research Letters. 44**,** pp. 7686-7694.
Gouhier, M., Donnadieu, F., 2008. Mass estimations of ejecta from Strombolian explosions by inversion of Doppler radar measurements. Journal of Geophysical Research: Solid Earth. 113.
Grady, D. E., Kipp, M. E., 1980. Continuum modelling of explosive fracture in oil shale. International Journal of Rock Mechanics and Mining Sciences & Geomechanics Abstracts. 17**,** pp. 147-157.
Greenhagen, B. T., et al., 2016. Origin of the anomalously rocky appearance of Tsiolkovskiy crater. Icarus. 273**,** pp. 237-247.
Hall, J. L., et al., 1981. Lunar floor-fractured craters: Evidence for viscous relaxation of crater topography. Journal of Geophysical Research: Solid Earth. 86**,** pp. 9537-9552.
Hartmann, W. K., 1969. Terrestrial, lunar, and interplanetary rock fragmentation. Icarus. 10**,** pp. 201-213.
Head, J. N., et al., 2002. Martian Meteorite Launch: High-Speed Ejecta from Small Craters. Science. 298**,** pp. 1752-1756.
Head, J. W., 2010. Transition from complex craters to multi-ringed basins on terrestrial planetary bodies: Scale-dependent role of the expanding melt cavity and progressive interaction with the displaced zone. Geophysical Research Letters. 37**,** p. L02203.
Hiesinger, H., et al., 2016. Cratering on Ceres: Implications for its crust and evolution. Science. 353**,** p. aaf4759.
Holsapple, K. A., 1993. The Scaling of Impact Processes in Planetary Sciences. Annual Review of Earth and Planetary Sciences. 21**,** pp. 333-373.
Hood, L. L., Artemieva, N. A., 2008. Antipodal effects of lunar basin-forming impacts: Initial 3D simulations and comparisons with observations. Icarus. 193**,** pp. 485-502.
Hörz, F., et al., 1975. Catastrophic rupture of lunar rocks: A Monte Carlo simulation. The moon. 13**,** pp. 235-258.
Housen, K. R., et al., 1983. Crater ejecta scaling laws: Fundamental forms based on dimensional analysis. J. Geophys. Res.: Solid Earth. 88**,** pp. 2485-2499.
Hsieh, H. H., Jewitt, D., 2006. A Population of Comets in the Main Asteroid Belt. Science. 312**,** p. 561.
Ivanov, B., 2008. Size-Frequency Distribution Of Asteroids And Impact Craters: Estimates Of Impact Rate. In: V. Adushkin, I. Nemchinov, (Eds.), Catastrophic Events Caused by Cosmic Objects. Springer Netherlands, Dordrecht, pp. 91-116.
Ivanov, B. A., 2001. Mars/Moon Cratering Rate Ratio Estimates. Space Science Reviews. 96**,** pp. 87-104.
Ivanov, B. A., 2006. Notes about secondary crater SFD. Planetary Chronology Workshop, p. 6018 (abstract).

Jha, A. K., 2009. A Textbook Of Applied Physics. I.K. International Publishing House Pvt. Limited, p. 346 ff.

Jiang, Y., et al., 2015. Boulders on asteroid Toutatis as observed by Chang'e-2. Scientific reports. 5**,** p. 16029.

Jutzi, M., et al., 2013. The structure of the asteroid 4 Vesta as revealed by models of planet-scale collisions. Nature. 494**,** p. 207.

Kenkmann, T., Dalwigk, I., 2000. Radial transpression ridges: A new structural feature of complex impact craters. Meteorit. Planet. Sci. 35**,** pp. 1189–1201.

Kneissl, T., et al., 2011. Map-projection-independent crater size-frequency determination in GIS environments—New software tool for ArcGIS. Planet. Space Sci. 59**,** pp. 1243–1254.

Koeberl, C., 2003. The Late Heavy Bombardment in the Inner Solar System: Is there any Connection to Kuiper Belt Objects? Earth, Moon, and Planets. 92**,** pp. 79-87.

Konopliv, A. S., et al., 2011. The Dawn gravity investigation at Vesta and Ceres. Space Sci. Rev. 163**,** pp. 461–486.

Konopliv, A. S., et al., 2014. The Vesta gravity field, spin pole and rotation period, landmark positions, and ephemeris from the Dawn tracking and optical data. Icarus. 240**,** pp. 103-117.

Krasinsky, G. A., et al., 2002. Hidden Mass in the Asteroid Belt. Icarus. 158**,** pp. 98-105.

Krishna, N., Kumar, P. S., 2016. Impact spallation processes on the Moon: A case study from the size and shape analysis of ejecta boulders and secondary craters of Censorinus crater. Icarus. 264**,** pp. 274-299.

Krohn, K., et al., 2016. Cryogenic flow features on Ceres: Implications for crater-related cryovolcanism. Geophysical Research Letters. 43**,** pp. 11994-12003.

Krohn, K., et al., 2018. The unique geomorphology and structural geology of the Haulani crater of dwarf planet Ceres as revealed by geological mapping of equatorial quadrangle Ac-6 Haulani. Icarus. 316**,** pp. 84-98.

Küppers, M., et al., 2012. Boulders on lutetia. Planetary and Space Science. 66**,** pp. 71-78.

Küppers, M., et al., 2014. Localized sources of water vapour on the dwarf planet (1) Ceres. Nature. 505**,** pp. 525–527.

Kurosawa, K., et al., 2018. Hydrocode modeling of the spallation process during hypervelocity impacts: Implications for the ejection of Martian meteorites. Icarus. 301**,** pp. 219-234.

Lagerkvist, C.-I., Magnusson, P., 1990. Analysis of asteroid lightcurves. II-Phase curves in a generalized HG-system. Astronomy and Astrophysics Supplement Series. 86**,** pp. 119-165.

Lange, M. A., Ahrens, T. J., 1983. The dynamic tensile strength of ice and ice-silicate mixtures. Journal of Geophysical Research: Solid Earth. 88**,** pp. 1197-1208.

Lee, P., et al., 1996. Ejecta blocks on 243 Ida and on other asteroids. Icarus. 120**,** pp. 87-105.

Levison, H. F., et al., 2009. Contamination of the asteroid belt by primordial trans-Neptunian objects. Nature. 460**,** p. 364.

Li, B., et al., 2017. Rock size-frequency distributions analysis at lunar landing sites based on remote sensing and in-situ imagery. Planetary and Space Science. 146**,** pp. 30-39.

Li, H., et al., 2016. Rock Dynamics: From Research to Engineering: Proceedings of the 2nd International Conference on Rock Dynamics and Applications. CRC Press, p. 42.

Lorenz, R. D., 2000. Microtektites on Mars: Volume and texture of distal impact ejecta deposits. Icarus. 144**,** pp. 353-366.

Lowrie, W., 2007. Fundamentals of Geophysics. Cambridge University Press, pp. 60-61.

Marchi, S., et al., 2009. A New Chronology for the Moon and Mercury. The Astronomical Journal. 137**,** p. 4936.

Marchi, S., et al., 2016. Cratering on Ceres: The puzzle of the missing large craters. Lunar Planet. Sci. XXXXVII, 1281 (abstract).

Martens, H. R., et al., 2015. Spatial distribution of ice blocks on Enceladus and implications for their origin and emplacement. Icarus. 245**,** pp. 162-176.

Mazrouei, S., et al., 2014. Block distributions on Itokawa. Icarus. 229**,** pp. 181-189.

McCord, T. B., Sotin, C., 2005. Ceres: Evolution and current state. J. Geophys. Res. 110**,** p. E05009.

McEwen, A. S., Bierhaus, E. B., 2006. The importance of secondary cratering to age constraints on planetary surfaces. Annual Review of Earth and Planetary Sciences. 34**,** pp. 535-567.

Melosh, H., Ivanov, B., 1999. Impact crater collapse. Annual Review of Earth and Planetary Sciences. 27**,** pp. 385-415.

Melosh, H. J., 1984. Impact ejection, spallation, and the origin of meteorites. Icarus. 59**,** pp. 234-260.

Melosh, H. J., 1989. Impact cratering: a geologic process. Oxford University Press, pp. 46-111.
Melosh, H. J., 2011. Planetary Surface Processes. Cambridge University Press, pp. 30, 335.
Mest, S., et al., 2017. The global geologic map of Ceres based on Dawn HAMO observations. 48th Lunar Planet. Sci. Conf. Lunar and Planetary Institute, The Woodlands, p. 2512 (abstract).
Michael, G. G., Neukum, G., 2010. Planetary surface dating from crater size-frequency distribution measurements: Partial resurfacing events and statistical age uncertainty. Earth Planet. Sci. Lett. 294**,** pp. 223–229.
Michael, G. G., et al., 2012. Planetary surface dating from crater size–frequency distribution measurements: Spatial randomness and clustering. Icarus. 218**,** pp. 169-177.
Michael, G. G., 2013. Planetary surface dating from crater size-frequency distribution measurements: Multiple resurfacing episodes and differential isochron fitting. Icarus. 226**,** pp. 885-890.
Michel, P., Morbidelli, A., 2007. Review of the population of impactors and the impact cratering rate in the inner solar system. Meteoritics & Planetary Science. 42**,** pp. 1861-1869.
Michikami, T., et al., 2008. Size-frequency statistics of boulders on global surface of asteroid 25143 Itokawa. Earth, planets and space. 60**,** pp. 13-20.
Minton, D. A., Malhotra, R., 2009. A record of planet migration in the main asteroid belt. Nature. 457**,** p. 1109.
Morgan, J. V., et al., 2016. The formation of peak rings in large impact craters. Science. 354**,** p. 878.
Morris, D. N., 1964. Charts for determining the characteristics of ballistic trajectories in a vacuum. RAND Corporation, Santa Monica, CA.
Nakamura, A., et al., 2008. Impact process of boulders on the surface of asteroid 25143 Itokawa—fragments from collisional disruption. Earth, planets and space. 60**,** pp. 7-12.
Naß, A., et al., 2011. Implementation of cartographic symbols for planetary mapping in geographic information systems. Planet. Space Sci. 59**,** pp. 1255–1264.
Naß, A., et al., 2015. GIS-based template for geological mapping - Ceres use case. ISPRS Workshop of Working Group IV/8: Planetary Mapping and Spatial Databases, p. (abstract).
Nathues, A., et al., 2015. Sublimation in bright spots on (1) Ceres. Nature. 528**,** p. 237.
Nathues, A., et al., 2017. Occator crater in color at highest spatial resolution. Icarus. in press.
Nayak, M., Asphaug, E., 2016. Sesquinary catenae on the Martian satellite Phobos from reaccretion of escaping ejecta. Nature communications. 7**,** p. 12591.
Nayak, M., et al., 2016. Effects of mass transfer between Martian satellites on surface geology. Icarus. 267**,** pp. 220-231.
Neukum, G., Ivanov, B., 1994. Crater size distributions and impact probabilities on Earth from lunar, terrestrial-planet, and asteroid cratering data. Hazards due to Comets and Asteroids. University of Arizona Press, pp. 359-416.
Newman, M. E., 2005. Power laws, Pareto distributions and Zipf's law. Contemporary Physics. 46**,** pp. 323-351.
Nier, A. O., McElroy, M. B., 1977. Composition and structure of Mars' Upper atmosphere: Results from the neutral mass spectrometers on Viking 1 and 2. Journal of Geophysical Research. 82**,** pp. 4341-4349.
O'Brien, D. P., Sykes, M. V., 2011. The origin and evolution of the asteroid belt—Implications for Vesta and Ceres. Space Science Reviews. 163**,** pp. 41-61.
O'Brien, D. P., et al., 2014. Constraining the cratering chronology of Vesta. Planetary and Space Science. 103**,** pp. 131-142.
Oliphant, T. E., 2007. Python for Scientific Computing. Computing in Science and Engg. 9**,** pp. 10-20.
Osinski, G. R., Pierazzo, E., 2012. Impact Cratering: Processes and Products. Wiley, p. 203.
Otto, K. A., et al., 2013. Mass-wasting features and processes in Vesta's south polar basin Rheasilvia. Journal of Geophysical Research: Planets. 118**,** pp. 2279-2294.
Pajola, M., et al., 2015. Size-frequency distribution of boulders ≥ 7 m on comet 67P/Churyumov-Gerasimenko. Astronomy & Astrophysics. 583**,** p. A37.
Palomba, E., et al., 2017. Compositional differences among Bright Spots on the Ceres surface. Icarus. in press.
Park, R. S., et al., 2016. A partially differentiated interior for (1) Ceres deduced from its gravity field and shape. Nature. 537**,** pp. 515–517.
Pasckert, J. H., et al., 2018. Geologic mapping of the Ac-2 Coniraya quadrangle of Ceres from NASA's Dawn mission: Implications for a heterogeneously composed crust. Icarus. 316**,** pp. 28-45.

Petrovic, J. J., 2003. Review Mechanical properties of ice and snow. Journal of Materials Science. 38**,** pp. 1-6.
Pierazzo, E., Melosh, H. J., 2000. Understanding Oblique Impacts from Experiments, Observations, and Modeling. Annual Review of Earth and Planetary Sciences. 28**,** pp. 141-167.
Pike, R. J., 1971. Genetic implications of the shapes of martian and lunar craters. Icarus. 15**,** pp. 384-395.
Pilcher, F., 1979. Circumstances of minor planet discovery. Asteroids. pp. 1130-1154.
Platz, T., et al., 2015. Putative volcanic landforms on Ceres. EPSC 2015, 915 (abstract).
Platz, T., et al., 2016a. Impact Cratering on Ceres: The simple-to-complex transition., Lunar and Planetary Science, Vol. (abstract), p. 2308 (abstract).
Platz, T., et al., 2016b. Surface water-ice deposits in the northern shadowed regions of Ceres. Nature Astronomy. 1**,** p. 0007.
Platz, T., et al., 2018. Geological mapping of the Ac-10 Rongo Quadrangle of Ceres. Icarus. 316**,** pp. 140-153.
Plescia, J. B., 2004. Morphometric properties of Martian volcanoes. J. Geophys. Res. 109**,** p. E03003.
Prettyman, T. H., et al., 2003. Gamma-ray and neutron spectrometer for the Dawn mission to 1 Ceres and 4 Vesta. IEEE Transactions on Nuclear Science. 50**,** pp. 1190-1197.
Prettyman, T. H., et al., 2011. Dawn's gamma ray and neutron detector. Space Sci. Rev. 163**,** pp. 371-459.
Prettyman, T. H., et al., 2017. Extensive water ice within Ceres' aqueously altered regolith: Evidence from nuclear spectroscopy. Science. 355**,** pp. 55-59.
Preusker, F., et al., 2016. Dawn at Ceres - Shape model and rotational state. Lunar Planet. Sci. XXXXVII, 1954 (abstract).
Quaide, W. L., Oberbeck, V. R., 1968. Thickness determinations of the lunar surface layer from lunar impact craters. Journal of Geophysical Research. 73**,** pp. 5247-5270.
Reddy, V., et al., 2012. Color and albedo heterogeneity of Vesta from Dawn. Science. 336**,** pp. 700-704.
Reiche, P., 1937. The Toreva-Block: A Distinctive Landslide Type. The Journal of Geology. 45**,** pp. 538-548.
Richardson, J. E., et al., 2005. Impact Cratering Theory and Modeling for the Deep Impact Mission: From Mission Planning to Data Analysis. Space Science Reviews. 117**,** pp. 241-267.
Richardson, J. E., et al., 2007. A ballistics analysis of the Deep Impact ejecta plume: Determining Comet Tempel 1's gravity, mass, and density. Icarus. 191**,** pp. 176-209.
Rivkin, A. S., et al., 2011. The surface composition of Ceres. Space Sci. Rev. 163**,** pp. 95–116.
Roatsch, T., et al., 2016a. High-resolution Ceres High Altitude Mapping Orbit atlas derived from Dawn Framing Camera images. Planetary and Space Science. 129**,** pp. 103-107.
Roatsch, T., et al., 2016b. Ceres Survey Atlas derived from Dawn Framing Camera images. Planetary and Space Science. 121**,** pp. 115-120.
Roatsch, T., et al., 2017. High-resolution Ceres Low Altitude Mapping Orbit Atlas derived from Dawn Framing Camera images. Planetary and Space Science. 140**,** pp. 74-79.
Ruesch, O., et al., 2016. Cryovolcanism on Ceres. Science. 353**,** p. aaf4286.
Russell, C. T., Raymond, C. A., 2011. The Dawn Mission to Vesta and Ceres. Space Sci. Rev. 163**,** pp. 3–23.
Russell, C. T., et al., 2012. Dawn at Vesta: Testing the Protoplanetary Paradigm. Science. 336**,** p. 684.
Russell, C. T., et al., 2013. Dawn completes its mission at 4 Vesta. Meteoritics & Planetary Science. 48**,** pp. 2076-2089.
Russell, C. T., et al., 2016. Dawn arrives at Ceres: Exploration of a small, volatile-rich world. Science. 353**,** pp. 1008-1010.
Schedl, A., 2015. Searching for Distal Ejecta on the Craton: The Sedimentary Effects of Meteorite Impact. The Journal of Geology. 123**,** pp. 201-232.
Schenk, P. M., et al., 2016. Impact cratering on the small planets Ceres and Vesta: S-C transitions, central pits, and the origin of bright spots. Lunar Planet. Sci. XXXXVII, 2697 (abstract).
Schmedemann, N., et al., 2014. The cratering record, chronology and surface ages of (4) Vesta in comparison to smaller asteroids and the ages of HED meteorites. Planetary and Space Science. 103**,** pp. 104-130.
Schmedemann, N., et al., 2015. A preliminary chronology for Ceres. Lunar Planet. Sci. XXXXVI, The Woodlands, TX, p. (abstract).
Schmedemann, N., et al., 2016. Timing of optical maturation of recently exposed material on Ceres. Geophysical Research Letters. 43**,** pp. 11987-11993.

Schmedemann, N., et al., 2017. The distribution of impact ejecta on Ceres. Lunar Plan. Sci., The Woodlands, TX, p. 1233 (abstract).
Schmidt, B. E., et al., 2017. Geomorphological evidence for ground ice on dwarf planet Ceres. Nature Geosci. 10**,** pp. 338-343.
Schmidt, R. M., Housen, K. R., 1987. Some recent advances in the scaling of impact and explosion cratering. International Journal of Impact Engineering. 5**,** pp. 543-560.
Schorghofer, N., et al., 2016. The permanently shadowed regions of dwarf planet Ceres. Geophysical Research Letters. 43**,** pp. 6783-6789.
Schröder, S. E., et al., 2016. Boulders on Ceres. EGU (abstract).
Schultz, P. H., 1992. Atmospheric effects on ejecta emplacement. 97**,** pp. 11623-11662.
Schultz, P. H., et al., 2005. Expectations for crater size and photometric evolution from the Deep Impact collision. Space Science Reviews. 117**,** pp. 207-239.
Schultz, P. H., Wrobel, K. E., 2012. The oblique impact Hale and its consequences on Mars. Journal of Geophysical Research: Planets. 117**,** p. E04001.
Scully, J. E. C., et al., 2017. Evidence for the Interior Evolution of Ceres from Geologic Analysis of Fractures. Geophysical Research Letters. 44**,** pp. 9564-9572.
Scully, J. E. C., et al., 2018. Ceres' Occator crater and its faculae explored through geologic mapping. Icarus. in press.
Seeds, M. A., Backman, D., 2015. The Solar System. Cengage Learning, p. 349.
Seidelmann, P. K., et al., 2007. Report of the IAU/IAG Working Group on cartographic coordinates and rotational elements: 2006. Celestial Mechanics and Dynamical Astronomy. 98**,** pp. 155-180.
Shoemaker, E. M., 1962. Interpretation of lunar craters. Physics and Astronomy of the Moon. pp. 283-359.
Shoemaker, E. M., 1965. 2. Preliminary Analysis of the Fine Structure of the Lunar Surface in Mare Cognitum. International Astronomical Union Colloquium. 5**,** pp. 23-77.
Shoemaker, E. M., 1998. Impact cratering through geologic time. Journal of the Royal Astronomical Society of Canada. 92**,** p. 297.
Sierks, H., et al., 2011. The Dawn Framing Camera. Space Sci. Rev. 163**,** pp. 263–327.
Sizemore, H. G., et al., 2017. Pitted terrains on (1) Ceres and implications for shallow subsurface volatile distribution. Geophysical Research Letters. 44**,** pp. 6570-6578.
Steeb, W. H., 2004. Problems & Solutions in Scientific Computing: With C++ and Java Simulations. World Scientific, p. 245.
Stephan, K., et al., 2017a. An investigation of the bluish material on Ceres. Geophysical Research Letters. 44**,** pp. 1660-1668.
Stephan, K., et al., 2017b. Ceres' Impact Craters – Relationships between Surface Composition and Geology. Icarus. in press.
Tanaka, K., et al., 2009. Planetary Geologic Mapping Handbook-2009.
Tanaka, K. L., Hartmann, W. K., 2012. Chapter 15 - The Planetary Time Scale. The Geologic Time Scale. Elsevier, Boston, pp. 275-298.
Thomas, N., et al., 2012. The geomorphology of (21) Lutetia: Results from the OSIRIS imaging system onboard ESA's Rosetta spacecraft. Planet. Space Sci. 66**,** pp. 96-124.
Thomas, P., et al., 2000. Phobos: Regolith and ejecta blocks investigated with Mars Orbiter Camera images. Journal of Geophysical Research: Planets. 105**,** pp. 15091-15106.
Thomas, P., et al., 2001. Shoemaker crater as the source of most ejecta blocks on the asteroid 433 Eros. Nature. 413**,** p. 394.
Thomas, P. C., et al., 2005. Differentiation of the asteroid Ceres as revealed by its shape. Nature. 437**,** pp. 224–226.
USGS, 2006. FGDC Digital Cartographic Standard for Geologic Map Symbolization (PostScript Implementation): U.S. Geological Survey Techniques and Methods 11-A2.
v. Gasselt, S., Nass, A., 2011. Planetary mapping—The datamodel's perspective and GIS framework. Planetary and Space Science. 59**,** pp. 1231-1242.
Vickery, A., 1986. Size-velocity distribution of large ejecta fragments. Icarus. 67**,** pp. 224-236.
von der Gathen, I., et al., 2016. Deformational features on Ceres' surface compared to other planetary bodies. Lunar Planet. Sci. XXXXVII, 1961 (abstract).
Vothihong, P., et al., 2017. Python: Data Analytics and Visualization. Packt Publishing, Birmingham, p. 298 ff.

Walsh, K. J., et al., 2012. Populating the asteroid belt from two parent source regions due to the migration of giant planets—"The Grand Tack". Meteoritics & Planetary Science. 47**,** pp. 1941-1947.

Weibull, W., 1951. Wide applicability. Journal of applied mechanics. 103**,** pp. 293-297.

Weiss, D., Head, J., 2014. Ejecta mobility of layered ejecta craters on Mars: Assessing the influence of snow and ice deposits. Icarus. 233**,** pp. 131–146.

Werner, S. C., 2009. The global Martian volcanic evolutionary history. Icarus. 201**,** pp. 44-68.

Werner, S. C., et al., 2009. Theoretical analysis of secondary cratering on Mars and an image-based study on the Cerberus Plains. Icarus. 200**,** pp. 406-417.

Werner, S. C., Ivanov, B. A., 2015. 10.10 - Exogenic Dynamics, Cratering, and Surface Ages A2 - Schubert, Gerald. Treatise on Geophysics (Second Edition). Elsevier, Oxford, pp. 327-365.

Wieczorek, M. A., Zuber, M. T., 2001. A Serenitatis origin for the Imbrian grooves and South Pole-Aitken thorium anomaly. Journal of Geophysical Research: Planets. 106**,** pp. 27853-27864.

Wilhelms, D., et al., 1978. Size-frequency distributions of primary and secondary lunar impact craters. Lunar Planet. Sci. IX, pp. 3735-3762 (abstract).

Wilhelms, D., 1990. Geologic mapping. In: R. Greeley, R. M. Batson, (Eds.), Planetary mapping. Cambridge University Press, pp. 208-260.

Wille, P. D. F., et al., 2013. Höhere Mathematik für Ingenieure: Band II Lineare Algebra. Vieweg+Teubner Verlag, p. 349.

Williams, D. A., et al., 2014. Introduction: The geologic mapping of Vesta. Icarus. 244**,** pp. 1–12.

Williams, D. A., et al., 2018a. Introduction: The geologic mapping of Ceres. Icarus. 316**,** pp. 1-13.

Williams, D. A., et al., 2018b. The geology of the Kerwan quadrangle of dwarf planet Ceres: Investigating Ceres' oldest, largest impact basin. Icarus. 316**,** pp. 99-113.

Wilson, L., Head, J. W., 2015. Groove formation on Phobos: Testing the Stickney ejecta emplacement model for a subset of the groove population. Planetary and Space Science. 105**,** pp. 26-42.

Wrobel, K. E., 2004. Effect of planetary rotation on distal tektite deposition on Mars. Journal of Geophysical Research. 109**,** p. E05005.

Wyrick, D., 2004. Distribution, morphology, and origins of Martian pit crater chains. J. Geophys. Res. 109**,** p. E06005.

Xiao, Z., Strom, R. G., 2012. Problems determining relative and absolute ages using the small crater population. Icarus. 220**,** pp. 254-267.

Yingst, R. A., et al., 2014. Geologic mapping of Vesta. Planet. Space Sci. 103**,** pp. 2–23.

Zwillinger, D., 2011. CRC Standard Mathematical Tables and Formulae, 32nd Edition. CRC Press, p. 356.